

Atom Interferometry with ultracold Rubidium atoms

विद्या वाचस्पति की उपाधि की अपेक्षाओं की आंशिक पूर्ति में प्रस्तुत शोध प्रबंध

A thesis submitted in partial fulfillment of the requirements of the
degree of Doctor of Philosophy

द्वारा / By

प्रणब दत्ता / Pranab Dutta)

पंजीकरण सं. / Registration No.: 20173563

शोध प्रबंध पर्यवेक्षक / Thesis Supervisor: Dr. Umakant D.
Rapol



भारतीय विज्ञान शिक्षा एवं अनुसंधान संस्थान पुणे
INDIAN INSTITUTE OF SCIENCE EDUCATION AND RESEARCH PUNE

2024

Certificate

Certified that the work incorporated in the thesis entitled “**Atom Interferometry with ultracold Rubidium atoms**” submitted by **Pranab Dutta** was carried out by the candidate, under my supervision. The work presented here or any part of it has not been included in any other thesis submitted previously for the award of any degree or diploma from any other university or institution.

Date: 22/08/2024



(Supervisor)

Declaration by Student

Name of Student: Pranab Dutta

Reg. No.: 20173563

Thesis Supervisor(s): Prof. Umakant D. Rapol

Department: Physics

Date of joining program: 01/08/2017

Date of Pre-Synopsis Seminar : 14/02/2024

Title of Thesis : **Atom Interferometry with ultracold Rubidium atoms**

I declare that this written submission represents my idea in my own words and where others' ideas have been included; I have adequately cited and referenced the original sources. I declare that I have acknowledged collaborative work and discussions wherever such work has been included. I also declare that I have adhered to all principles of academic honesty and integrity and have not misrepresented or fabricated or falsified any idea/data/fact/source in my submission. I understand that violation of the above will be cause for disciplinary action by the Institute and can also evoke penal action from the sources which have thus not been properly cited or from whom proper permission has not been taken when needed.

The work reported in this thesis is the original work done by me under the guidance of Prof. Umakant D. Rapol.

Date: 22/08/2024

A handwritten signature in black ink, reading "Pranab Dutta", with a horizontal line underneath the name.

Signature of the student

Abstract

Atom interferometry, a technique that leverages the wave nature of atoms to create interference patterns, has emerged as a powerful tool for high-precision measurements. This method exploits the principles of quantum mechanics, particularly the wave-particle duality, to achieve remarkable sensitivity and accuracy. Atom interferometers utilize coherent matter waves, typically of ultracold atoms, which are manipulated using laser pulses to form superposition states that interfere. The resulting interference patterns provide insights into various physical phenomena, making atom interferometers highly effective in precision metrology, fundamental physics, and practical applications.

The development of quantum sensors based on atom interferometry has opened new frontiers in measurement science. Quantum sensors exploit quantum coherence and entanglement to surpass the limitations of classical sensors, offering unprecedented precision. In the realm of inertial sensing, atom interferometers can measure accelerations and rotations with extraordinary accuracy, leading to advances in navigation systems, geophysics, and seismology. For instance, gravimeters based on atom interferometry can detect minute changes in gravitational acceleration, useful for mineral exploration, monitoring volcanic activity, and detecting underground structures.

In addition to inertial sensing, atom interferometry is pivotal in testing fundamental physics. It allows precise measurements of constants such as the fine-structure constant and the gravitational constant. Moreover, atom interferometers are instrumental in experiments probing the equivalence principle, a cornerstone of general relativity, and in searches for dark matter and gravitational waves. The sensitivity of these interferometers to tiny perturbations makes them ideal for detecting phenomena predicted by theories beyond the Standard Model of particle physics. The engineering of quantum sensors using atom interferometry involves several critical technologies. These include techniques for cooling and trapping atoms, precise control of laser fields, and advanced methods for isolating the system from environmental noise. Innovations in these areas have led to the development of portable and even chip-scale atom interferometers, broadening their applicability in various fields.

Despite significant progress, challenges remain in the practical deployment of atom interferometer-based quantum sensors. These include enhancing the coherence time of

atomic superposition states, improving robustness against environmental disturbances, and miniaturizing the systems for real-world applications. Ongoing research focuses on overcoming these challenges through novel quantum control techniques, improved atom optics, and integration with microfabricated technologies.

This work explores the development of atomic sensor technology through several key areas. It begins with a detailed examination of atom interferometers, focusing on the interaction between light and atoms in two-level and three-level systems, and the principles of Bragg and Raman diffraction.

The research then describes the design and assembly of an experimental setup capable of producing an ensemble of ultracold atoms at a temperature of 100 nK. This setup includes a Bragg lattice used to develop an atom interferometer for ultracold ^{87}Rb atoms.

Subsequent analysis covers Bragg diffraction and atom interferometry, providing insights into the diffraction process within the experimental setup and its influence on atom transitions between momentum states. This section also includes a demonstration of a Mach-Zehnder interferometer utilizing Bragg diffraction.

The implementation of the atom interferometer is investigated as an atomic gravimeter, with a new approach proposed to reduce phase noise and improve measurement accuracy and precision.

Lastly, the work examines double Bragg diffraction and its potential applications, proposing a new concept for an atom-based Sagnac interferometer to advance the field of atomic sensors.

To my **Family**

Publications from the thesis work

- A Decade of Advancement of Quantum Sensing and Metrology in India Using Cold Atoms and Ions. *J Indian Inst Sci*; **Pranab Dutta**, S. Sagar Maurya, Kushal Patel, Korak Biswas, Umakant D. Rapol, et al. *J Indian Inst Sci*, **103**, 609–632 (2023)
- Comparative Analysis of Phase Noise for different configurations of Bragg lattice for an Atomic Gravimeter with Bose-Einstein Condensate; **Pranab Dutta**, S. Sagar Maurya, Korak Biswas, Kushal Patel, Umakant D. Rapol, *AIP Advances* , **14**, 015352 (2024)

List of other publications

- Effects of finite momentum width on the reversal dynamics in a BEC based atom optics δ -kicked rotor. Jay Mangaonkar, Chetan Vishwakarma, S. Sagar Maurya, Sumit Sarkar, Jamie L MacLennan, **Pranab Dutta** and Umakant D Rapol, 2020, *J. Phys. B: At. Mol. Opt. Phys.*, **53** 235502 (2020)
- Interplay between quantum diffusion and localization in the atom-optics kicked rotor; S. Sagar Maurya, J. Bharathi Kannan, Kushal Patel, **Pranab Dutta**, Korak Biswas, Jay Mangaonkar, M. S. Santhanam, and Umakant D. Rapol; *Phys. Rev. E* **106**, 034207 (2022)
- Machine-learning-based automated loading of strontium isotopes into magneto-optical trap; Korak Biswas, Kushal Patel, S. Sagar Maurya, **Pranab Dutta**, Umakant D. Rapol; *AIP Advances*, **13** 075313 (2023)
- Spectroscopy of the $5s5p^3P_0 \rightarrow 5s5d^3D_1$ transition of strontium using laser cooled atoms; Kushal Patel, Palki Gakkhar, Korak Biswas, S. Sagar Maurya, **Pranab Dutta**, Vishal Lal, Brajesh Mani, Umakant D Rapol *J. Phys. B: At. Mol. Opt. Phys.*, **57**, 105501 (2024)

Manuscripts under review

- Evaporative Cooling by Switching the Optical Dipole Traps On and Off; S Sagar Maurya*, **Pranab Dutta***, Korak Biswas, Kushal Patel, and Umakant D. Rapol
* Both the authors have contributed equally to the work.
- Asymmetric Dynamical Localization And Precision Measurement of BEC Micromotion; S. Sagar Maurya, J. Bharathi Kannan, Kushal Patel, **Pranab Dutta**, Korak Biswas, M. S. Santhanam, and Umakant D. Rapol
- Electromagnetically Induced Transparency (EIT) aided cooling of strontium atomss.; Korak Biswas, Kushal Patel, S. Sagar Maurya, **Pranab Dutta**, Umakant D. Rapol and Yeshpal Singh, *arXiv: 2311.08318* (2023)

Patents

- OVEN FOR GENERATION AND COLLIMATION OF AN ATOMIC BEAM, Umakant D Rapol, Kushal Patel, Korak Biswas, S. Sagar Maurya, **Pranab Dutta**, Indian Patent Application Number 202421000590. Filed on January 03, 2024.
- CHEMICAL OXYGEN GENERATOR Umakant D Rapol, Kushal Patel, Korak Biswas, S. Sagar Maurya, **Pranab Dutta**, Indian Patent Application Number 202121020842, Filed on May 07, 2021. The patent has been granted
- Hybrid oxygen system using passive and active systems Umakant D Rapol, Kushal Patel, Korak Biswas, S. Sagar Maurya, **Pranab Dutta**, Indian Patent Application Number 202111029508, Filed on June 30, 2021

Acknowledgments

My interest in physics research was ignited by my uncle, Swapan Das. I completed my Master's degree in Physics at Gauhati University. Feeling uncertain about how to pursue admission into prestigious universities, I relocated to New Delhi to prepare for competitive government exams. During this period, I stumbled upon macroeconomics, which significantly impacted my career aspirations. However, my passion for physics persisted, leading me to successfully clear the CSIR-JRF exam. This achievement secured me a position as a junior researcher at IISER Pune, where I now work in the Experimental Physics lab, specifically focusing on Atomic Physics and Quantum Optics (APQO).

The journey of the past seven years has been incredibly interesting, filled with valuable learning experiences. During this time, I transitioned from being a core researcher to becoming an entrepreneur. My initial weeks at IISER Pune were a unique experience, as I had never been in an environment where everyone was so focused on their careers and clear about their goals. Early on, I was instructed to meet the faculty member under whom I wanted to conduct my research. My fascination with quantum physics led me to the Experimental Physics lab, where I expressed my desire to study under Prof. Umakant Rapol. He accepted me as his student, and even after more than seven years, I believe it was the best decision I could have made. In the lab, I had the privilege of working with my seniors: Dr. Sumit Sarkar, Dr. Gunjan Verma, Dr. Chetan Vishwakarma, and Dr. Jay Mangaonkar.

I joined the APQO lab to develop an atom interferometer using ultracold atoms and had the privilege of learning about the equipment and techniques from senior members. That same year, I met my lab mates S. Sagar Maurya, Kushal Patel, and Korak Biswas. Together, we worked on two experimental setups involving Strontium and Rubidium. We frequently discussed the challenges we faced in the lab, collaborating to understand and address the problems we were targeting. Beyond our research, we explored creative ideas and enjoyed developing an oxygen generator during the COVID-19 pandemic, which strengthened our bond. It was during this time that we also conceived the idea of starting a startup together.

I would like to express my deep gratitude to my supervisor Prof. Umakant Rapol,

who has been instrumental in shaping who I am today. The initial days were challenging as I adapted to working with sophisticated instruments, but he consistently encouraged and motivated me. Additionally, I am especially thankful for his unwavering support in helping us establish our startup.

I would like to express my gratitude to my Research Advisory Committee (RAC) members, Prof. Ajay Wasan and Dr. Sreejith G.J, for their invaluable feedback and insightful suggestions. Their annual evaluations were instrumental in guiding my research in the right direction.

The construction of the experimental setup and the execution of experiments would not have been possible without the support of Technical Officer Mr. Nilesh Dumbre and the technical staff, Karthikeyan S. and Sudhir Lone. I would also like to thank Prabhakar Anagare and Dhanashree Sheth for their efficient handling of all the administrative tasks.

I have always drawn my inspiration from my parents, Mr. Ranjit Kumar Dutta and Mrs. Anjana Das Dutta, and I am deeply grateful to them for being a constant source of motivation throughout my life. My brother, Sion Dutta, despite his mischievous nature, is very dear to me. He has been like a mother to me, providing delicious food and bringing a smile to my face, even when I was thousands of kilometres away from home. Lastly, I want to thank my dear wife Mrs. Madhushmita Paul , who accompanied me in my final stages of my PhD and was a constant source of support.

I would also like to thank the Council of Scientific and Industrial Research (CSIR) for awarding me the scholarship during my Ph.D., and IHUB-QTF for funding me for six months during the final stages of my research.

Last but not least, I want to thank my friends Umashankar Rajput, Vrinda Narayanan, Gokul M. A., Manisha Rajput, and Suraj Lakhchaura, as well as my junior labmates Vishal Lal, Rhuthwik Skanda, Anurag Bhadane, and RAYEES A S for their companionship and the quality time we spent together. I am grateful to IISER Pune for providing a pleasant working environment.

Date: July 8, 2024

(Pranab dutta)

Contents

Abstract	vii
Publications from the thesis work	xi
List of other publications	xiii
Manuscripts under review	xv
Manuscripts under preparation	xvii
Acknowledgments	xix
List of figures	xxv
List of tables	xxxiii
1 Introduction	1
1.1 Exploring Quantum Sensors for Precise Measurements	1
1.1.1 Inertial sensing using cold atom sensors	2
1.2 Atom Interferometer (AI)	5
1.2.1 Stepwise Explanation of an Atom Interferometer	5
1.3 Different types of Atom Interferometer	7
1.3.1 Mach-Zehnder Atom Interferometer	7
1.3.2 Ramsey-Bordé Atom Interferometer	8

1.3.3	Multi-Path Atom Interferometer	8
1.4	Different cold atom sensor applications	8
1.4.1	Determination of the Fine Structure Constant	8
1.4.2	Testing the equivalence principle:	10
1.4.3	Gravitational wave detection:	11
1.4.4	Measuring gravity with atoms	12
1.4.5	Quantum gyroscope with atoms	13
1.5	Emerging techniques to enhance the sensitivity in Atom Interferometer .	15
1.5.1	Quantum Entanglement in Atom Interferometry	15
1.5.2	Large Momentum Transfer	17
1.6	Real field application of quantum sensors	18
1.6.1	Geoexploration and Civil engineering	18
1.6.2	Inertial Navigation System	19
1.7	Objective of the thesis	24
1.8	Outline of the thesis	26
2	Theoretical Background	27
2.1	A brief overview of cold atoms and Bose-Einstein Condensate.	27
2.2	Two-photon Transition	30
2.2.1	Light atom diffraction theory	32
2.2.2	Summary	44
3	Experimental apparatus and methods	45
3.1	The vacuum assembly	45
3.1.1	Modes of Gas Flow	46
3.1.2	Vacuum system	47
3.2	The oven	48
3.3	Laser System	51
3.3.1	Laser diode's emission spectrum	51
3.3.2	Cooling and re-pumping laser	55
3.3.3	Laser for Bragg lattice	59
3.3.4	Optical dipole trap	61

3.4	Summary	64
4	Bragg Diffraction and Atom Interferometry	65
4.1	Bragg diffraction of Atoms in momentum space	65
4.1.1	Higher order Bragg diffractions	67
4.2	Bragg spectroscopy of Atoms in momentum space	70
4.2.1	Momentum width of the BEC	71
4.3	Atom Interferometry	74
4.3.1	Bragg pulse interaction in an atom interferometer	75
4.3.2	Free evolution between the pulses	78
4.4	Mach-Zehnder Interferometer	79
4.5	Summary	82
5	Atomic Gravimeter	83
5.1	Introduction	84
5.2	Quantum Gravimeter	85
5.2.1	Measurement Principle	85
5.2.2	Noise Model of an Interferometer due to its optical path	88
5.2.3	Sensitivity Function	88
5.3	Experimental Details	91
5.4	Results and discussion	93
5.4.1	Phase Noise for different configuration	93
5.4.2	Stability of the gravity measurement	95
5.5	Conclusion	97
6	Atom based rotation sensor	99
6.1	Sagnac Theory	99
6.1.1	Employing a path integral approach to solve the Sagnac inter- ferometer configuration	100
6.2	Rotation sensor using atom interferometry	101
6.2.1	Three pulse (MZI) rotation sensor :	102
6.2.2	Four Pulse Ramsey-Bordé Atom Interferometry rotation sensor	105

6.3	Differential atom interferometer	105
7	Conclusion and Outlook	109
7.1	Summary	109
7.2	Future outlook	110

List of Figures

- 1.1 **Classical and quantum sensor comparison:** The working principle of a cold-atom accelerometer or interferometer involves using a standing wave along with an ensemble of cold atoms. The standing wave acts as an optical ruler, guiding the atoms as they fall freely through the system. During their descent, the atoms interact with a first beam splitter, a mirror pulse, and a final beam splitter. This interaction causes a phase shift, which can be detected at the output ports of the atom interferometer. 2

- 1.2 **Atom Interferometer for Various Applications:** **Fig (a):** Atomic gravimeter adapted from [1]. **Fig (b):** Rotation sensor adapted from [2]. **Fig (c):** Atomic clock adapted from NIST-F1 Cesium Fountain Clock **Credit:** NIST. 4

- 1.3 **Simultaneous Conjugate Ramsey-Borde Interferometers.** Solid lines show the trajectories of the atoms, while dashed lines indicate the laser pulses with their respective frequencies. The optical lattices are formed by two laser pulses contains two different frequencies, ω_1 , ω_2 and ω_1 , $\omega_2 \pm \omega_m$. BO stands for Bloch oscillations which helps us in creating an accelerating optical lattice acquiring momentum from two photon recoils per BO. $|n\rangle$ represents a momentum eigenstate with momentum $2n\hbar k$ 9

1.4	Schematic diagram of Bose Einstein Condensate (BEC) based Atom Interferometer and its space time trajectories. The blue dots represents BEC with ballistic expansion after release from the dipole trap. The experiment runs in three steps.(i) The conversion of mean field energy into kinetic energy of BEC during time of flight T_{tof} (ii) the MZI with different interferometric time ranging from ms (iii) the final pulse for detection after allowing the wave packets to separate with τ_{sep} ms. .	13
1.5	Atom based Sagnac interferometer. Schematic of a matter-wave Sagnac interferometer based on two-photon Raman transitions. An optical illustration of atom interferometer is shown in the left diagram. An atom in state $ 1\rangle$, with center-of-mass velocity $v = \frac{p}{M}$, is subjected to a sequence of counter-propagating laser pulses that are rotating relative to the atomic trajectory at a constant rate Ω	14
1.6	Spin squeezing in an atom interferometer: a) Schematic diagram of an atom interferometer, b) and c) Coherent Spin State evolution of non-entangled states and entangled states, d) and e) The output signal for phase measurement above and below SQL. (Reprinted from [3], with the permission of AIP Publishing)	16
1.7	The usual magnitudes of gravity gradient anomalies produced by different gravitational sources. ($1E = 10^{-9}s^{-2}$). (This figure is adapted from [4])	19
1.8	Gimbaled Based INS. In this system, the INS includes a 3-axis gyroscope that measures angular velocities Ω_x , Ω_y , and Ω_z , which are used to adjust the orientation via a feedback loop controlling the gimbals. At the same time, accelerometers measure accelerations along each axis, a_x , a_y , and a_z^{tot} , while accounting for mobile rotations. The gravitational acceleration g is subtracted from a_z^{tot} to obtain the mobile's true acceleration a_z . By performing a double integration of this acceleration, the position components x , y , and z can be derived.	20

1.9	Strapdown based INS. The gyroscopes provide angular velocities which, when integrated over time from the initial attitude, define the current attitude in terms of Euler angles α , β , and γ . In a strap-down INS, accelerations along three axes are measured, with gravitational acceleration projected onto each component a_x^{tot} , a_y^{tot} , and a_z^{tot} , while Coriolis accelerations introduce perturbations. Initially, these accelerations are projected onto the navigation frame determined by the current Euler angles of the mobile. They are then corrected for Coriolis acceleration, calculated using the gyroscopes, and gravitational acceleration $g(t)$. By double integrating these corrected accelerations, the position components x , y , and z are derived.	21
2.1	Temperature scale of cooling of atoms.	28
2.2	The two-photon transition configurations can be classified as follows: (a) Two-photon absorption (Ξ), where an initial photon, not in resonance with any atomic transition, is absorbed, leading to a virtual state, followed by a subsequent absorption event to a permissible real energy state. In this scenario, the combined energy of the photons, $\hbar(\omega_1 + \omega_2)$, must match the energy difference between the real states, denoted as $ g\rangle$. (b) Single-photon absorption coupled with a single spontaneous or stimulated emission event (Λ). Here, the disparity in photon energy, $\hbar (\omega_1 - \omega_2) $, must correspond to the energy separation between real states, $ e\rangle - g\rangle$. The deviations from resonance for single and two-photon processes are indicated by Δ and δ , respectively.	31
2.3	Schematic of a discrete two-level system under the presence of a non-resonant light field. This scheme involves the absorption of a single photon followed by either a spontaneous or a stimulated emission event. For this to occur, the energy difference of the absorbed photon, $\hbar \omega_{eg} - \omega_L $, must match the energy difference between the two real states, $ e\rangle$ and $ g\rangle$. The detuning of the single photon is represented by δ	34
2.4	Population probability $P_e(\tau)$ of excited state $ e\rangle$ from figure 2.3 for different detuning values.	37

2.5	^{87}Rb D2 Structure for Raman and Bragg Transitions (a) Co-propagating Raman beams induce transitions between the states $ F = 1, m_F = 0\rangle$ and $ F = 2, m_F = 0\rangle$. (b) Counter-propagating Bragg beams drive transitions between momentum states, where the energy separation corresponds to the two-photon recoil energy.	41
3.1	Images of the Vacuum System: (a) The figure shows the experimental setup of the oven system and its connected ion pump. (b) This image displays the experimental setup of the science chamber. (c) This image presents the complete experimental setup.	49
3.2	CAD Images of the Rb Oven System: The figures illustrate the design of the atomic reservoir, including the microdrill array and the flexible bellow. The second figure presents a cross-sectional view of the entire design.	50
3.3	Machine drawing for the implemented oven system.	50
3.4	The energy level diagram for cooling and trapping of atoms: The ^{87}Rb D2 transition structure including the Zeeman level splitting. The atoms are cooled in a hybrid trap of magnetic and optical trap. At the completion of cooling the atoms occupy the $F = 1, m_f = -1$ ground state.	52
3.5	Schematic layout of an external cavity diode laser	54
3.6	Optical Layout of the Laser System: A schematic diagram depicting the optical layout of the cooling and repumping laser system. Further details can be found in Sunil Kumar's thesis [6].	57
3.7	Optical Layout of the Laser System: The experimental setup of the optical layout	58
3.8	Laser Beam Preparation for Bragg Lattice: A schematic diagram illustrating two independent laser beams separated by $\Delta\omega \sim 15\text{ kHz}$ to generate the Bragg beams. The left dashed block represents the spectroscopy of ^{87}Rb , locked to the $5^2\text{S}_{1/2}, F = 2 \rightarrow 5^2\text{P}_{3/2}, F' = 2$ D2 transition at 780 nm. The right dashed block depicts the configuration of the Bragg laser system.	59

3.9	Laser Beam Preparation for Bragg Lattice: The experimental setup is depicted in the photograph.	60
3.10	Static Trap Depth for Dipole Beam: The calculated trap depth for a single-beam dipole trap with a wavelength of 1064 nm. The dipole beam is traveling along the x direction. This trap utilizes a Gaussian beam with a power of $P = 5$ W and a beam waist of $\omega_0 = 50 \mu\text{m}$	62
3.11	Laser Beam Preparation for Optical dipole trap: A schematic diagram illustrating the generation of dipole beams for evaporative cooling.	63
4.1	Bragg diffraction of atoms. Atoms engage with photons emitted by two laser beams, which have frequencies of ω and $\omega + \Delta\omega$ and intersect at an angle ϑ . These atoms can experience coherent diffraction, transitioning from an initial momentum state $ p_0\rangle = 0\hbar k\rangle$ to a final momentum state $ p_r\rangle = 2\hbar k \sin(\vartheta/2)\rangle$, provided that the energy difference between the laser beams meets the condition $\hbar\Delta\omega = \frac{p_r^2}{2m}$. This happens when atoms are exposed to two counter-propagating laser beams, they can undergo a process where they first absorb a photon from one beam, gaining its momentum, and then undergo stimulated emission into the opposing beam, emitting a photon and experiencing a recoil in the opposite direction.	66
4.2	Image of Bragg diffraction and Rabi oscillation for $\pi/2$ and π pulse . . .	68
4.3	Schematic representation of n-th order Bragg diffraction. For coherent coupling between the momentum states $ 0\hbar k\rangle$ and $ 2n\hbar k\rangle$, energy conservation necessitates that $\hbar n\Delta\omega_n = \frac{(2n\hbar k)^2}{2m}$. The energy levels are indicated by their transverse momentum states, expressed in units of $\hbar k$. The corresponding detunings for the ground and excited states are represented by Δ_i	69
4.4	Higher Order Bragg Diffraction. (a) Image showing higher order Bragg diffraction of the condensate. (b) Rabi oscillation of 6th order Bragg diffraction.	70

4.5	Bragg spectroscopy of Bose-Einstein condensates in momentum space. In each sequence from top to bottom, the duration of the box-shaped Bragg pulses is fixed at $\tau = 100 \mu s$, while the detuning $\Delta\omega$ is varied from 8 kHz to 21 kHz. The momentum distribution is observed after time of flight of $200 \mu s$. Atoms that are diffracted are highlighted with a yellow box, and the corresponding zeroth order is marked in green box.	72
4.6	Atom interferometer diagram depicting the atom's position. The vertical axis is the position of the atom in the free fall trajectory of the atoms and the horizontal axis represent the time taken in the interferometric sequence.	75
4.7	Schematic of the Mach-Zehnder Bragg Interferometer Experiment. The following pulse sequence illustrates the consecutive Bragg pulses. In this sequence, $\pi/2 = 50 \mu s$, $\pi = 100 \mu s$, and the interferogram time is $300 \mu s$.	80
4.8	Population oscillation of the condensate. Oscillations in the population of diffracted order of the condensate in the $ 4\hbar k\rangle$ momentum state as a function of the phase shift ϕ of the last Bragg pulse. The interferogram time between the centers of successive Bragg pulses is $\Delta T = 300 \mu s$.	81
5.2	Transfer function $ H(2\pi f) ^2$ for a Mach-Zehnder sequence $\pi/2 - \pi - \pi/2$ with a Rabi frequency of $2\pi \times 5$ kHz for an interferometric time of 10 ms. $\frac{n}{T+2\tau_R}$ represents the frequencies where the sensitivity diminishes, where n is an integer and $\frac{\sqrt{3}\Omega_R}{6\pi}$ corresponds to the cutoff frequency for a finite duration of Bragg pulses.	89

5.3	Schematic diagram of generation of Bragg beams and interferometric signal for two different configurations. (a) Top figure depicts the block diagram of generation of Bragg pulses using two different AOMs driven by AFGs which are phase locked using Rubidium atomic clock. The laser is locked to the Rubidium transition line which is not shown in the diagram. PD: photodiode, SA: spectrum analyser, AFG: arbitrary function generator. Bottom figure shows the population oscillation of first order momentum state versus sweep rate in terms of acceleration for interferometer time $T = 3.4$ ms. (b) Top figure depicts the block diagram of generation of Bragg pulses using single AOM driven by AFG which are phase locked. Bottom figure which is adapted from our previous work [7] shows the population oscillation of first order momentum state versus sweep rate in terms of acceleration for interferometer time $T = 10$ ms for single AOM configuration. Reproduced with permission from J Indian Inst Sci 103, 609–632 (2023), Springer Nature. Inset: Precise scanning of sweep rate along with the interferometric signal.	92
5.4	The power spectrum of the Bragg beams is examined for various configurations. In this analysis, the dashed red line represents the configuration involving two co-propagating laser beams diffracted from separate AOMs as shown in Figure 5.3 (a), the dot-dashed green line represents the configuration of Bragg beams diffracted from separate AOMs and coupled into a single fiber to reduce the differential phase noise and the solid blue line corresponds to the configuration utilizing a single AOM as shown in the Figure 5.3(b), with a frequency resolution of 500 Hz.	94
5.5	Phase Noise spectrum of the Bragg beams for single AOM configuration and dual AOM configuration coupled to a single fiber with 25 Hz resolution bandwidth.	95
5.6	Allan deviation of the gravity measurements for interferometric time $T = 10$ ms. The dashed line corresponds to a short-term sensitivity of $1360 \mu\text{Gal}/\sqrt{\text{Hz}}$ for 1 second.	96

6.1	Schematic pulse diagram of BEC based Atom Interferometer and its space time trajectories. a)Three Pulse Scheme b) Four Pulse Scheme . .	103
6.2	Schematic pulse diagram of simultaneous BEC-based Atom Interferometer and its space-time trajectories for Four Pulse Scheme. The orange and grey color arrows indicate the Bragg pulses for splitting, redirecting, and merging. The orange beam is coupled with two different frequencies of ω_1 and ω_2 whereas the grey beam consists of one frequency ω_0 . The atoms start from a position (a) where a $\pi/2$ pulse is applied. The atoms split into two momentum states simultaneously and symmetrically with a recoil momentum of $\pm 2\hbar k$. Subsequently, we apply $\pi - \pi - \pi/2$ pulses with a time interval of $T - 2T - T$ after the first π pulse. The red arrow and circles denote the trajectories of the negative momentum interferometer, whereas the blue arrows and circles denote the trajectories of the positive momentum interferometer. Since the interferometer time is less enough than after the last $\pi/2$ pulse, the zeroth momentum state is not separated enough, so we see them overlapping with each other. Here g is the direction of gravity.	104
6.3	a)BEC after π pulse, b)BEC after $\pi/2$ pulse, c)Rabi oscillation for two different momentum states	106
6.4	Normalised population oscillation of $\pm 2\hbar k$ for four pulse method. a) $T=450\mu s$, b) $T=1$ ms	106
7.1	Compact setup of a Rubidium MOT.	110
7.2	Laser system for compact quantum gravimeter using telecom laser.	111

List of Tables

1.1	Different capabilities of atom based quantum sensors	3
1.2	Classification of accelerometer and gyroscope performances. The position accuracy is calculated after a one-hour integration period, assuming there are no initial errors in position, velocity, or attitude. The table is cited from [5]	23
2.1	Phase shifts for different transitions	44
3.1	Approximate values for typical vacuum parameters for several gas flow regimes.	46
3.2	Vacuum levels with their respective pressure and particle density. .	47

Chapter 1

Introduction

1.1 Exploring Quantum Sensors for Precise Measurements

In the realm of modern physics, the advent of quantum mechanics has revolutionized our understanding of the fundamental nature of the universe. Quantum mechanics, with its probabilistic nature and intriguing phenomena such as superposition and entanglement, has not only deepened our comprehension of the microscopic world but has also paved the way for transformative technological advancements. One such groundbreaking application lies in the realm of quantum sensors [8], which harness the principles of quantum mechanics to achieve unparalleled levels of precision in measurement.

Traditional sensors have played a pivotal role in countless fields, from navigation systems and medical diagnostics to environmental monitoring and fundamental research. However, as demands for higher accuracy [9], sensitivity [10], and resolution [11] continue to escalate, the limitations of classical sensing technologies become increasingly apparent. Quantum sensors offer a promising solution to these challenges by exploiting quantum phenomena to achieve measurements that were once deemed unattainable.

At the heart of quantum sensors lies the principle of quantum superposition, wherein a quantum system can exist in multiple states simultaneously. By delicately manipulating and interrogating quantum states, quantum sensors can achieve levels of sensitivity and precision that surpass those of their classical counterparts. Moreover, the

phenomenon of quantum entanglement enables correlations between particles over vast distances, enabling the development of distributed sensing networks with unprecedented capabilities.

In this thesis, we explored atom interferometers, which are matter-wave interferometers analogous to the well-known optical interferometers. Similar to their optical counterparts, atom interferometers function by splitting an ensemble of cold atoms into a superposition of two states that travel through separate interferometer arms, accumulating relative phase differences. These states are then recombined to produce interference. In optical interferometers, this process is achieved using mirrors and beam splitters, whereas in matter-wave interferometers, pulses of an optical lattice are used.

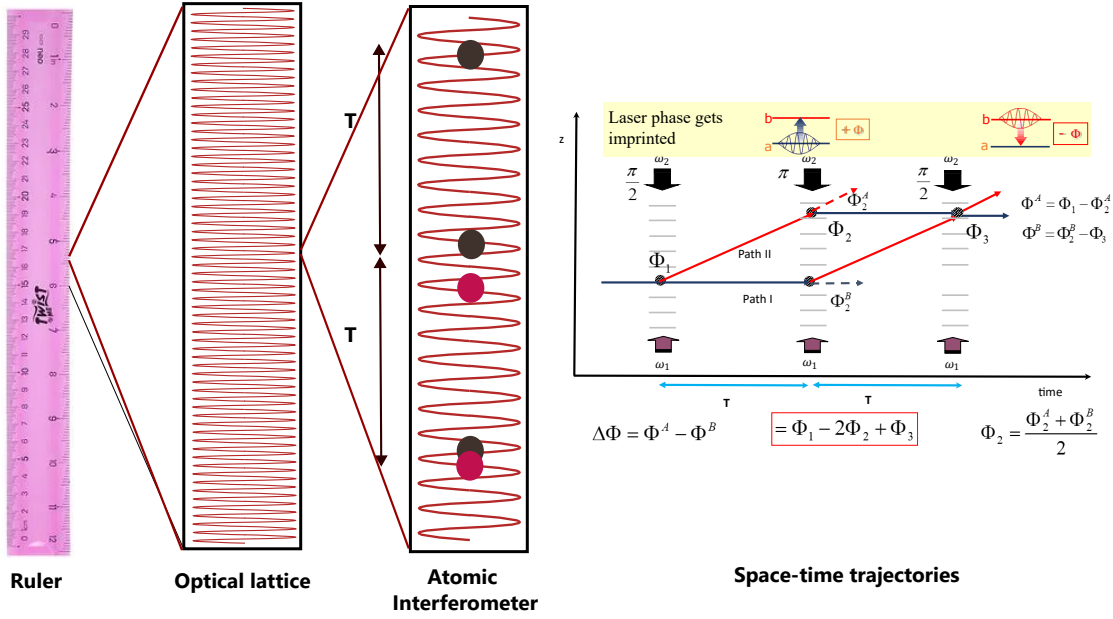


Figure 1.1: **Classical and quantum sensor comparison:** The working principle of a cold-atom accelerometer or interferometer involves using a standing wave along with an ensemble of cold atoms. The standing wave acts as an optical ruler, guiding the atoms as they fall freely through the system. During their descent, the atoms interact with a first beam splitter, a mirror pulse, and a final beam splitter. This interaction causes a phase shift, which can be detected at the output ports of the atom interferometer.

1.1.1 Inertial sensing using cold atom sensors

The foundation for cold atom sensors was laid by the groundbreaking work of Steven Chu, Claude Cohen-Tannoudji, and William D. Phillips [12], who were awarded the

Nobel Prize in Physics in 1997 for their development of methods to cool and trap atoms with laser light. Building upon the groundbreaking work, M. Kasevich and S. Chu in 1991 [13], demonstrated the light-pulse atom interferometry, employing laser-cooled atoms, which has evolved into a highly effective method for achieving precise measurements. Over the last three decades, significant advancements have been made in the realms of inertial sensing and the exploration of fundamental physics through pioneering experiments. In 1995, Eric Cornell, Carl Wieman, and Wolfgang Ketterle [14, 15] achieved a major breakthrough by successfully creating the first Bose-Einstein condensate (BEC) in a dilute gas of rubidium atoms. BEC is a state of matter that occurs at extremely low temperatures, where quantum effects become dominant, and all atoms occupy the same quantum state. This milestone marked the birth of a new era in atomic physics and laid the groundwork for atom sensors using BEC.

Inertial sensing covers the measurement of the local gravitational acceleration, rotations as the rotation of the Earth, as well as gravity gradiometry, by a differential read out of two spatially separated atom interferometers. Table 1.1 presents a reference for various sensors utilizing atom-based platforms.

Quantity Measured	Sensor Type	Achieved Sensitivity	No of atoms
Gravity	Cold atoms	$\sim 75 \times 10^{-8} \text{ ms}^{-2}/\sqrt{\text{Hz}}$	$\sim 10^7$ [16]
Gradiometer	Cold atoms	$\sim 466 \times 10^{-9} \text{ s}^{-2}/\sqrt{\text{Hz}}$	$\sim 10^8$ [11]
Time	Optical clocks	$\sim 4.4 \times 10^{-18} / \sqrt{\text{Hz}}$	$\sim 10^5$ [17]
Rotation	Cold atoms	$\sim 100 \times 10^{-9} \text{ rad/sec}/\sqrt{\text{Hz}}$	$\sim 2 \times 10^7$ NA [18]
Magnetic Field	BEC	$\sim 120 \times 10^{-12} \text{ T/m}/\sqrt{\text{Hz}}$	$\sim 2 \times 10^6$ [19]
Rydberg Sensor	Vapour cell	$\sim 55 \times 10^{-9} \text{ nVcm}^{-1}/\sqrt{\text{Hz}}$	[20]

Table 1.1: Different capabilities of atom based quantum sensors

Most sensors mentioned in table 1.1 are based on atom interferometer and they share a conceptual resemblance to optical Mach-Zehnder interferometers [21]. In such configurations, a beamsplitter divides a light beam into two paths, which subsequently converge after reflecting from mirrors. Upon their reunion, these paths intertwine at another beamsplitter, leading to observable interference patterns in the power output from the

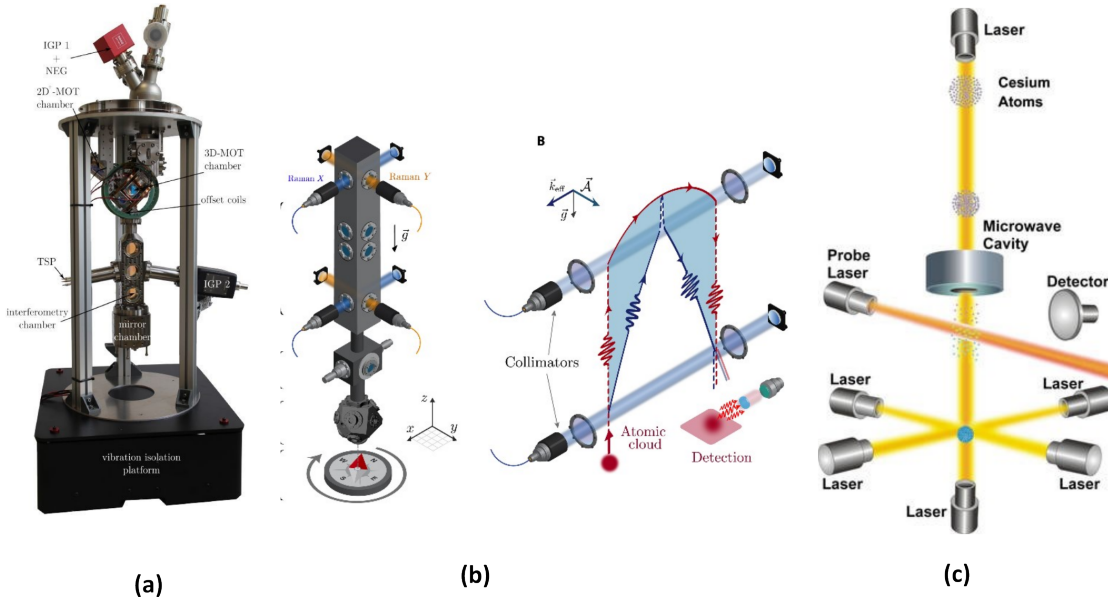


Figure 1.2: **Atom Interferometer for Various Applications:** **Fig (a):** Atomic gravimeter adapted from [1]. **Fig (b):** Rotation sensor adapted from [2]. **Fig (c):** Atomic clock adapted from NIST-F1 Cesium Fountain Clock **Credit: NIST.**

final beamsplitter's two ports.

Contemporary atom interferometers predominantly employ light-pulse atom-optical elements, where laser light takes on the role traditionally held by mirrors and beamsplitters in manipulating matter waves. This paradigm shift effectively exchanges the traditional function of light and matter in an optical interferometer.

When laser light, resonating with an atomic transition, interacts with an atom, it coherently induces oscillations in the populations of the ground and excited states, a phenomenon known as Rabi oscillations. This is explained in detail in Chapter 4. Initiating with atoms in the ground state and timing the laser pulse to cease after a quarter of an oscillation, corresponding to a $\pi/2$ phase evolution of the Rabi oscillation, results in placing the atoms into an equal-probability superposition of the ground and excited states. This operation, termed a ' $\pi/2$ pulse,' effectively acts as a 50:50 beamsplitter. Similarly, a ' π pulse,' timed to last half an oscillation, reverses the population of the ground and excited states, functioning akin to a mirror. Finally, one observes the oscillation in the population of atoms after the completion of the interferometer.

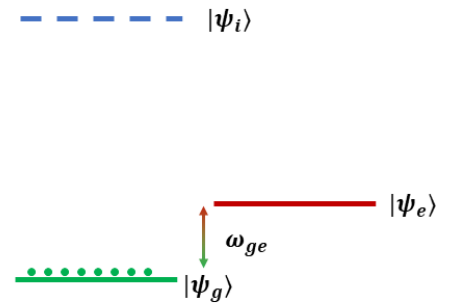
1.2 Atom Interferometer (AI)

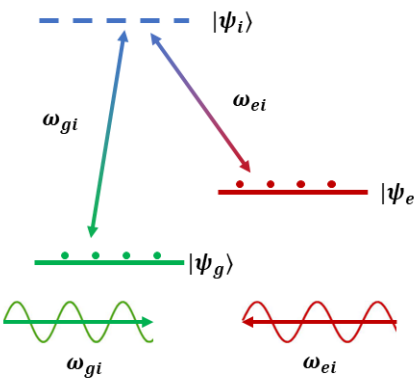
Over the last decade, atom interferometer (AI)-based quantum sensors have rapidly evolved, showcasing diverse measurement schemes and implementations for high-precision measurements. Utilized in various applications today, atom interferometers (AI) remain pivotal contributors to precision measurement frontiers, even on ground. Cold clouds of atoms, cooled to mere tens of microkelvin and nanokelvin using laser cooling, approach absolute zero, offer an ultra-sensitive test matter wave for interferometric measurements. Atom interferometers (AIs) have demonstrated their exceptional sensitivity as a probe for inertial forces, including accelerations and rotations. By dropping cooled atom clouds, precise measurements of local gravitational acceleration have been achieved with an absolute uncertainty of $\sim 75 \times 10^{-8} \text{ ms}^{-2}/\sqrt{\text{Hz}}$ [16]. Additionally, Sagnac-type interferometers have detected minuscule rotations, typically with sensitivities closer to $10^{-9} \text{ rad/s}/\sqrt{\text{Hz}}$ [18]. Gravity gradiometers, designed to gauge gravitational differences between two points using a shared reference frame, have been developed with an absolute sensitivity of $\sim 466 \times 10^{-9} \text{ s}^{-2}/\sqrt{\text{Hz}}$ [11].

1.2.1 Stepwise Explanation of an Atom Interferometer

Within this segment, we shall elucidate the principle of atom interferometry in a comprehensible manner through six sequential steps. This journey will culminate in our understanding of the measurement of acceleration due to gravity and other fundamental constants.

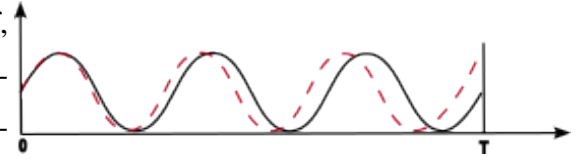
1. **Step 1:** Let's explore a three-level system comprising the ground state $|\psi_g\rangle$, excited state $|\psi_e\rangle$, and an intermediate state $|\psi_i\rangle$. Initially, atoms are prepared in the ground state through cooling and trapping techniques.

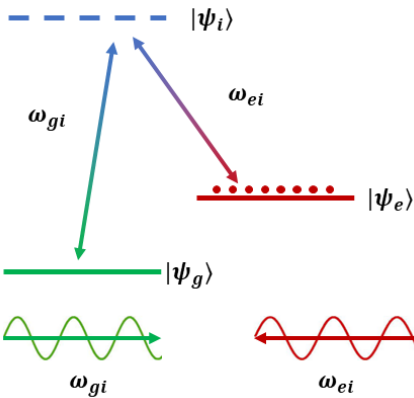


2. 
- Step 2:** A laser pulse, incorporating two distinct frequencies, with frequency difference equal to the frequency difference between the ground and intermediate state, is directed at the atom, causing it to enter a superposition state encompassing both the ground state $|\psi_g\rangle$ and the excited state $|\psi_e\rangle$.
- $$|\psi\rangle = \frac{1}{\sqrt{2}}(|\psi_g\rangle + \exp^{i\omega_{ge}t} |\psi_e\rangle) \quad (1.1)$$

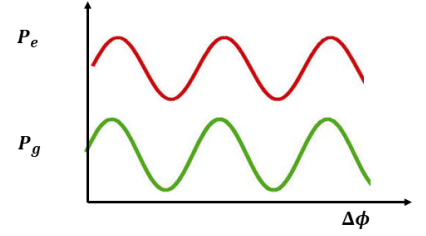
This type of pulse is referred to as a $\pi/2$ pulse, akin to a beamsplitter in optical interferometry.

- Step 3:** After the first pulse, the atoms evolve freely for a time T , without intervention. The phase accumulated during this period is $\Delta\phi = \int_0^T \omega_{ge} dt$. If,
3. during this interval, the atoms undergo a displacement δx relative to the electromagnetic field radiation produced by a local oscillator, an extra phase shift $\Delta\phi = \mathbf{k} \cdot \delta \mathbf{x}$ is acquired.



4. 
- Step 4:** Thus one can introduce another laser pulse, which transfer the atoms from ground state to excited state and viceversa.
- $$|\psi\rangle = \frac{1}{\sqrt{2}}(\exp^{-i\omega_{ge}t} |\psi_g\rangle + |\psi_e\rangle) \quad (1.2)$$
- This type of pulse is referred to as a π pulse, akin to a mirror in optical interferometry.

- Step 5:** The final step includes the re-combining the two atomic wavefunctions by a $\pi/2$ pulse. The outcome of the atom's final state hinges on the relative phase obtained between the two states. The likelihood of observing the atom in either $|\psi_g\rangle$ or $|\psi_e\rangle$ after the pulse is contingent upon the degree of dephasing and follows the equation:



$$P_e = \frac{1}{2}(1 + \cos(\Delta\phi)) \quad (1.3)$$

6. **Step 6:** A three-pulse interferometer is constructed by sequentially applying Raman or Bragg pulses separated by a time interval T , consisting of a $\pi/2$ -pulse, a π -pulse, and another $\pi/2$ -pulse. This arrangement induces a phase shift expressed as:

$$\Delta\phi = \phi_1 - 2\phi_2 + \phi_3 \quad (1.4)$$

By analyzing the interference pattern, it's possible to make extremely precise measurements of parameters such as gravitational acceleration, magnetic fields, and inertial forces.

1.3 Different types of Atom Interferometer

1.3.1 Mach-Zehnder Atom Interferometer

The Mach-Zehnder atom interferometer [22] is one of the simplest and most common types. It is similar to the optical Mach-Zehnder interferometer but uses atoms instead of photons. In this interferometer, a beam of atoms is split into two separate paths using laser pulses. These paths are then recombined to produce an interference pattern that depends on the phase difference accumulated along the two paths as shown in figure 1.1. The phase difference can be influenced by external forces like gravity, enabling precision measurements.

1.3.2 Ramsey-Bordé Atom Interferometer

The Ramsey-Bordé interferometer [23] is a variant that uses two pairs of laser pulses to create an atom interferometer. The first pair of pulses splits and recombines the atomic wave packets, while the second pair, does the same as shown in figure 1.3. The interference pattern generated by this setup is highly sensitive to the atomic velocity and can be used to measure atomic recoil, fundamental constants, and time. This type of interferometer is widely used in precision spectroscopy, determination of fine structure constant and measurements of atomic transitions.

1.3.3 Multi-Path Atom Interferometer

Multi-path atom interferometers [24, 25] extend the basic two-path design by splitting the atom beam into more than two paths, creating a more complex interference pattern. These interferometers can provide higher sensitivity and accuracy for certain measurements by exploiting the additional phase information available from the multiple paths. They are used in fundamental research applications, such as exploring quantum coherence and decoherence.

1.4 Different cold atom sensor applications

1.4.1 Determination of the Fine Structure Constant

Calculating the fine structure constant α [26] using cold atoms has become an exciting area in atomic physics. This fundamental constant, in quantum electrodynamics, determines the strength of electromagnetic interaction between charged particles [27]. It shows the relationship between the binding energy of an electron-proton system and the electron's rest energy, expressed through a formula:

$$\alpha^2 = \frac{2R_\infty}{c} \frac{m_{Atom}}{m_e} \frac{h}{m_{Atom}} \quad (1.5)$$

where h is the Planck constant, c is the speed of light in vacuum, R_∞ is the Rydberg constant, and m_e is the mass of an electron.

Atom interferometers measure α based on measuring the recoil kinetic energy transferred from or to an atom of mass m_{Atom} after scattering a photon that carries mo-

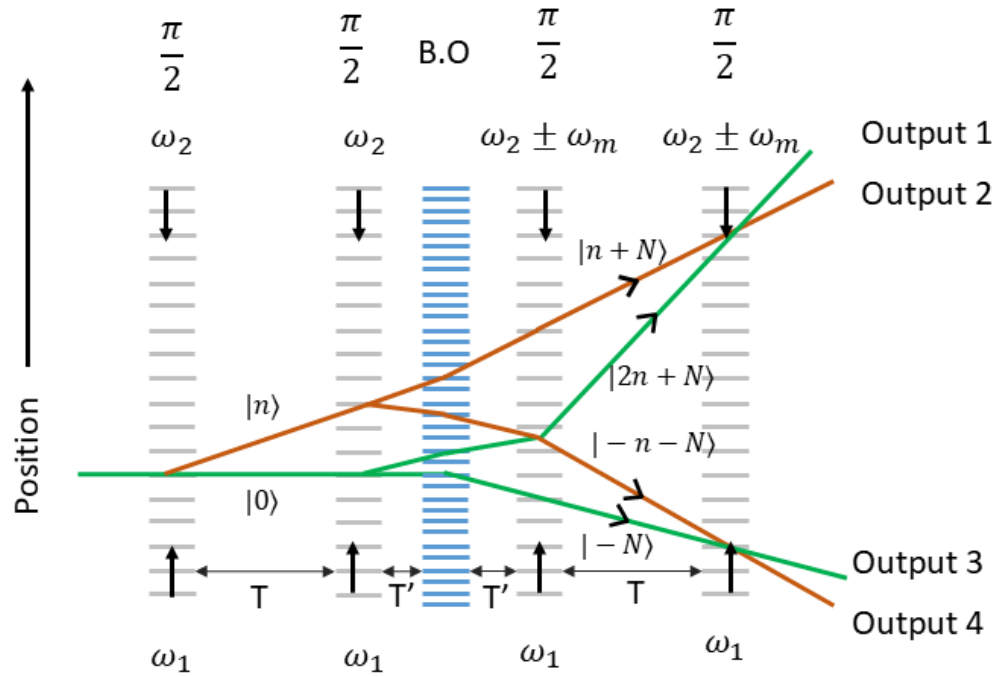


Figure 1.3: **Simultaneous Conjugate Ramsey-Borde Interferometers.** Solid lines show the trajectories of the atoms, while dashed lines indicate the laser pulses with their respective frequencies. The optical lattices are formed by two laser pulses contains two different frequencies, ω_1 , ω_2 and ω_1 , $\omega_2 \pm \omega_m$. BO stands for Bloch oscillations which helps us in creating an accelerating optical lattice acquiring momentum from two photon recoils per BO. $|n\rangle$ represents a momentum eigenstate with momentum $2n\hbar k$.

momentum $\hbar k$ [28], where $\hbar = h/2\pi$ is the reduced Planck constant and k is the photon wavenumber. This recoil kinetic energy is given by ω_r , where $\omega_r = \frac{\hbar k^2}{2m_{Atom}}$ is the recoil frequency. Introducing an extension to the conventional laser-pulse sequence within an atom interferometer, involving the incorporation of four $\pi/2$ pulses, leads to the formation of two distinct closed interferometers as shown in figure 1.3. The disparity between the phase shifts [29] experienced by these two interferometers correlates directly with the recoil energy accumulated during the beamsplitter $\pi/2$ pulses. By amalgamating this innovative interferometer configuration with an accurate determination of the wavelength of the laser light utilized for the pulses, it becomes feasible to derive a precise measurement of h/m_{Atom} [30].

1.4.2 Testing the equivalence principle:

The equivalence principle asserts that local physical phenomena in a freely falling frame are equivalent to those in the absence of gravitational fields, as long as tidal effects can be neglected [31, 32]. The discrepancy in acceleration observed between two test masses in free fall, which signifies a departure from the universality of free fall (UFF), is a key aspect of the equivalence principle. A comprehensive recent overview explores both the theoretical underpinnings and practical implications of the equivalence principle, alongside its experimental validations [33]. Typically, investigations into the weak equivalence principle involve examining the minute difference in acceleration, denoted as $|a_1 - a_2|$, between two dissimilar freely falling test masses. Any potential deviation of the weak equivalence principle are quantified through the *Eötvös* parameter η :

$$\eta = 2 \left| \frac{a_1 - a_2}{a_1 + a_2} \right| \quad (1.6)$$

According to the Weak Equivalence Principle (WEP), the *Eötvös* parameter should be zero, indicating that the accelerations experienced by two test masses of different composition or material are equal when subjected to the same gravitational field. However, deviations from zero in the *Eötvös* parameter would indicate a violation of the Weak Equivalence Principle. Such deviations could arise from new physics beyond the standard framework of general relativity, such as theories involving extra dimensions or modifications to the gravitational interaction.

Various experiments have been conducted to assess the weak equivalence principle. On Earth, torsion balances have yielded the most stringent constraints on potential violations, achieving a relative precision of approximately 10^{-13} [34]. In space, the MICROSCOPE mission stands out for its highly accurate test of the weak equivalence principle, reaching a relative precision of around 10^{-14} [35]. Additionally, lunar laser ranging measurements have also established stringent bounds. Notably, several other experiments rely on the weak equivalence principle for their validity.

Atom interferometers present a unique and complementary method for investigating the equivalence principle [36, 37]. One key advantage is the intrinsic isotopic purity of the test samples, coupled with their well-defined spin states. This inherent purity allows for a meticulous exploration of potential violations of the equivalence principle related to spin-dependence [38]. By comparing results obtained with different spin polarizations, researchers can scrutinize for deviations from the Universality of Free Fall (UFF). Moreover, atom interferometers offer access to atomic elements [39] that are challenging to employ as macroscopic test masses due to technical constraints. This capability broadens the scope of investigation, particularly in terms of exploring atomic elements or isotopes with varying neutron and proton numbers. Consequently, atom interferometers facilitate the expansion of the parameter space, thereby enhancing our ability to probe the fundamental principles governing gravitational interactions.

1.4.3 Gravitational wave detection:

Atom interferometry presents an alternative avenue to traditional laser interferometry for detecting gravitational waves, offering a complementary approach [40]. By employing two atom interferometers manipulated by the same light field, these systems can function as differential phase meters, tracking the distance traveled by the light field [41], similar to the figure 1.3. Building upon this principle, proposals for space-borne detectors which aim to achieve performance levels akin to the laser interferometer utilized in the Laser Interferometer Space Antenna (LISA) project [42].

To bridge the frequency gap between ground-based laser interferometers such as Virgo or AdvLIGO [43], and LISA, atom interferometers have been suggested to be operated at 0.1 – 10 Hz band. Variations in setup, whether vertical or horizontal baselines,

have been explored, with ongoing efforts towards the latter configuration within the Matter-wave laser Interferometric Gravitation Antenna (MIGA) [44] consortium. The European Laboratory for Gravitation and Atom-Interferometric Research (ELGAR) facility is pioneering the development of long-baseline infrastructure employing quantum physics to probe spacetime and gravitation. Utilizing a network of atom interferometers, it aims to discern gravitational-wave signals in the 0.1 – 10 Hz range while filtering out Newtonian gravitational noise, filling a frequency band which was overlooked by existing gravitational-wave detectors [45]. Beyond gravitational wave detection, ELGAR is poised to contribute to various scientific inquiries, including monitoring the Earth's gravitational field evolution and three-dimensional rotation rate over time.

1.4.4 Measuring gravity with atoms

In an absolute gravimeter, the determination of local gravity acceleration relies on tracking the displacement of a freely falling test mass [13]. In classical gravimeters, this test mass, typically a macroscopic object, is optically monitored. However, in atom interferometers, a collection of laser-cooled atoms serves as the test mass. Their displacement is observed through their interaction with a stationary two-photon Raman [13, 46] or Bragg [47, 48] transitions, or single-photon transitions on ultranarrow lines [49] functioning essentially as an 'optical ruler' as shown in figure 1.1. A simplified overview of the timing sequence involved in such measurements is provided here for introductory purposes. The gravity acceleration g produces a phase change at the interferometer output which is given as [50]:

$$\Delta\phi = k g T^2 \quad (1.7)$$

where, k represents the effective wavevector responsible for splitting and recombining the wavepacket of light, while T denotes the duration of free-fall experienced by the atom between successive laser pulses.

Alternative methods have been explored to measure g using atom interferometry, including experiments with Bloch oscillations [51]. In these experiments, cold atoms are trapped in a vertical optical lattice [52]. The gravitational force and the periodic potential from the laser standing wave result in oscillations in momentum space, characterized

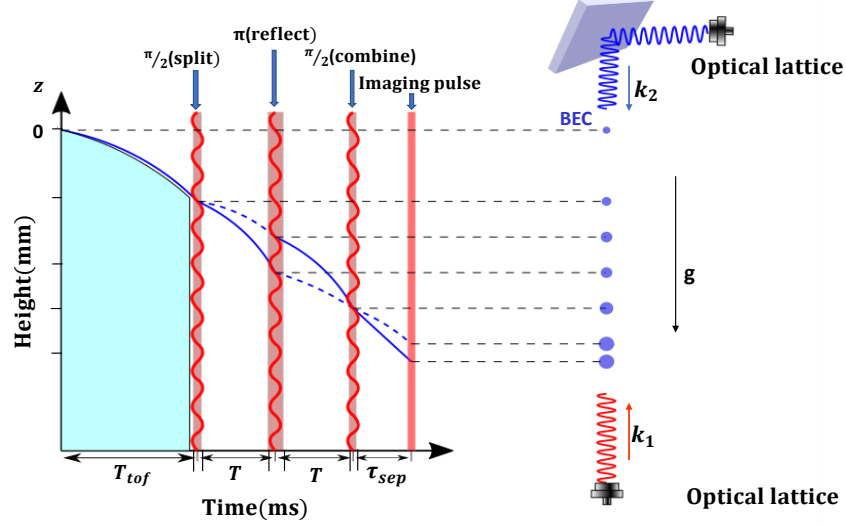


Figure 1.4: **Schematic diagram of Bose Einstein Condensate (BEC) based Atom Interferometer and its space time trajectories.** The blue dots represents BEC with ballistic expansion after release from the dipole trap. The experiment runs in three steps. (i) The conversion of mean field energy into kinetic energy of BEC during time of flight T_{tof} (ii) the MZI with different interferometric time ranging from ms (iii) the final pulse for detection after allowing the wave packets to separate with τ_{sep} ms.

by a frequency ν_{BO} as:

$$\nu_{BO} = \frac{mg\lambda}{2h} \quad (1.8)$$

Here, m represents the atomic mass, λ denotes the wavelength of the laser creating the lattice, and h is Planck's constant. By determining the frequency of the Bloch oscillations, the gravitational acceleration g can be calculated.

In this thesis, I will focus on demonstrating an atom interferometer utilizing Bragg diffraction [53] and employ it to measure the acceleration due to gravity.

1.4.5 Quantum gyroscope with atoms

From the beginning of the 20th century onwards, numerous adaptations of Georges Sagnac's [54] original experiments have emerged. These experiments leveraged the 'Sagnac' interference phenomenon to assess rotational movement, employing both light and atoms in their setups. Gyroscopes that utilize this effect measure a rotation rate, Ω ,

through a phase shift between the two paths of an interferometer [55]. The Sagnac phase shift, applicable to both photons and massive particles, can be expressed as:

$$\Phi_{\text{sagnac}} = \frac{4\pi E}{hc^2} \mathbf{A} \cdot \boldsymbol{\Omega} \quad (1.9)$$

The vector \mathbf{A} represents the area of the Sagnac loop, perpendicular to the plane of the interferometer and corresponding to the area enclosed by its arms. The energy E is defined as follows: for a photon, it is $\hbar\omega$, and for a particle with rest mass M , it is Mc^2 . Equation 1.9 indicates that the Sagnac phase shift for a matter-wave interferometer is greater by a factor of $\frac{Mc^2}{\hbar\omega} \sim 10^{11}$ compared to an optical interferometer of the same area. This factor becomes significant when comparing the rest energy of an atom to that of an optical photon in the visible spectrum, highlighting the exceptional sensitivity of atom-based sensors to rotational motion [55]. Figure 1.5 provides the basic illustration of an atom based rotation sensor. More detailed work is provided in the chapter 7.

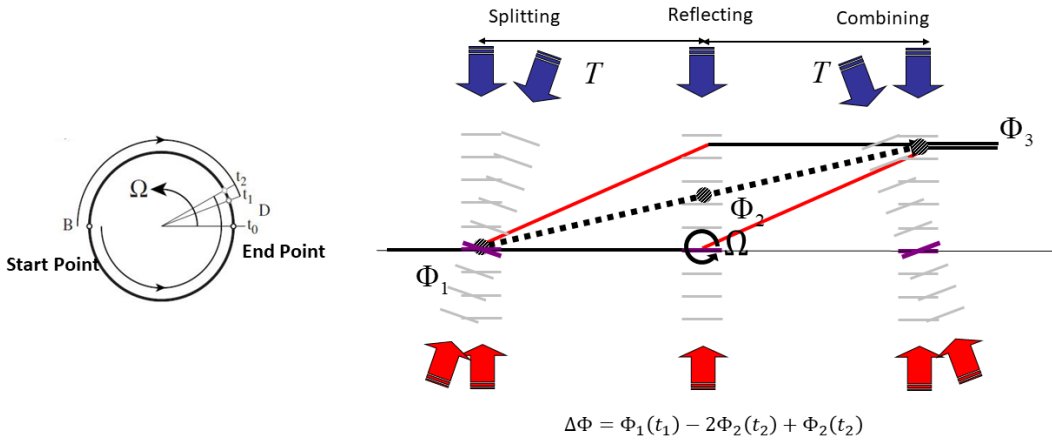


Figure 1.5: Atom based Sagnac interferometer. Schematic of a matter-wave Sagnac interferometer based on two-photon Raman transitions. An optical illustration of atom interferometer is shown in the left diagram. An atom in state $|1\rangle$, with center-of-mass velocity $v = \frac{p}{M}$, is subjected to a sequence of counter-propagating laser pulses that are rotating relative to the atomic trajectory at a constant rate Ω .

1.5 Emerging techniques to enhance the sensitivity in Atom Interferometer

In the last decade, there have been huge efforts to develop new techniques to enhance the sensitivity of cold atoms as well as ultracold atom-based interferometers. Cutting-edge techniques such as large momentum transfer, Bloch oscillations, double Bragg diffraction, and momentum entangled state preparation for the interferometers are a few of them. There have been efforts to improve precision, accuracy, stability, and in decreasing the size of AIs. Here we discuss briefly how entanglement and large momentum transfer play crucial roles in boosting the sensitivity of AIs [56].

1.5.1 Quantum Entanglement in Atom Interferometry

The Standard Quantum Limit (SQL) represents a fundamental limit on the precision of measurements imposed by quantum mechanics, particularly in interferometry and metrology. It originates from the Heisenberg uncertainty principle, which dictates that there is a trade-off between the precision of measurements of conjugate variables, such as position and momentum or phase and number.

In the context of interferometry, the SQL sets the minimum uncertainty in phase measurements when using a coherent state of light or matter waves. The uncertainty in phase, $\Delta\phi$, for a coherent state is given by:

$$\Delta\phi \geq \frac{1}{\sqrt{N}}$$

where N is the number of photons or atoms used in the interferometer. This expression implies that the precision improves as the square root of the number of particles increases, but this scaling represents the best possible sensitivity achievable with classical resources. The SQL is derived from the quantum noise that arises due to the quantization of the electromagnetic field or atomic states. In a simple interferometric setup, the phase uncertainty can also be related to the uncertainties in the amplitude quadratures of the light field, ΔX_1 and ΔX_2 , through the following relation:

$$\Delta X_1 \Delta X_2 \geq \frac{1}{2}$$

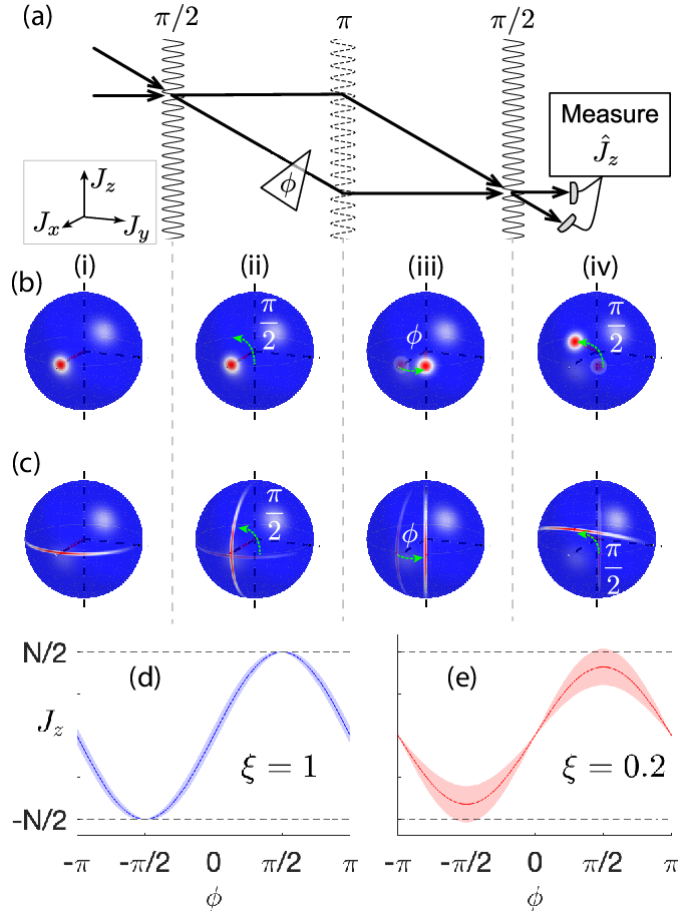


Figure 1.6: **Spin squeezing in an atom interferometer:** a) Schematic diagram of an atom interferometer, b) and c) Coherent Spin State evolution of non-entangled states and entangled states, d) and e) The output signal for phase measurement above and below SQL. (Reprinted from [3], with the permission of AIP Publishing)

where X_1 and X_2 are the quadrature amplitudes of the field. This inequality is a manifestation of the Heisenberg uncertainty principle.

To surpass the SQL, quantum-enhanced techniques such as squeezed states or entangled particles can be employed. For instance, in a squeezed state, the uncertainty in one quadrature is reduced at the expense of increased uncertainty in the conjugate quadrature, allowing for phase measurements with precision below the SQL:

$$\Delta\phi_{\text{squeezed}} \geq \frac{1}{\sqrt{N}} e^{-r}$$

where r is the squeezing parameter, indicating the degree of noise reduction in the

phase quadrature.

Surpassing the SQL is crucial for applications in precision measurements, such as gravitational wave detection, where the ability to measure minute displacements or phase shifts with extremely high accuracy is necessary. The development of techniques to beat the SQL has significant implications for advancing the sensitivity of devices like atomic clocks, magnetometers, and other quantum sensors. Quantum entanglement of atoms in an interferometer provides a promising tool to enhance the sensitivity beyond SQL through relative phase measurements. The early experiments which demonstrated the spin squeezing and momentum entanglement for metrological measurements are given in [57–59].

In an atom interferometer the relative phase difference between two momentum states is determined through some observable \hat{S} related to ϕ as $\Delta\phi = \frac{\sqrt{\text{Var}(\hat{S})}}{|\partial\hat{S}/\partial\phi|} = \frac{\xi}{\sqrt{N}}$ and ξ quantifies the role of quantum entanglement through enhancement of sensitivity. Fig. 1.6 shows the diagram of a quantum enhanced signal in atom interferometry. In the case of Quantum Gravimeter, where atoms fall under gravity in the standard Mach-Zehnder interferometer configuration, one can relate the acceleration due to gravity with the phase of an interferometer as $\phi = \mathbf{k} \cdot \mathbf{g}T^2$. For a quantum-enhanced signal through quantum entanglement the sensitivity in acceleration due to gravity can be seen as $\Delta g = \frac{\xi}{\sqrt{N}k_{||}T^2}$ where N is the number of atoms, $k_{||}$ is the component of \mathbf{k} parallel to \mathbf{g} . Similarly for a rotation sensor where the phase shift is given as $\phi = 2m\mathbf{\Omega} \cdot \mathbf{A}/\hbar$, the sensitivity scales as $\Delta\Omega = \frac{\xi\hbar}{\sqrt{N}2mA_{||}}$, where $A_{||}$ is the component of \mathbf{A} parallel to $\mathbf{\Omega}$. Recent developments such as the work reported in [60] show through numerical simulation of spin squeezed ultracold atoms that the sensitivity gain can reach upto 14 dB beyond the SQL limit. The experimental work on the realization of momentum entanglement in atom Interferometry is shown in reference [61]. The article reports on the demonstration of spin squeezing of -3.1 dB in ultracold atoms. Thus, the coming decades can see the quantum-enhanced atomic inertial sensors in a more matured form [56].

1.5.2 Large Momentum Transfer

Another way to enhance the sensitivity is to increase the interferometric area through multi-photon excitation. Methods like multiple two-photon Raman or Bragg transitions,

double Raman or Bragg diffraction, Bloch oscillations or a combination of Bragg and Bloch oscillations [62–66] allow improvements in the sensitivity by increasing the effective separation between the two interfering atomic samples. The disadvantage of this technique, especially with cold atoms is the addition of extra phase noise due to the multi-port nature induced by the effective multi-photon process.

1.6 Real field application of quantum sensors

1.6.1 Geoexploration and Civil engineering

Gravimetry techniques play crucial roles across various fields including metrology, geology, and industrial applications like resource exploration. Traditional absolute gravimeters and absolute gravity gradiometers have historically faced limitations due to mechanical wear and low sampling rates, rendering them inadequate for continuous long-term observations and applications on mobile platforms. The emergence of atom interferometers (AIs) towards the end of the previous century presented a new technological solution. As discussed in previous sections, AIs utilize laser pulses to manipulate groups of atoms within a vacuum, achieving splitting, redirection, and recombination. AIs, devoid of macroscopic moving components, are well-suited for prolonged continuous measurements and high-sampling-rate operations, circumventing thermal and wear effects that degrade measurement precision in classical instruments. Moreover, leveraging atomic standards as references (such as energy levels and associated transitions) enables these instruments to attain precision and stability.

In civil engineering applications, gravity and gravity gradient maps serve as valuable tools for understanding subsurface conditions. The most prominent features typically observed are those exhibiting significant contrasts in mass or density compared to their surroundings, often indicating boundaries between soil and air. Consequently, gravitational anomalies of interest often include features such as mine shafts, tunnels, sinkholes, and pipes. Presently, gravity sensing in the field is predominantly conducted using relative spring-based gravimeters. Conducting micro-gravity surveys before construction can help mitigate additional expenses arising from unexpected subsurface voids. However, such surveys are seldom conducted due to the considerable time required for

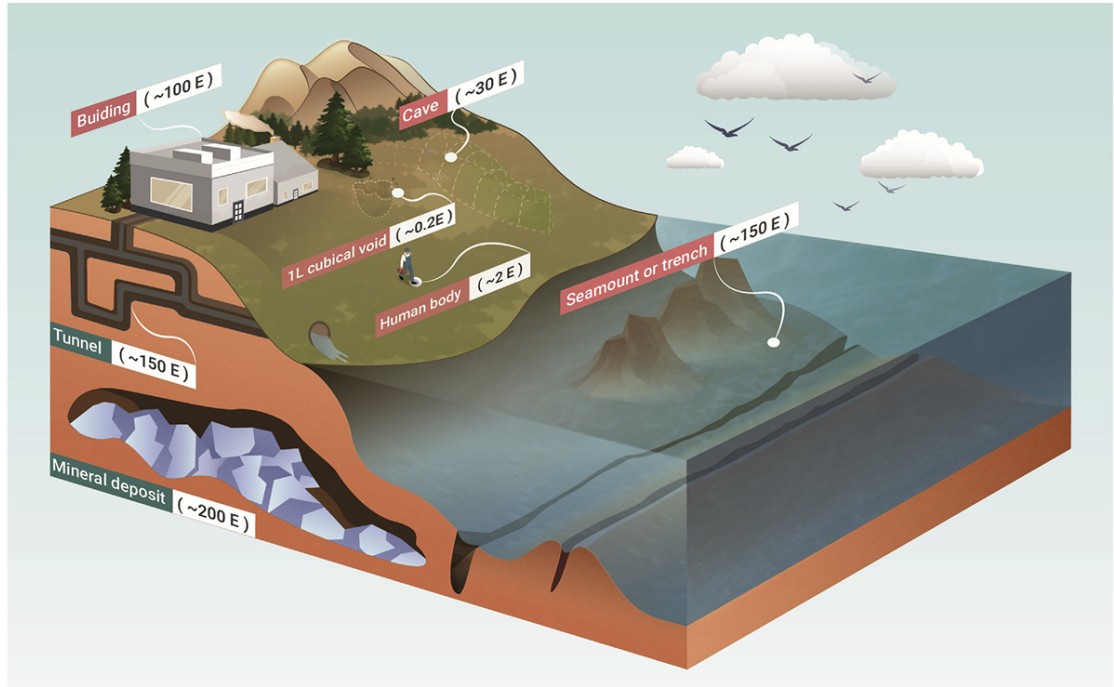


Figure 1.7: The usual magnitudes of gravity gradient anomalies produced by different gravitational sources. ($1E = 10^{-9} s^{-2}$). (This figure is adapted from [4])

measurements. Current gravity mapping techniques entail approximately 10-15 minutes per measurement point, rendering gravity mapping for large-scale civil engineering projects impractical due to time and cost constraints. Atom interferometers (AIs) exhibit the capability to measure gravity gradients equivalent to $1ngs^{-1}$ across a distance of 1 meter. This level of precision, already attainable in laboratory settings, holds the promise of significantly decreasing measurement durations in civil engineering field surveys by more than a hundredfold. This advancement presents a commercially appealing option with considerable economic potential.

1.6.2 Inertial Navigation System

A comprehensive inertial navigation system (INS) integrates an inertial measurement unit (IMU) and a central processing unit (CPU) to autonomously compute trajectories. Its core task involves determining both the position and orientation of a mobile entity from an initially established reference point. An inertial measurement unit (IMU) encompasses a collection of sensors, typically comprising a trio of accelerometers and

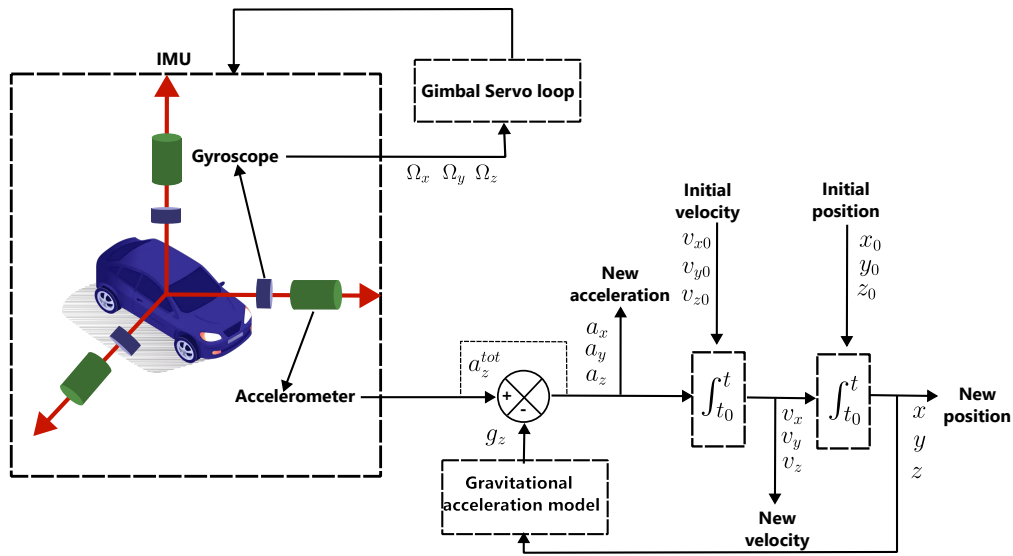


Figure 1.8: **Gimbaled Based INS.** In this system, the INS includes a 3-axis gyroscope that measures angular velocities Ω_x , Ω_y , and Ω_z , which are used to adjust the orientation via a feedback loop controlling the gimbals. At the same time, accelerometers measure accelerations along each axis, a_x , a_y , and a_z^{tot} , while accounting for mobile rotations. The gravitational acceleration g is subtracted from a_z^{tot} to obtain the mobile's true acceleration a_z . By performing a double integration of this acceleration, the position components x , y , and z can be derived.

gyroscopes, complemented by basic electronic components to relay measurements via a communication bus. It assesses acceleration and angular velocity across three axes and constitutes a cornerstone in inertial navigation systems.

Inertial navigation techniques historically encompassed two approaches. In earlier times, when computational capabilities were limited, gimbaled-based INS systems were prevalent [67]. These systems relied on an inertial measurement unit (IMU) mounted on gimbals consisting of three or four rotational frames. Figure 1.8 illustrates the operational schematic of a gimbaled INS. As computational speeds advanced, INS systems transitioned to strap-down configurations [67]. In this setup, the INS is mechanically fixed directly to the moving platform, eliminating the need for gimbals. Figure 1.9 illustrates the operational schematic of a strap-down INS. Inertial navigation systems rely

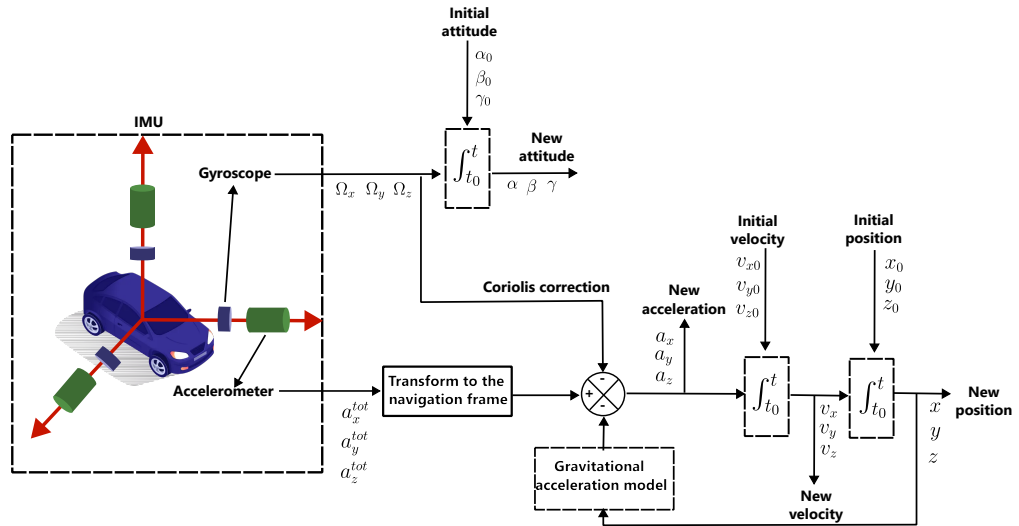


Figure 1.9: **Strapdown based INS.** The gyroscopes provide angular velocities which, when integrated over time from the initial attitude, define the current attitude in terms of Euler angles α , β , and γ . In a strap-down INS, accelerations along three axes are measured, with gravitational acceleration projected onto each component a_x^{tot} , a_y^{tot} , and a_z^{tot} , while Coriolis accelerations introduce perturbations. Initially, these accelerations are projected onto the navigation frame determined by the current Euler angles of the mobile. They are then corrected for Coriolis acceleration, calculated using the gyroscopes, and gravitational acceleration $g(t)$. By double integrating these corrected accelerations, the position components x , y , and z are derived.

on knowing the initial position, velocity, and orientation of the mobile platform with a certain degree of accuracy. To determine the initial position, dead-reckoning instru-

ments like altimeters, odometers, radars, sonars, or lidars are typically used. Another approach is to compare the position to a calibrated reference system, such as a global navigation satellite system (GNSS), terrestrial radio beacons, or by aligning local measurements with established maps, including those that indicate magnetic or gravity field anomalies. Positioning errors in inertial navigation systems stem from various sources. Time integration of accelerations and rotation rates leads to cumulative errors over time. Additionally, these systems are prone to bias drift. The sensor's actual response deviates from linearity and is influenced by the environment. Non-linearities can be addressed using higher-order scale factor models, but calibration is challenging due to their dependence on environmental factors. Table 1.2 displays the performance grades of IMUs, with data assessed over one hour of integration. The table provides the classification of Inertial Measurement Unit (IMU) grades based on their performance metrics, specifically accelerometer bias stability, gyroscope bias stability, and their resulting position accuracies. Below is a brief explanation of the grades:

1. **Consumer Grade:** Used in smartphones, fitness trackers, and other consumer electronics.
2. **Industrial Grade:** Utilized in industrial automation, robotics, and automotive systems.
3. **Tactical Grade:** Found in tactical systems like drones, guided munitions, and mid-level navigation systems.
4. **Intermediate Grade:** Bridges the gap between tactical and navigation grades; used in advanced navigation systems.
5. **Navigation Grade:** Used in aircraft, ships, and advanced navigation systems.
6. **Strategic Grade:** Used in military and strategic systems like missiles and space exploration.

Besides the aforementioned sources of error, the accuracy of the gravity model and gravitational anomalies map plays a crucial role in preventing navigation errors from escalating. Auxiliary sensors and navigation aids, such as feature matching techniques or dead reckoning instruments, prove invaluable in minimizing position errors.

IMU Grade	Accelerometer Bias Stability (g)	Position Accuracy (km)	Gyroscope Bias Stability (rad/s)	Position Accuracy (km)
Consumer	$> 5 \times 10^{-2}$	> 320	$> 5 \times 10^{-4}$	$> 10^4$
Industrial	10^{-2}	64	5×10^{-5}	1000
Tactical	10^{-3}	6.4	5×10^{-6}	100
Intermediate	10^{-4}	0.64	5×10^{-8}	1
Navigation	5×10^{-5}	0.32	$> 5 \times 10^{-8}$	< 1
Strategic	5×10^{-6}	0.032	$> 5 \times 10^{-9}$	< 0.1

Table 1.2: **Classification of accelerometer and gyroscope performances.** The position accuracy is calculated after a one-hour integration period, assuming there are no initial errors in position, velocity, or attitude. **The table is cited from [5]**

Methods of feature matching

Utilizing feature matching techniques involves comparing environmental features with a pre-existing map or database, grounded on physical models and local anomaly surveys [68–70]. Factors like Earth’s non-perfect spherical shape and density variations influence local gravity alongside large-scale movements within the planet. Present-day navigation heavily relies on gravity field matching, facilitated by advanced gravity maps obtained through airborne and space surveys. The widely adopted EGM2008 map [71] combines satellite and terrestrial observations to provide accurate global gravity data. Gravity gradiometry offers even more refined navigation, providing the full gravity gradient tensor $\partial \vec{g} / \partial \vec{r}$ [69], aiding in noise rejection and bias drift mitigation.

Geomagnetic field matching navigation [72] is feasible at certain altitudes, where orbital spacecraft can compare local measurements with a global magnetic model. However, anomalies in the Earth’s geomagnetic field at lower altitudes can be measured to generate a database, although their time-varying nature limits navigation efficiency. Stellar navigation utilizes celestial bodies’ positions, employing star trackers equipped with telescopes and light detectors on gimbals. Hypsometry and bathymetry surveys, measuring land elevation and ocean depth, respectively, contribute to global relief models used in matching navigation through comparisons with local profiles obtained from sonars, lidars, or radars.

Benefits of atomic sensors

Atom-based instruments are emerging as a new class of inertial sensors, offering unparalleled sensitivity, stability, and accuracy. These include devices such as gravimeters, gravity gradiometers, and gyroscopes. The exceptional performance of these sensors is expected to drive significant technological advancements in various domains, including geophysics, metrology, and especially inertial navigation

In the realm of atom interferometry, cold atoms housed within vacuum apparatus function as ideal proof masses in free fall, facilitating precise measurements. Remarkable advancements have been made, resulting in commercial gravimeters utilizing similar technology boasting stability of less than $< 1 \text{ ng}$ and an absolute accuracy of around $< 1 \text{ ng}$, alongside a noise level on the order of $10 \text{ ng}/\sqrt{\text{Hz}}$. Similarly, rotation sensors have achieved an absolute accuracy of 1 nrad/s with noise levels on the order of $10 \text{ nrad}/\sqrt{\text{Hz}}$. Nonetheless, these instruments typically consist of large, intricate laboratory setups necessitating quiet and stable conditions for operation. Applications in field and onboard scenarios demand significant reductions in size, weight, and power consumption of such devices, along with heightened robustness and resistance to environmental disturbances. Notably, significant strides have been made in recent years toward commercializing cold-atom-based sensors.

Several research teams and companies have developed portable cold-atom gravimeters. However, these systems are typically unsuitable for operation during movement and often necessitate a stable and quiet environment to achieve their optimal performance levels. Companies like AOSense [73], Atomionics [74], and Msquared [75] offer commercial products in relatively compact packages, ranging in weight from tens of kilograms to around 100 kilograms. In contrast, a mobile system can function while in motion and within relevant navigation environments. Recently, Simon Templier [76] successfully demonstrated 3D tracking of the acceleration vector using a compact hybrid first quantum accelerometer triad (QuAT).

1.7 Objective of the thesis

The primary objective of this thesis is to explore and develop techniques in atom interferometry, with a particular focus on utilizing ultracold atoms (Bose-Einstein con-

densates) to achieve high-precision measurements. The work begins by providing a comprehensive theoretical understanding of atom interferometry, including the foundational principles of laser cooling, magnetic trapping, and evaporative cooling, as well as the interaction of light with atoms in both two-level and three-level systems.

The thesis then details the experimental procedures for achieving Bose-Einstein condensation in ^{87}Rb , covering the construction of essential components such as the oven, laser systems, and the Ultra-High-Vacuum (UHV) chamber, along with the design of a Bragg laser system specifically for atom interferometry. It further investigates the formation of an atom interferometer, analyzing the Rabi frequency associated with Bragg diffraction in ultracold atoms and conducting Bragg spectroscopy to study the properties of these systems.

The development of an atomic gravimeter using ultracold atoms (BEC) is also a key focus, where a Bragg lattice is employed to create an atom interferometer along the vertical direction. This includes a thorough characterization of phase noise in different Bragg beam configurations and an evaluation of the sensitivity and resolution of the system. Additionally, the thesis introduces and experimentally demonstrates the use of double Bragg diffraction to construct an atomic Sagnac interferometer.

Finally, the thesis summarizes the findings and presents a future outlook, suggesting potential directions for continued research in the field of atom interferometry and its applications in precision measurement technologies. Through these efforts, the thesis aims to contribute to the advancement of atom interferometry as a powerful tool for high-precision measurements.

1.8 Outline of the thesis

Chapter	Description
2	Chapter 2 provides a theoretical overview of the atom interferometer and the foundational principles of laser cooling, magnetic trapping, and evaporative cooling. Additionally, this chapter offers a comprehensive explanation of light-atom interactions in a two-level system, extending to a three-level system that encompasses Raman and Bragg diffraction.
3	Chapter 3 provides a comprehensive description of the experimental setup for achieving ^{87}Rb Bose-Einstein condensation. It details the construction of the oven, laser systems, and the Ultra-High-Vacuum (UHV) chamber. Additionally, this chapter explains the design of the Bragg laser system used in the atom interferometer.
4	Chapter 4 reports the formation of an atom interferometer and the results of the observation of it. It details about the Rabi frequency of a Bragg diffraction of atoms and also talks about the Bragg spectroscopy of ultracold atoms.
5	Chapter 5 provides the detailed study of the development of an atomic gravimeter with ultracold atoms (BEC). It utilises the Bragg lattice to create the atom interferometer along the vertical direction. It also characterizes the phase noise in two different configuration of Bragg beams and finally measures the sensitivity and resolution of the system.
6	Chapter 6 introduces the concept of double Bragg diffraction and demonstrates an experimental procedure for implementing an atomic Sagnac interferometer.
7	Chapter 7 summarizes the work and presents the future outlook.

Chapter 2

Theoretical Background

In this chapter, we provide a concise overview of the theoretical concepts essential for comprehending the research presented in this thesis. The initial portion of this chapter describes briefly about the theory behind trapped Bose gases, fundamentals of laser cooling and trapping. Subsequent sections of this chapter discusses and delve into the theoretical frameworks of light atom interaction where we first discuss about the interaction of an two-level atomic ensemble with a light field and specifically with light pulse and secondly, we extend it to three level system where we emphasis on the phase evolution during the sequence [77].

2.1 A brief overview of cold atoms and Bose-Einstein Condensate.

In the 1970s, A. Ashkin [78] reported the initial observation of freely suspended particles experiencing acceleration due to radiation pressure from continuous wave (cw) visible laser light. Hänsch and Schawlow (1975) [79] along with Wineland and Dehmelt (1975) [80] recognized the potential of such light sources to exert significant forces on atoms, laying the groundwork for potential cooling applications. Subsequently, in 1978, A. Ashkin [81] proposed the utilization of lasers for atom trapping, marking the seminal introduction to the concepts of laser cooling and trapping of atoms. Initially, advancements were gradual, with significant experimental breakthroughs emerging several years later: the achievement of the first stopping of a thermal atomic beam in 1982 [82], fol-

lowed by the pioneering demonstration of three-dimensional cooling in 1985 [83], and the groundbreaking accomplishment of the first optical trapping in 1986 [84].

The foundational principle of laser cooling hinges on the conservation of energy and momentum during the absorption and emission of radiation. The prevalent technique, "Doppler cooling," exploits the velocity-dependent nature of radiation pressure induced by light due to Doppler shift. This effect dampens atomic motion when the laser frequency is adjusted below an atomic resonance [85]. This breakthrough prompted subsequent experimental inquiries and fostered a deeper theoretical comprehension. Researchers recognized the significance of the multi-level structure of actual atoms and the spatial variation of the light field's polarization in the cooling process [86–88]. These insights led to the development of new cooling mechanisms termed sub-Doppler or polarization gradient cooling, yielding temperatures on the order of 10^{-5} K. Nevertheless, a fundamental temperature constraint persists: an atom cannot attain less kinetic energy than that associated with a single photon recoil. Typically, this recoil limit corresponds to temperatures ranging between 10^{-7} and 10^{-6} K. However, researchers found ways to get around this recoil limit. They let atoms scatter photons until, by chance, the final recoil gives the atoms a velocity close to zero. These methodologies, known as sub-recoil cooling, have achieved three-dimensional temperatures below 10^{-6} K [89, 90], as evidenced by subsequent studies [91, 92]. The phenomenon of Bose-Einstein condensation

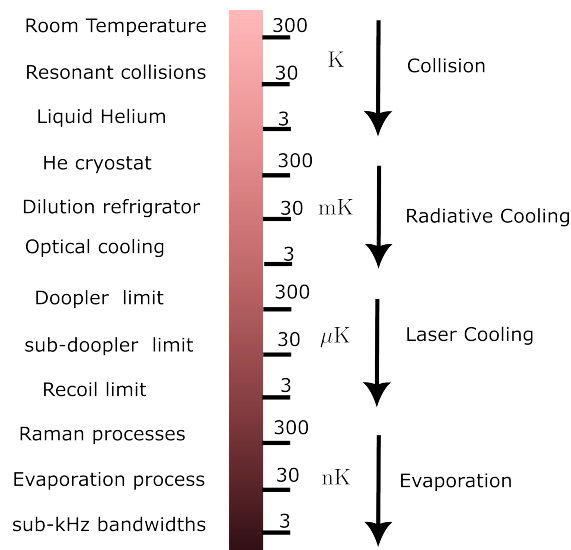


Figure 2.1: Temperature scale of cooling of atoms.

has been anticipated since 1924. This landmark discovery emerged from the collaborative efforts of Satyendra Nath Bose and Albert Einstein [93, 94]. Prompted by Bose's seminal contributions and inspired by Louis de Broglie's elucidation of particle wave nature [95], Einstein formulated a comprehensive quantum theory for bosonic particles in an ideal gas. In his two seminal papers [94], Einstein not only laid out this theory but also foresaw a remarkable phenomenon: the coherent condensation of atoms into a single quantum state. As this effect arises solely due to pure quantum statistics, the transition from classical to quantum statistics. The quantum effects become significant when the thermal de Broglie wavelength which can be written as:

$$\lambda_{dB} = \sqrt{\frac{2\pi\hbar^2}{mk_BT}} \quad (2.1)$$

When the thermal de Broglie wavelength becomes comparable to the mean inter-particle distance $n^{-1/3}$, where n represents the system's density, it highlights one of the most intriguing predictions of quantum mechanics: atoms not only exhibit discrete particle behavior but also manifest wave properties. Essentially, the de Broglie wavelength signifies the extent of positional uncertainty associated with the thermal momentum distribution, an uncertainty that escalates as the temperature T decreases. Consequently, macroscopic quantum phenomena emerge when $n^{-1/3} \sim \lambda_{dB}$, indicating that the phase space density satisfies the following criteria:

$$n\lambda_{dB}^3 = n \left(\sqrt{\frac{2\pi\hbar^2}{mk_BT}} \right)^{3/2} \geq 1 \quad (2.2)$$

Meeting this criterion results in a spatial overlap of the particle wave functions. At this juncture, particles begin to lose their distinct identities, becoming indistinguishable, and their motion can no longer be correlated with their classical trajectories. Figure 2.1 illustrates the decreasing temperature scale of atoms and the techniques used to cool them.

The Bose-Einstein condensate can be characterized by a unified wave function, effectively encapsulating the attributes of the entire macroscopic assembly as a singular coherent quantum mechanical entity. Conversely, in accordance with Pauli's exclusion

principle, such consolidation is precluded for Fermions governed by Fermi-Dirac statistics, where an anti-symmetric wave function is mandated. Regarding temperature, the aforementioned criterion for Bosons can be re-framed as [96]:

$$T \leq n^{2/3} \left(\sqrt{\frac{2\pi\hbar^2}{mk_B T}} \right) \quad (2.3)$$

This shows that quantum effects are tied to low temperatures, where wave-like behavior becomes noticeable. In everyday situations, the energetic movement of particles hides this wave behavior. At high temperatures, the thermal de Broglie wavelength gets smaller, and the gas acts according to classical physics. Here, we discuss cold and ultra-cold atoms and demonstrate how quantum effects can be utilized to conduct remarkable experiments for precision measurements.

2.2 Two-photon Transition

A two-photon transition refers to a quantum process where an atom or molecule undergoes a change in its energy state by absorbing or emitting two photons simultaneously. This phenomenon is significant in the realm of quantum mechanics and spectroscopy, offering insights into the intricate behavior of atomic and molecular systems. Unlike single-photon transitions, which are governed by strict selection rules and occur with specific frequencies corresponding to the energy difference between initial and final states, two-photon transitions involve the simultaneous absorption or emission of two photons, typically of lower energy. This process enables transitions that may not be accessible via single-photon absorption or emission, allowing for the exploration of otherwise inaccessible energy levels and providing a deeper understanding of the quantum properties of matter. Two-photon transitions find applications in various fields, including quantum optics, laser spectroscopy, and quantum information processing, where their unique characteristics contribute to the development of advanced technologies and the study of fundamental physical phenomena.

Two-photon processes are typically classified into two arrangements, illustrated in Figure 2.2. These configurations are identified as direct two-photon absorption (referred to as Ξ) and single-photon absorption combined with a single spontaneous or stimulated

emission event (referred to as Λ). The effectiveness of these transitions relies on guiding atoms from an initial ground state ($|g\rangle$) through a virtual excited state ($|i\rangle$) to reach the desired real final state ($|e\rangle$), thereby bypassing the prohibited single-photon transition. Ξ -type systems are commonly employed in two-photon absorption [97] spectroscopy.

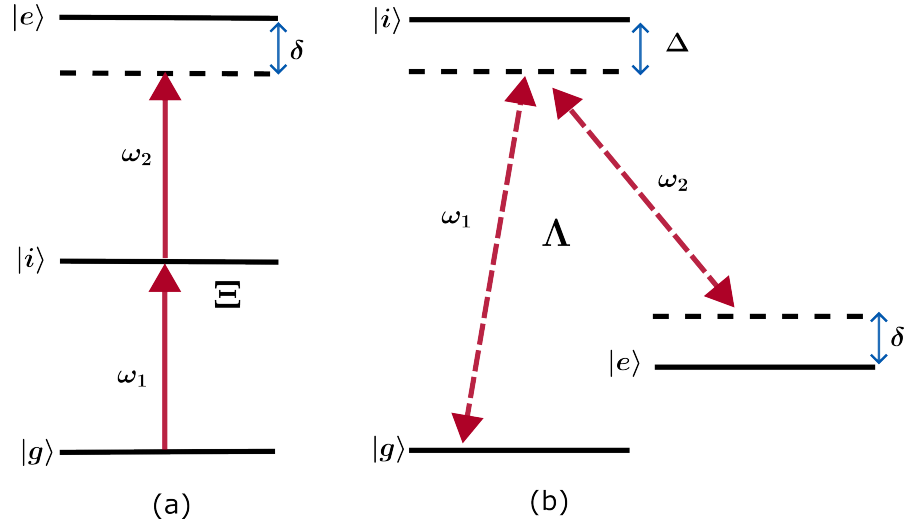


Figure 2.2: **The two-photon transition configurations can be classified as follows:** (a) Two-photon absorption (Ξ), where an initial photon, not in resonance with any atomic transition, is absorbed, leading to a virtual state, followed by a subsequent absorption event to a permissible real energy state. In this scenario, the combined energy of the photons, $\hbar(\omega_1 + \omega_2)$, must match the energy difference between the real states, denoted as $|g\rangle$. (b) Single-photon absorption coupled with a single spontaneous or stimulated emission event (Λ). Here, the disparity in photon energy, $\hbar|(\omega_1 - \omega_2)|$, must correspond to the energy separation between real states, $|e\rangle - |g\rangle$. The deviations from resonance for single and two-photon processes are indicated by Δ and δ , respectively.

The two-photon process pertinent to this apparatus involves Λ orientation, encompassing the well-known phenomena of Raman and Bragg diffraction of atoms [98]. The primary distinction lies in the fact that in Raman diffraction, the internal state undergoes alteration during the two-photon process, whereas in Bragg diffraction, it remains unchanged. Consequently, the two frequencies, ω_1 and ω_2 , responsible for generating the diffraction gratings, must be adjusted to initiate the process. Hence, their difference, $\hbar|(\omega_1 - \omega_2)|$, is contingent on the mechanism employed. In a typical Raman scattering scenario, an atomic sample is illuminated by a monochromatic light source that is detuned from all electronic resonances. The atoms can simultaneously absorb an

incoming photon and emit a photon of a different frequency. This process coherently transfers the atom to an energy level equivalent to the energy difference between the two photons. The absorption and decay event gives rise to the conventional Λ -level scheme depicted in Figure 2.2. The manipulation of the atomic ensemble in this setup employs two closely related transition schemes, with the exception that the decay process is stimulated toward a desired state.

2.2.1 Light atom diffraction theory

A general description of the interaction of a light field with an atom that can be configured in a variety of different energy states is extremely complex. As we use the alkali metal rubidium in our experiment, we will limit this treatment to atoms with a single valence electron. As a first step, we will simplify the problem to a two-level atom, later expanding for the three-level Raman and Bragg transition employed in the atom interferometer.

Light atom interaction of two-level system:

The behavior of stimulated Λ transitions becomes apparent when examining the time-dependent changes of a two-level atom subjected to an oscillating electric field. Consider a discrete two-level atom interacting with electromagnetic radiation of frequency ω_L and arbitrary phase ϕ , treated as a classical field (utilizing a semi-classical approach). Under the dipole approximation, the Hamiltonian governing an atom in such an oscillating electric field is expressed as:

$$\hat{H}_{total} = \hat{H}_{atom} + \hat{H}_{int} \quad (2.4)$$

where \hat{H}_{atom} is the atomic Hamiltonian with eigenenergies, while \hat{H}_{int} is the interaction Hamiltonian of the atom with the light field.

$$\hat{H}_{atom} = \hbar\omega_e|e\rangle\langle e| + \hbar\omega_g|g\rangle\langle g| \quad (2.5)$$

$$\hat{H}_{int} = -\vec{d} \cdot \vec{E} \quad (2.6)$$

Here, $\vec{d} = -q\vec{r}$ (electric dipole moment) and $\vec{E} = \vec{E}_0 \cos(\omega_L t + \phi)$ (oscillating

electromagnetic field).

Typically, the wavelength of light far exceeds the size of an atom, denoted as $\lambda \gg a_0$. Under the assumption that the atom's position, approximately R , remains constant throughout the interaction duration, changes in phase are minor, and the electric field's amplitude remains same across the atom's size. Consequently, the electric dipole approximation simplifies by disregarding spatial variation of the electric field, such that $E(\sim r, t) \approx E(\sim R, t) \approx E(t)$. The total Hamiltonian of the system can now be written as:

$$\hat{H}_{total} = \hbar\omega_e|e\rangle\langle e| + \hbar\omega_g|g\rangle\langle g| - \vec{d} \cdot \vec{E}_0 \cos(\omega_L t + \phi) \quad (2.7)$$

The temporal evolution of the two level system can be described by a time-dependent Schrödinger equation with the following ansatz for the wave function

$$i\hbar \frac{d}{dt} |\Psi(t)\rangle = \hat{H}_{total} |\Psi(t)\rangle = (\hat{H}_{atom} + \hat{H}_{int}) |\Psi(t)\rangle \quad (2.8)$$

The time-dependent wavefunction $\Psi(t)$ for a two-level system is given by Equation 2.9, where $|g\rangle$ and $|e\rangle$ denote the ground and excited states, respectively. $E_g = \hbar\omega_g$ and $E_e = \hbar\omega_e$ represent the energies of these states, while c_g and c_e are normalization factors ensuring $\langle \Psi(t) | \Psi(t) \rangle = c_g^2 + c_e^2 = 1$.

$$|\Psi(t)\rangle = c_e |e\rangle e^{-iE_e t/\hbar} + c_g |g\rangle e^{-iE_g t/\hbar} \quad (2.9)$$

Given the driving field's frequency ω_L and $\omega_e - \omega_g = \omega_{eg}$ as depicted in Figure 2.2 (b). Equation 2.7, 2.8, and 2.9 establish a set of coupled equations governing the coefficients c_e and c_g [99]. These coupled equations can be written by solving Equation 2.8 and 2.9 as:

$$\begin{aligned} i\hbar \frac{d}{dt} a_e(t) &= \hbar\omega_e a_e(t) + \hbar\Omega_{eg} \left(\frac{e^{i(\omega_L t + \phi)} + e^{-i(\omega_L t + \phi)}}{2} \right) a_g(t) \\ i\hbar \frac{d}{dt} a_g(t) &= \hbar\Omega_{eg}^* \left(\frac{e^{-i(\omega_L t + \phi)} + e^{i(\omega_L t + \phi)}}{2} \right) a_e(t) + \hbar\omega_g a_g(t) \end{aligned} \quad (2.10)$$

where, $a_e(t) = c_e e^{-iE_e t/\hbar}$ and $a_g(t) = c_g e^{-iE_g t/\hbar}$. Here we introduce the Rabi

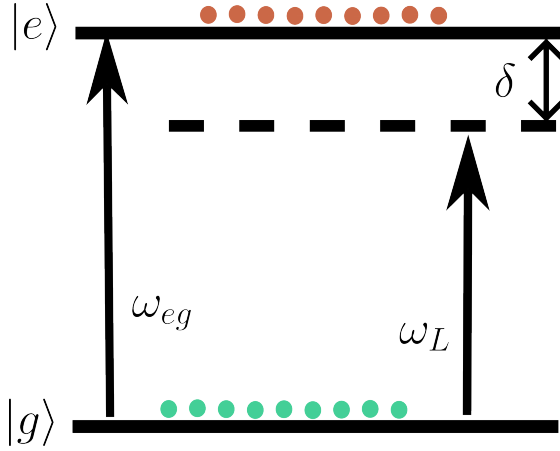


Figure 2.3: **Schematic of a discrete two-level system under the presence of a non-resonant light field.** This scheme involves the absorption of a single photon followed by either a spontaneous or a stimulated emission event. For this to occur, the energy difference of the absorbed photon, $\hbar|\omega_{eg} - \omega_L|$, must match the energy difference between the two real states, $|e\rangle$ and $|g\rangle$. The detuning of the single photon is represented by δ .

frequency on resonance Ω_{eg} and out of resonance Ω_r by detuning $\delta = \omega_L - \omega_{eg} = \omega_L - (\omega_e - \omega_g)$ as:

$$\begin{aligned}\Omega_{eg} &= -\frac{\langle e|\vec{d} \cdot \vec{E}_0|g\rangle}{\hbar} \\ \Omega_r &= \sqrt{\delta^2 + \Omega_{eg}^2}\end{aligned}\tag{2.11}$$

Given that $\Omega_{eg} \ll \omega_e, \omega_g$, we ignore the rapidly oscillating terms with frequencies ω_e, ω_g , focusing solely on the slowly oscillating coefficients $a_e(t)$ and $c_g(t)$. Upon further solving Equation 2.10, which encompasses both off-resonant terms $\omega_{eg} + \omega_L$ and resonant terms $\omega_{eg} - \omega_L = -\delta$, and assuming a small detuning compared to the transition frequency $\delta \ll \omega_{eg}$, we can consider the two level dynamics to neglect the fast oscillating terms based on rotating wave approximation (RWA). Consequently, considering only the resonant term, the Schrödinger equation simplifies to:

$$\begin{aligned}i\frac{d}{dt}c_e &= \frac{\Omega_{eg}}{2} \{e^{-i(\delta t + \phi)}\} c_g \\ i\frac{d}{dt}c_g &= \frac{\Omega_{eg}^*}{2} \{e^{i(\delta t + \phi)}\} c_e\end{aligned}\tag{2.12}$$

This finally results in an expression with the coefficients c_e and c_g and a time-dependent

Hamiltonian can be written as:

$$\frac{d}{dt} \begin{pmatrix} c_e \\ c_g \end{pmatrix} = \frac{-i}{2} \begin{pmatrix} 0 & \Omega_{eg} \{e^{-i(\delta t + \phi)}\} \\ \Omega_{eg}^* \{e^{i(\delta t + \phi)}\} & 0 \end{pmatrix} \begin{pmatrix} c_e \\ c_g \end{pmatrix} \quad (2.13)$$

Thus, the updated approximate Hamiltonian can now be expressed in the basis of $|e\rangle$ and $|g\rangle$ as follows:

$$\hat{H}_{total} = \frac{\hbar}{2} \begin{pmatrix} 0 & \Omega_{eg} \{e^{-i(\delta t + \phi)}\} \\ \Omega_{eg}^* \{e^{i(\delta t + \phi)}\} & 0 \end{pmatrix} \quad (2.14)$$

We transform this Hamiltonian, which exhibits weak time-dependence, into a time-independent form by employing a suitable unitary function. Through a general unitary transformation, the resultant transformed Hamiltonian takes the form $\hat{H}'_{total} = U \hat{H}_{total} U^\dagger + i\hbar \frac{\partial U}{\partial t} U^\dagger$ [100]. Here the unitary operator is written as:

$$U = e^{i\delta t/2} |e\rangle\langle g| + e^{-i\delta t/2} |g\rangle\langle e| \quad (2.15)$$

In this updated framework, the new Hamiltonian becomes:

$$\hat{H}'_{total} = \frac{\hbar}{2} \begin{pmatrix} -\delta & \Omega_{eg} e^{-i\phi} \\ \Omega_{eg}^* e^{i\phi} & \delta \end{pmatrix} \quad (2.16)$$

The eigenvalues of the scaled Hamiltonian is given as:

$$\lambda_{\pm} = \pm \frac{\hbar \Omega_r}{2} \quad (2.17)$$

The eigenenergies of the scaled Hamiltonian is given as:

$$\begin{aligned} \Delta E_e &= \frac{\hbar}{2} (-\delta + \Omega_r) \\ \Delta E_g &= \frac{\hbar}{2} (\delta - \Omega_r) \end{aligned} \quad (2.18)$$

The alteration in energy experienced by the eigenstates of a time-independent Hamiltonian when influenced by a light field is termed the AC Stark shift which give rise to new eigenstates called as dressed states. For far detuned light i.e. $\delta \gg \Omega_{eg}$, the sym-

metric energy adjustment observed in the so-called dressed states can be expanded in expressions involving:

$$\Delta E_g = -\Delta E_e = \frac{\hbar}{2}(\delta - \Omega_r) = \frac{\hbar}{2} \left(\delta - \sqrt{\delta^2 + \Omega_{eg}^2} \right) \approx -\frac{\hbar \Omega_{eg}^2}{4\delta} \quad (2.19)$$

Now, we apply a pulse of light of length τ and find the coefficients of $c_e(t_0 + \tau)$ and $c_g(t_0 + \tau)$. This is done by transforming initial wavefunction $|\Psi(t_0)\rangle$ into the rotating frame and projecting it to the eigenstates of \hat{H}'_{total} . We thus calculate $|\Psi(t_0 + \tau)\rangle'$ and do a back transformation to obtain $|\Psi(t_0 + \tau)\rangle$. Thus one can write the coefficients as [100]:

$$c_e(t_0 + \tau) = e^{-i\frac{\delta\tau}{2}} \left\{ c_e(t_0) \left[\cos\left(\frac{\Omega_r\tau}{2}\right) + \frac{i\delta}{\Omega_r} \sin\left(\frac{\Omega_r\tau}{2}\right) \right] + c_g(t_0) e^{-i(\delta t_0 + \phi)} \left[\frac{-i\Omega_{eg}}{\Omega_r} \sin\left(\frac{\Omega_r\tau}{2}\right) \right] \right\} \quad (2.20)$$

$$c_g(t_0 + \tau) = e^{i\frac{\delta\tau}{2}} \left\{ c_e(t_0) e^{i(\delta t_0 + \phi)} \left[\frac{-i\Omega_{eg}}{\Omega_r} \sin\left(\frac{\Omega_r\tau}{2}\right) \right] + c_g(t_0) \left[\cos\left(\frac{\Omega_r\tau}{2}\right) - \frac{i\delta}{\Omega_r} \sin\left(\frac{\Omega_r\tau}{2}\right) \right] \right\} \quad (2.21)$$

Formulas 2.20 and 2.21 provide the updated probability amplitudes of the two stable atomic states after a time duration τ under the condition of constant amplitude electromagnetic coupling. When the applied field is absent, represented by $\Omega_{eg} = 0$ and $\Omega_r = |\delta|$, these equations simplify to:

$$c_e(t_0 + \tau) = c_e(t_0) e^{-i\frac{\delta\tau}{2}} [\cos(|\delta|\tau/2) + i(\delta/|\delta|)\sin(|\delta|\tau/2)] = c_e(t_0) \quad (2.22)$$

$$c_g(t_0 + \tau) = c_g(t_0) e^{i\frac{\delta\tau}{2}} [\cos(|\delta|\tau/2) - i(\delta/|\delta|)\sin(|\delta|\tau/2)] = c_g(t_0) \quad (2.23)$$

In case of zero detuning i.e. $\delta = 0$, $\Omega_r = \Omega_{eg}$, the equations 2.20 and 2.21 becomes:

$$\begin{aligned} c_e(t_0 + \tau) &= c_e(t_0) \cos(\Omega_{eg}\tau/2) - i c_g(t_0) e^{-i\phi} \sin(\Omega_{eg}\tau/2) \\ c_g(t_0 + \tau) &= -i c_e(t_0) e^{i\phi} \sin(\Omega_{eg}\tau/2) + c_g(t_0) \cos(\Omega_{eg}\tau/2) \end{aligned} \quad (2.24)$$

We can initiate a two-level system wherein all atoms are initially in one state (for instance, $c_e(t_0) = 0, c_g(t_0) = 1$), and then ascertain the likelihood of locating an atom in either state $|e\rangle$ or $|g\rangle$.

$$P_e(\tau) = |c_e(\tau)|^2 = \left(\frac{\Omega_{eg}}{\Omega_r}\right)^2 \sin^2\left(\frac{\Omega_{eg}\tau}{2}\right) = \left(\frac{\Omega_{eg}^2}{2\Omega_r^2}\right) [1 - \cos(\Omega_{eg}\tau)] \quad (2.25)$$

$$P_g(\tau) = |c_g(\tau)|^2 = \left(\frac{\Omega_{eg}}{\Omega_r}\right)^2 \cos^2\left(\frac{\Omega_{eg}\tau}{2}\right) = \left(\frac{\Omega_{eg}^2}{2\Omega_r^2}\right) [1 + \cos(\Omega_{eg}\tau)] \quad (2.26)$$

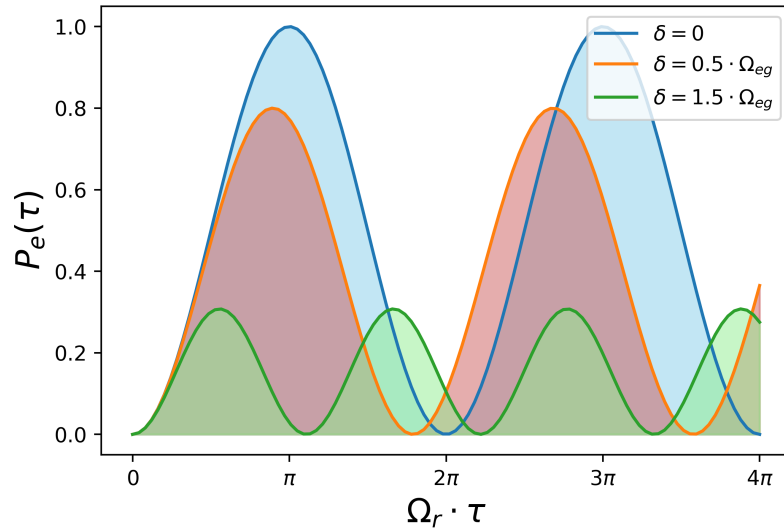


Figure 2.4: Population probability $P_e(\tau)$ of excited state $|e\rangle$ from figure 2.3 for different detuning values.

The oscillations displayed in Figure 2.3 illustrate Rabi oscillations under varying detuning conditions. When $\delta = 0$, the transition probability reaches a maximum amplitude, fluctuating between 0 and 1. Conversely, for $\delta \neq 0$, the transition probability diminishes, and the oscillation frequency consistently exceeds the resonant frequency. Consequently, based on Figure 2.3, specific pulse durations can be identified. At $\delta = 0$, the duration corresponds to complete population inversion is termed a π pulse, denoted as $\Omega_{eg} \cdot \tau = \pi$. Conversely, when atoms are equally distributed between both states, it signifies a $\pi/2$ pulse, represented as $\Omega_{eg} \cdot \tau = \pi/2$. In case of on-resonant light i.e.

$\delta = 0$ the above equation becomes:

$$\begin{aligned} P_e(\tau) &= \frac{1}{2}[1 - \cos(\Omega_{eg}\tau)] \\ P_g(\tau) &= \frac{1}{2}[1 + \cos(\Omega_{eg}\tau)] \end{aligned} \quad (2.27)$$

Atoms in momentum state:

Now, if we contemplate the atoms possessing a specific momentum \vec{p} , we can write the atomic wave-function as a propagating plane wave:

$$|\Psi(\vec{r}, t)\rangle = ae^{-i\vec{p}\cdot\vec{r}/\hbar}|\Psi(t)\rangle \quad (2.28)$$

where a is the amplitude factor. The new Hamiltonian is modified with the momentum term as:

$$\hat{H}_{total} = \hat{H}_{mom} + \hat{H}_{atom} + \hat{H}_{int} \quad (2.29)$$

$$\hat{H}_{total} = \frac{\vec{p}^2}{2m} + \hbar\omega_e|e\rangle\langle e| + \hbar\omega_g|g\rangle\langle g| - \vec{d} \cdot \vec{E}_0 \cos(\omega_L t + \phi) \quad (2.30)$$

The electric field includes the spatial variation $\vec{E} = \vec{E}_0 \cos(\vec{k} \cdot \vec{r} - \omega_L t + \phi)$ in the interaction term. The interaction term involving light can be adjusted by employing the closure relation:

$$1 \cdot e^{\pm i\vec{k}\cdot\vec{r}} = \int d^3p e^{\pm i\vec{k}\cdot\vec{r}} |\mathbf{p}\rangle\langle \mathbf{p}| = \int d^3p |\mathbf{p} \pm \hbar\vec{k}\rangle\langle \mathbf{p}| \quad (2.31)$$

Consequently, when a photon is absorbed or emitted, the atom's total momentum undergoes a change of $\hbar\vec{k}$. Consequently, the two atomic states within our system become coupled, and the two potential eigenstates are now $|g, \vec{p}\rangle$ and $|e, \vec{p} + \hbar\vec{k}\rangle$. Given the introduction of a new set of eigenstates, the behavior of the system, inclusive of external degrees of freedom, is described by the wave function [100]:

$$|\Psi(t)\rangle = c_e(t)e^{-i(\frac{\omega_e}{2} + \frac{|\vec{p} + \hbar\vec{k}|^2}{2m\hbar})t} |e, \vec{p} + \hbar\vec{k}\rangle + c_g(t)e^{-i(\frac{\omega_g}{2} + \frac{|\vec{p}|^2}{2m\hbar})t} |g, \vec{p}\rangle \quad (2.32)$$

The energy eigenvalues of the system are currently:

$$\begin{aligned} E|e, \vec{p} + \hbar\vec{k}\rangle &= \hbar\omega_e + \frac{|\vec{p} + \hbar\vec{k}|^2}{2m} = \hbar\bar{\omega}_e \\ E|g, \vec{p}\rangle &= \hbar\omega_g + \frac{|\vec{p}|^2}{2m} = \hbar\bar{\omega}_g \end{aligned} \quad (2.33)$$

In this updated framework, the calculation of the non-resonant Rabi frequency necessitates consideration of both the Doppler shift $\frac{\vec{p}\cdot\vec{k}}{m}$ and the photon recoil $\frac{\hbar|\vec{k}|^2}{2m}$. This results in a new effective detuning, which is now determined as:

$$\delta_{eff} = \omega_L - \left(\frac{E|e, \vec{p} + \hbar\vec{k}\rangle - E|g, \vec{p}\rangle}{\hbar} \right) = \omega_L - \omega_{eg} + \frac{\vec{p} \cdot \vec{k}}{m} + \frac{\hbar|\vec{k}|^2}{2m} \quad (2.34)$$

Expanding to a three-level system: Raman and Bragg Diffraction

In the preceding section, we focused on the dynamics of a two-level system, which will now be expanded to include a three-level system. We introduce an atom with two ground states $|g\rangle$ and $|e\rangle$, along with an intermediate excited level $|i\rangle$, interacting with two lasers as shown in Figure 2.2.

The new driving electric fields now consists of two frequency components:

$$\begin{aligned} \vec{E}_1 &= \vec{E}_{1,0} \cos(\vec{k}_1 \cdot \vec{r} - \omega_1 t + \phi_1) \\ \vec{E}_2 &= \vec{E}_{2,0} \cos(\vec{k}_2 \cdot \vec{r} - \omega_2 t + \phi_2) \end{aligned} \quad (2.35)$$

The Hamiltonian for the three level system can be written as:

$$\hat{H}_{total} = \frac{\vec{p}^2}{2m} + \hbar\omega_e |e\rangle\langle e| + \hbar\omega_g |g\rangle\langle g| + \hbar\omega_i |i\rangle\langle i| - \vec{d} \cdot (\vec{E}_0 + \vec{E}_2) \quad (2.36)$$

In the three-level system, akin to the preceding section, the external degrees of freedom exhibit a close connection with the internal ones. This is because the atom's state can only undergo changes through the absorption or stimulated emission of laser photons. When the atom is in state $|g, \vec{p}\rangle$, it can be excited to state $|i\rangle$ by either laser 1 or laser 2, leading to the following potential states: $|i, \vec{p} + \hbar\vec{k}_1\rangle$ and $|i, \vec{p} + \hbar\vec{k}_2\rangle$. Through stimulated emission, the atom eventually transitions to state $|e, \vec{p} + \hbar(\vec{k}_1 - \vec{k}_2)\rangle$.

$=|e, \vec{p} + \hbar(\vec{k}_{eff})\rangle$. This is signified by all five possibilities forming a closed-momentum family, where the quantum state of a single atom can be depicted by the following wave function:

$$|\Psi(t)\rangle = a_g(t)|g, \vec{p}_g\rangle + a_e(t)|e, \vec{p}_e\rangle + a_{i1}(t)|i, \vec{p}_{i1}\rangle + a_{i2}(t)|i, \vec{p}_{i2}\rangle + a_{i3}(t)|i, \vec{p}_{i3}\rangle \quad (2.37)$$

with time-dependent coefficients $a_n(t)$ and the momenta:

$$\begin{aligned} \vec{p}_g &= \vec{p} \\ \vec{p}_e &= \vec{p} + \hbar\vec{k}_{eff} \\ \vec{p}_{i1} &= \vec{p} + \hbar\vec{k}_1 \\ \vec{p}_{i2} &= \vec{p} + \hbar\vec{k}_2 \\ \vec{p}_{i3} &= \vec{p} + \hbar(\vec{k}_{eff} + \vec{k}_1) \end{aligned} \quad (2.38)$$

The energies of these states are influenced by the Doppler effect and the recoil energy.

$$\begin{aligned} E_{|e, \vec{p} + \hbar\vec{k}_1 - \hbar\vec{k}_2\rangle} &= \hbar\omega_e + \frac{(\vec{p} + \hbar(\vec{k}_1 - \vec{k}_2))^2}{2m} \equiv \hbar\bar{\omega}_e \\ E_{|g, \vec{p}\rangle} &= \hbar\omega_g + \frac{|\vec{p}|^2}{2m} \equiv \hbar\bar{\omega}_g \end{aligned} \quad (2.39)$$

and the detunings for this system is defined as :

$$\Delta_{eff} = \omega_1 - \left(\omega_i - \omega_g + \frac{|\vec{p}|^2 - |\vec{p} + \hbar\vec{k}|^2}{2m\hbar} \right) = \omega_1 - \left(\omega_i - \omega_g + \frac{\vec{p} \cdot \vec{k}_1}{m} + \frac{\hbar\vec{k}_1^2}{2m} \right) \quad (2.40)$$

$$\delta_{eff} = (\omega_1 - \omega_2) - (\bar{\omega}_e - \bar{\omega}_g) = \omega_{eff} - \left(\omega_{eg} + \frac{\vec{p} \cdot \vec{k}_{eff}}{m} + \frac{\hbar\vec{k}_{eff}^2}{2m} \right) \quad (2.41)$$

The defined effective frequency, wave vector, and offset phase of both lasers as follows:

$$\Phi_1 - \Phi_2 = (\vec{k}_1 - \vec{k}_2) \cdot \vec{r} - (\omega_1 - \omega_2)t + (\phi_1 - \phi_2) \quad (2.42)$$

Solving the Schrödinger equation $i\hbar \frac{\partial}{\partial t} |\Psi(t)\rangle = \hat{H}_{total} |\Psi(t)\rangle$ now gives in terms of the new coefficients and the appropriate closure relations as Equation 2.31 into

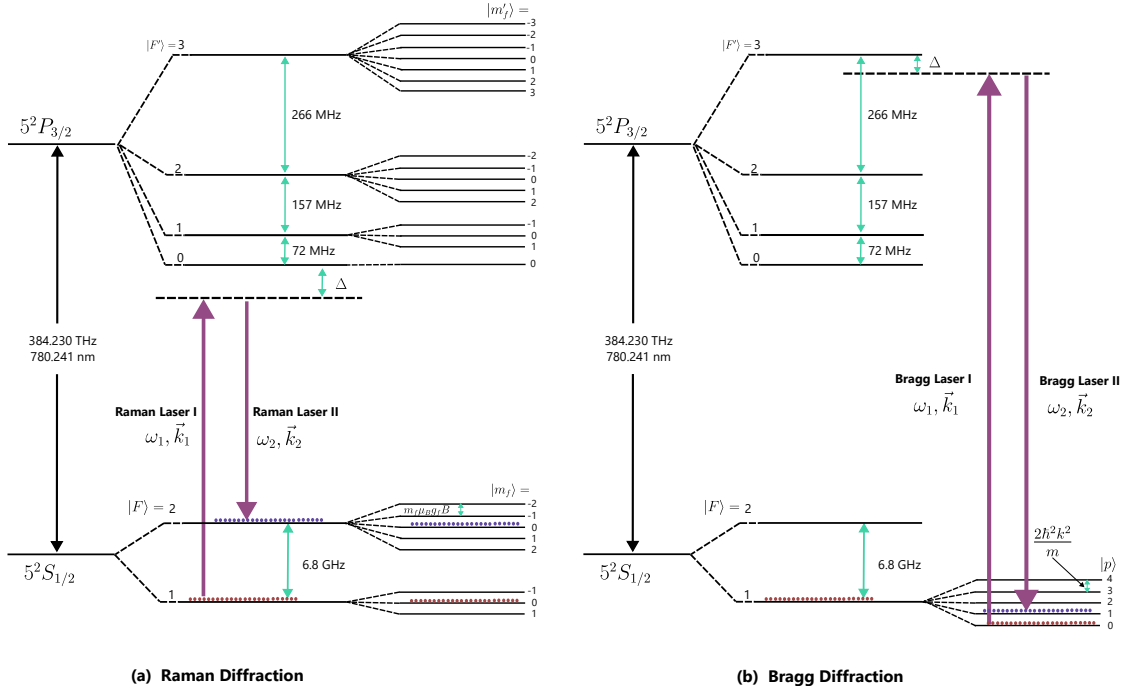


Figure 2.5: ^{87}Rb D2 Structure for Raman and Bragg Transitions (a) Co-propagating Raman beams induce transitions between the states $|F = 1, m_F = 0\rangle$ and $|F = 2, m_F = 0\rangle$. (b) Counter-propagating Bragg beams drive transitions between momentum states, where the energy separation corresponds to the two-photon recoil energy.

gives:

$$\begin{aligned}
 i\dot{c}_g(t) &= \frac{c_{i1}(t)}{2}\Omega_{g1}^*e^{i\Delta t}e^{-i\phi_1} + \frac{c_{i2}(t)}{2}\Omega_{g2}^*e^{i(\Delta-\delta-\omega_{eg}+\frac{\delta}{2})t}e^{-i\phi_2} \\
 i\dot{c}_e(t) &= \frac{c_{i3}(t)}{2}\Omega_{e1}^*e^{i(\Delta+\omega_{eg}-\delta_3)t}e^{-i\phi_1} + \frac{c_{i1}(t)}{2}\Omega_{e2}^*e^{i(\Delta-\delta)t}e^{-i\phi_2} \\
 i\dot{c}_{i1}(t) &= \frac{c_g(t)}{2}\Omega_{g1}e^{-i\Delta t}e^{i\phi_1} + \frac{c_e(t)}{2}\Omega_{e2}e^{-i(\Delta-\delta)t}e^{i\phi_2} \\
 i\dot{c}_{i2}(t) &= \frac{c_g(t)}{2}\Omega_{g2}e^{-i(\Delta-\delta-\omega_{eg}+\frac{\delta}{2})t}e^{i\phi_2} \\
 i\dot{c}_{i3}(t) &= \frac{c_e(t)}{2}\Omega_{e1}e^{-i(\Delta+\omega_{eg}-\delta_3)t}e^{i\phi_1}
 \end{aligned} \tag{2.43}$$

where $\delta_2 = \frac{\hbar\vec{k}_2 \cdot \vec{k}_{eff}}{m}$, $\delta_3 = \frac{\hbar\vec{k}_3 \cdot \vec{k}_{eff}}{m}$ and $\Omega_{xy} = -\frac{\langle x|\vec{d} \cdot \vec{E}|y\rangle}{\hbar}$ which is the coupling strength between two states is described as the Rabi frequency

Hence, the equation system described in Equations 2.43 can be streamlined to a two-

level equation system through the process of adiabatic elimination of the intermediate states [101]. Consequently, a new and simplified Hamiltonian can be defined within the two-level system framework, achieved by removing all coefficients associated with the intermediate stage in the basis of $|g, \vec{p}\rangle$ and $|e, \vec{p} + \hbar\vec{k}_{eff}\rangle$.

$$\hat{H}_{reduced} = \hbar \begin{pmatrix} \Omega_e^{AC} & \frac{\Omega_{eff}}{2} e^{-i(\delta_{eff}t + \phi_{eff})} \\ \frac{\Omega_{eff}}{2} e^{i(\delta_{eff}t + \phi_{eff})} & \Omega_g^{AC} \end{pmatrix} \quad (2.44)$$

Thus the co-efficient $c_e(t)$ and $c_g(t)$ can be expressed as:

$$\begin{aligned} \dot{c}_e(t) &= -i\Omega_e^{AC} c_e(t) - i\frac{\Omega_{eff}}{2} e^{-i(\delta_{eff}t + \phi_{eff})} c_g(t) \\ \dot{c}_g(t) &= -i\Omega_g^{AC} c_g(t) - i\frac{\Omega_{eff}}{2} e^{i(\delta_{eff}t + \phi_{eff})} c_e(t) \end{aligned} \quad (2.45)$$

where, the above equations are provided with descriptions of the effective Rabi frequency Ω_{eff} , the effective phase disparity between the two light fields, and the light-induced shifts of the hyperfine levels. Thus,

$$\begin{aligned} \Omega_{eff} &\equiv \frac{\Omega_e^* \Omega_g}{2\Delta} \\ \phi_{eff} &\equiv \phi_2 - \phi_1 \\ \Omega_g^{AC} &\equiv \frac{|\Omega_{g1}|^2}{4\Delta} + \frac{|\Omega_{g2}|^2}{4(\Delta - \omega_{eg})}, \quad \Omega_e^{AC} \equiv \frac{|\Omega_{e1}|^2}{4(\Delta + \omega_{eg})} + \frac{|\Omega_{e2}|^2}{4\Delta} \end{aligned} \quad (2.46)$$

The equation 2.45 is further solved to find the coefficients with time in the rotating frame.

$$\begin{aligned} c_g(t_0 + \tau) &= e^{-i(\Omega_{AC} - \delta_{eff})\tau/2} \left[\left(\cos \frac{\Omega_r \tau}{2} - i \frac{(\delta_{AC} - \delta_{eff})}{\Omega_r} \sin \frac{\Omega_r \tau}{2} \right) c_g(t_0) \right. \\ &\quad \left. - i \frac{\Omega_{eff}}{\Omega_r} \sin \frac{\Omega_r \tau}{2} e^{i(\delta_{eff}t_0 + \phi_{eff})} c_e(t_0) \right] \end{aligned} \quad (2.47)$$

$$c_e(t_0 + \tau) = e^{-i(\Omega_{AC} + \delta_{eff})\tau/2} \left[\left(\cos \frac{\Omega_r \tau}{2} + i \frac{(\delta_{AC} - \delta_{eff})}{\Omega_r} \sin \frac{\Omega_r \tau}{2} \right) c_e(t_0) - i \frac{\Omega_{eff}}{\Omega_r} \sin \frac{\Omega_r \tau}{2} e^{-i(\delta_{eff} t_0 + \phi_{eff})} c_g(t_0) \right] \quad (2.48)$$

δ_{AC} represents the differential AC Stark shift, while Ω_{AC} signifies the cumulative AC-Stark shifts and Ω_r is the Rabi frequency in the rotating frame

$$\begin{aligned} \delta_{AC} &\equiv \Omega_e^{AC} - \Omega_g^{AC} \\ \Omega_{AC} &\equiv \Omega_e^{AC} + \Omega_g^{AC} \\ \Omega_r &\equiv \sqrt{\Omega_{eff}^2 + (\delta_{eff} - \delta_{AC})^2}. \end{aligned} \quad (2.49)$$

Thus, from the resulting coefficients obtained in rotation wave approximation in Equation 2.47 and 2.48 can be used to find the populations of both states. For the starting parameters $c_g(t = 0) = 1$ and $c_e(t = 0) = 0$, the populations of both states can be expressed as:

$$\begin{aligned} P_g(t) &= \frac{\Omega_{eff}^2}{\Omega_{eff}^2 + (\delta_{eff} - \delta_{AC})^2} \cos^2 \left(\sqrt{\Omega_{eff}^2 + (\delta_{eff} - \delta_{AC})^2} \cdot \frac{\tau}{2} \right) \\ P_e(t) &= \frac{\delta_{eff}^2}{\Omega_{eff}^2 + (\delta_{eff} - \delta_{AC})^2} \sin^2 \left(\sqrt{\Omega_{eff}^2 + (\delta_{eff} - \delta_{AC})^2} \cdot \frac{\tau}{2} \right). \end{aligned} \quad (2.50)$$

Rabi oscillations induced by two-photon Raman transitions exhibit a frequency denoted as Ω_{eff} . For instance, during a π -pulse, the entire population ideally transfers from one momentum state to another. In Bragg diffraction, the ratio $\omega_{eff}/\delta_{eff}$ is approximately 0.01 ppb, facilitating the approximation of the effective Rabi frequency as follows:

$$\Omega_{eff} \equiv \frac{\Omega_e^* \Omega_g}{2\Delta} \approx \frac{\Omega^2}{2\Delta}, \quad (2.51)$$

with $\Omega_e^* = \Omega_g \equiv \Omega$ as the single photon Rabi frequency. In the case of a resonant interaction ($\delta_{eff} = 0$) and $\delta_{AC} = 0$. Thus Equation 2.50 simplifies to the following expressions:

$$P_g(t) = \cos^2 \left[\frac{\Omega_{\text{eff}} \cdot \tau}{2} \right] = \frac{1}{2} [1 + \cos(\Omega_{\text{eff}} \cdot \tau)], \quad (2.52)$$

$$P_e(t) = \sin^2 \left[\frac{\Omega_{\text{eff}} \cdot \tau}{2} \right] = \frac{1}{2} [1 - \cos(\Omega_{\text{eff}} \cdot \tau)]. \quad (2.53)$$

The effectiveness of the Rabi frequency scales with the total intensity of laser light i.e. I_{1+2} when the relative intensity $q = \frac{I_2}{I_1}$ is constant, offering a means to adjust the transition probability [77].

$$\Omega_{\text{eff}} = \frac{\Omega_e^* \Omega_g}{2\Delta} \propto \sqrt{I_1 I_2} = \sqrt{\frac{q}{1+q}} \cdot I_{1+2} \quad (2.54)$$

Deducing from equations 2.47 and 2.48, table no 2.1 give the phase of the atomic wave from transitions between two specific states.

Transition	Phase shift
$ g, \vec{p}\rangle \rightarrow g, \vec{p}\rangle$	$-(\Omega_{AC} - \delta_{eff})\tau/2 - \theta_0$
$ g, \vec{p}\rangle \rightarrow e, \vec{p} + \hbar\vec{k}_{eff}\rangle$	$-(\Omega_{AC} - \delta_{eff})\tau/2 - \frac{\pi}{2} - \delta_{eff}t_0 - \phi_{eff}$
$ g, \vec{p} + \hbar\vec{k}_{eff}\rangle \rightarrow g, \vec{p} + \hbar\vec{k}_{eff}\rangle$	$-(\Omega_{AC} - \delta_{eff})\tau/2 + \theta_0$
$ g, \vec{p} + \hbar\vec{k}_{eff}\rangle \rightarrow e, \vec{p}\rangle$	$-(\Omega_{AC} - \delta_{eff})\tau/2 - \frac{\pi}{2} + \delta_{eff}t_0 + \phi_{eff}$

Table 2.1: Phase shifts for different transitions

$$\text{where, } \theta_0 = \cos\left(\frac{\Omega_{RT}}{2}\right) + \frac{i(\delta_{eff} - \Delta_{AC})}{\Omega_R} \sin\left(\frac{\Omega_{RT}}{2}\right)$$

2.2.2 Summary

In this chapter, an overview about the basic interactions of light and matter was given which led to the description of Raman and Bragg diffraction as a coherent two-photon process between two momentum states. These transitions have been used to form beam splitters and combiners for the matter waves for our experiment.

Chapter 3

Experimental apparatus and methods

This section provides an in-brief description of the experimental configuration employed to generate ultracold atoms and achieve Bose-Einstein Condensation (BEC) for the investigations documented in this thesis. A significant component of the experimental apparatus draws inspiration from the setup utilized in the research conducted by Sunil Kumar [6] and Sumit Sarkar [102], albeit with certain modifications tailored specifically for the creation of ultra-cold atoms through optical dipole trapping techniques and development of Bragg lattice for Atom Interferometer.

3.1 The vacuum assembly

To ensure efficient cooling throughout all stages of the cooling process, it's essential to minimize the atoms interaction within the surrounding 300K environment. There are three primary mechanisms of thermal energy transfer need to be addressed to single out and isolate the atoms effectively: radiative, mechanical, and convective heating mechanism. Radiative heating poses significant challenges, particularly when dealing with big objects like those found in cryogenic buffer gas systems, necessitating thorough radiation shielding measures. However, the laser-cooled atomic samples utilized in this setup exhibit minimal photon absorption cross-sections and relatively limited atomic transitions, significantly reducing the impact of black-body radiation. To mitigate or minimize heating effects from mechanical and convective processes to acceptable levels, the atomic sample is placed inside an ultra-high vacuum (UHV) chamber and shielded

from the external environment.

3.1.1 Modes of Gas Flow

As a system transitions from atmospheric pressure condition to high vacuum through pumping, the gas within undergoes distinct stages of gas flow. In vacuum technology, three primary types of flow are typically observed: viscous or continuum flow, molecular flow, and the transitional state between these known as Knudsen flow. One can distinguish the viscous state at high pressures from the molecular state at low pressures and the transitional state between these two. Fluid flow is described by two unitless numbers, the Reynolds number and the Knudsen Number.

	Pressure				
	10 ³ mbar	10 ⁰ mbar	10 ⁻³ mbar	10 ⁻⁶ mbar	10 ⁻⁹ mbar
Particle Density, n (cm ⁻³)	10 ¹⁹	10 ¹⁶	10 ¹³	10 ¹⁰	10 ⁷
Mean Free Path, λ (cm)	10 ⁻⁵	10 ⁻²	10	10 ⁴	10 ⁷ (= 100 km)
Collision Rate, Z_v (s ⁻¹ cm ⁻³)	10 ²⁹	10 ²³	10 ¹⁷	10 ¹¹	10 ⁵
Type of Gas Flow	← viscous →		← Knudsen →	← molecular →	

Table 3.1: **Approximate values for typical vacuum parameters for several gas flow regimes.**

The Knudsen number defines the ratio of the mean free path λ_{mfp} of an atom traveling through a capillary to the length l of the capillary:

$$K_n = \frac{\lambda_{mfp}}{l} = \frac{k_B T}{\pi \sqrt{2} d^2 p l} \quad (3.1)$$

When $K_n \ll 1$, it signifies the presence of viscous flow regime, demonstrating traits akin to those of a continuous fluid. Conversely, when $K_n \gg 1$ in scenarios of extremely low pressures, where the mean free path surpasses the dimensions of the vacuum enclosure, the flow tends towards molecular behavior.

In the viscous state of a gas, one distinguishes further between turbulent and laminar flow. the value of another dimensionless quantity, the Reynolds number is defined as:

$$R_n = \frac{dv\rho}{\eta} \quad (3.2)$$

d represents the pipe diameter or the characteristic size of the vacuum component, while v , ρ , and η denote the gas velocity, density, and viscosity respectively, at the flow

temperature. Assessing the Knudsen and Reynolds numbers allows for the prediction of different flow regimes, which can be approximately discerned using the following relationships:

1. $R_n < 1200$ ($K_n < 0.01$): laminar (viscous gas state)
2. $R_n > 2200$ ($K_n < 0.01$): turbulent (viscous gas state)
3. $1.0 > K_n > 0.01$: intermediate (transition gas state)
4. $K_n > 1.0$: molecular (rarefied gas state)

When the pressure of a gas within a chamber or vessel is lower than the surrounding pressure, or if it falls below 300 mbar, the gas is classified as being in a vacuum state. According to this definition, 300 mbar represents the lowest atmospheric pressure typically encountered at the Earth's surface. Table 3.2 shows the different level of vacuum.

Pressure Level	Pressure (mbar)	Particles per cm ³
Atmospheric Pressure	1013.25	2.7×10^{19}
Low Vacuum (LV)	300 - 1	$10^{19} - 10^{16}$
Medium Vacuum (MV)	$1 - 10^{-3}$	$10^{16} - 10^{13}$
High Vacuum (HV)	$10^{-3} - 10^{-7}$	$10^{13} - 10^9$
Ultra-High Vacuum (UHV)	$10^{-7} - 10^{-12}$	$10^9 - 10^4$
Extreme-High Vacuum (XHV)	$< 10^{-12}$	$< 10^4$

Table 3.2: Vacuum levels with their respective pressure and particle density.

3.1.2 Vacuum system

The process of creating, cooling, and trap loading the atomic ensemble necessitates the use of two distinct pressure environments: a medium vacuum (MV) region and an ultra-high vacuum (UHV) (10^{-11} Torr) region. To achieve the lowest possible pressure in the UHV chamber, which serves as the science chamber, it is separated from the MV chamber, connected to the oven, by a high-impedance section. This arrangement minimizes convective heating of the atomic sample during the final cooling stages. The high impedance is facilitated by a differential pumping system, featuring a long stainless

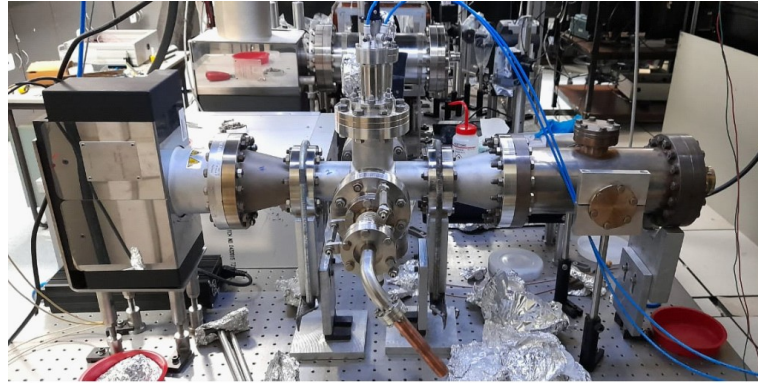
steel tube with an aperture of 5 mm in diameter and 8 cm in length, which ensures low conductance. This aperture significantly reduces the undesired gas flow from the MV to the UHV region. Figure 3.1 illustrates the experimental setup of the Rubidium system. The detailed description of the design is mentioned in the theses by Sunil Kumar [6] and Sumit Sarkar [102].

3.2 The oven

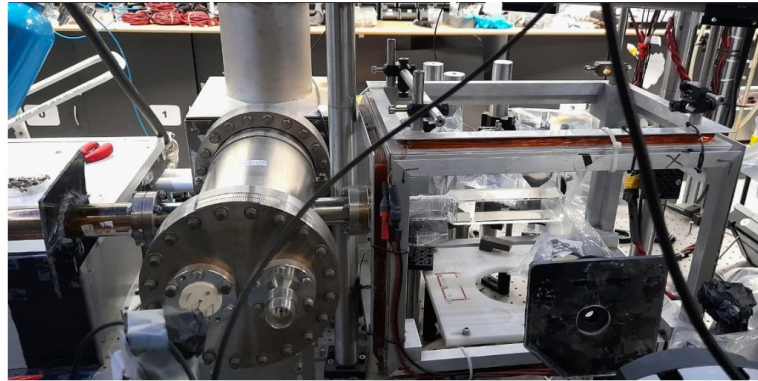
In our experiment, a thermal beam of ^{87}Rb atoms is generated using an effusive atomic source. The oven setup, depicted in Figure 3.2, illustrates the system used to produce the atomic beam. The cavity stores the atomic sample, which is heated to a specific temperature to generate the beam of atoms. The cavity contains a glass ampule with 5 grams of rubidium. The oven is constructed in a cylindrical, L-shaped design using 304L stainless steel and is welded onto a hollow flange of DN35CF-DN40CF. The reservoir is heated to $\sim 120^\circ$ to produce sufficient flux.

The hollow flange of DN35CF-DN40CF is attached to the cavity and secured to a separate blank flange featuring a microchannel array using copper gaskets and M6 screws. This secure sealing process prevents vacuum leaks, thereby protecting the atomic sample from oxidation. The microdrill arrays integrated into the blank flange ensure proper collimation of the atomic beam and direct it into the cold atomic chamber.

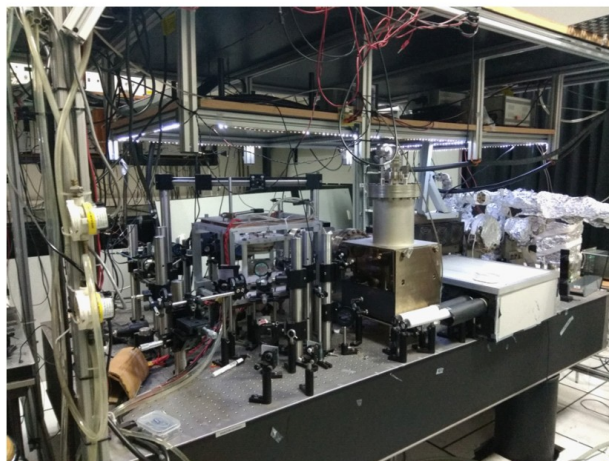
The oven is connected to a vacuum pump to maintain low pressure inside the oven which is measured using a pressure gauge connected to the vacuum pump. This ensures a proper pressure is maintained inside the oven well within the experimental conditions. The pressure is initially maintained at approximately 2×10^{-10} torr and increases to around 2×10^{-8} torr after six months of operation. To regulate the pressure inside the chamber, a copper cup with a small central opening is employed. This cup plays a crucial role in controlling the chamber's pressure. It is connected to a cold block situated outside the vacuum chamber via high current feedthroughs. The cold block is cooled to -18°C using a Peltier device. The low temperature of the copper cup stops atoms from reaching the ion pump by causing them to adhere to the cup's surface, thereby maintaining the vacuum level by functioning as a thermal conductor. The oven



(a)



(b)



(c)

Figure 3.1: **Images of the Vacuum System:** (a) The figure shows the experimental setup of the oven system and its connected ion pump. (b) This image displays the experimental setup of the science chamber. (c) This image presents the complete experimental setup.

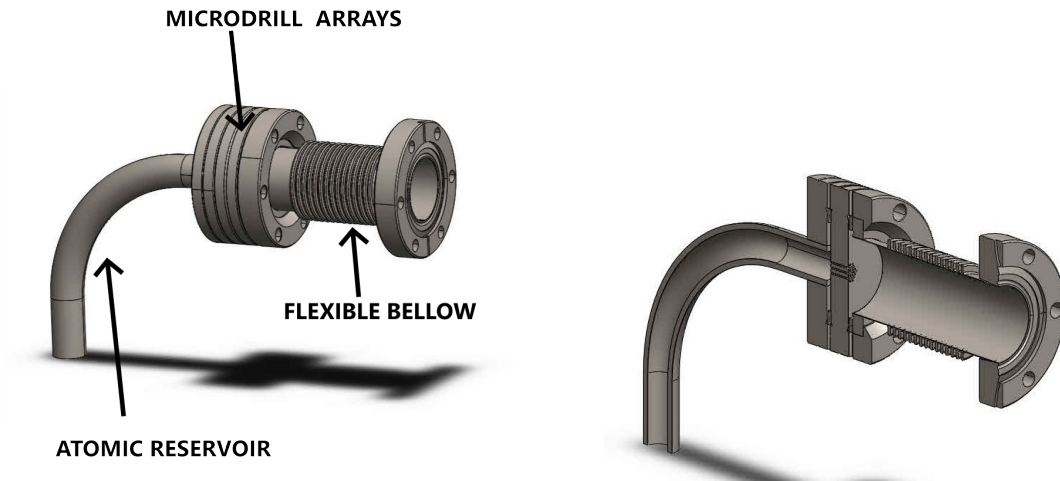


Figure 3.2: **CAD Images of the Rb Oven System:** The figures illustrate the design of the atomic reservoir, including the microdrill array and the flexible bellows. The second figure presents a cross-sectional view of the entire design.

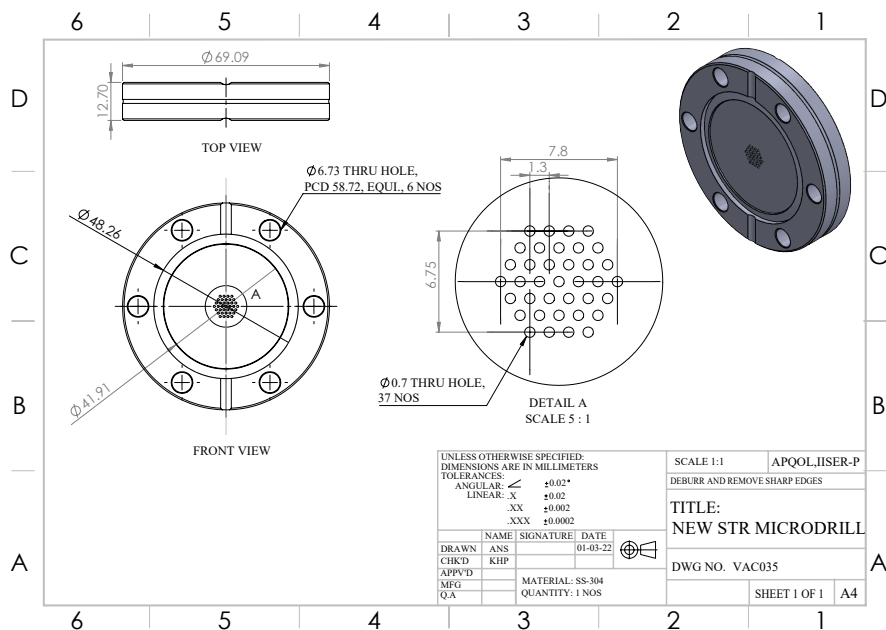


Figure 3.3: Machine drawing for the implemented oven system.

is also connected to an atomic beam shutter through a rotational feedthrough which is controlled using regulated air pressure which is further used to control the outflow of the atomic beam for the experiment.

The microchannel array is arranged in a hexagonal pattern to achieve the highest possible packing fraction. The microchannels located towards the periphery of the array are drilled at an angle in relation to the central microchannels on the blank flange. This design feature effectively enhances the collimation of the atomic beam. A common issue with effusive ovens is that a significant fraction of the atomic beam is lost as the emitted atoms diverge into a large solid angle, resulting in reduced atomic flux into the vacuum chamber where the MOT is generated and a shorter lifespan for the oven. However, by enhancing the collimation of the beam, both the lifespan of the atomic oven and the efficiency of atomic flux into the vacuum chamber are improved in the current setup.

3.3 Laser System

The laser cooling setup plays a crucial role in creating and controlling the light employed to cool the atomic sample. This includes the laser system which encompasses the magneto-optical trap MOT light and the re-pumper light. In ^{87}Rb the cooling and re-pumping transition cycle is given in the Figure 3.4

Within our experimental setup, we utilize semiconductor laser diodes made of GaAs, procured commercially and integrated into an external resonator to serve as light sources. One notable advantage of employing rubidium-87 within our interferometer lies in the fact that its D2 transition boasts an energy gap of 384 THz, equivalent to a laser wavelength of 780 nm

3.3.1 Laser diode's emission spectrum

One can express the oscillating electric field of a laser diode as a temporal evolution using the subsequent equation:

$$\vec{E}(t) = \vec{E}_0 e^{-i\omega t + \phi_0} \quad (3.3)$$

When a disturbance arises from the interaction between the electric field and its surroundings (such as spontaneous emission), the field encounters variations in both am-

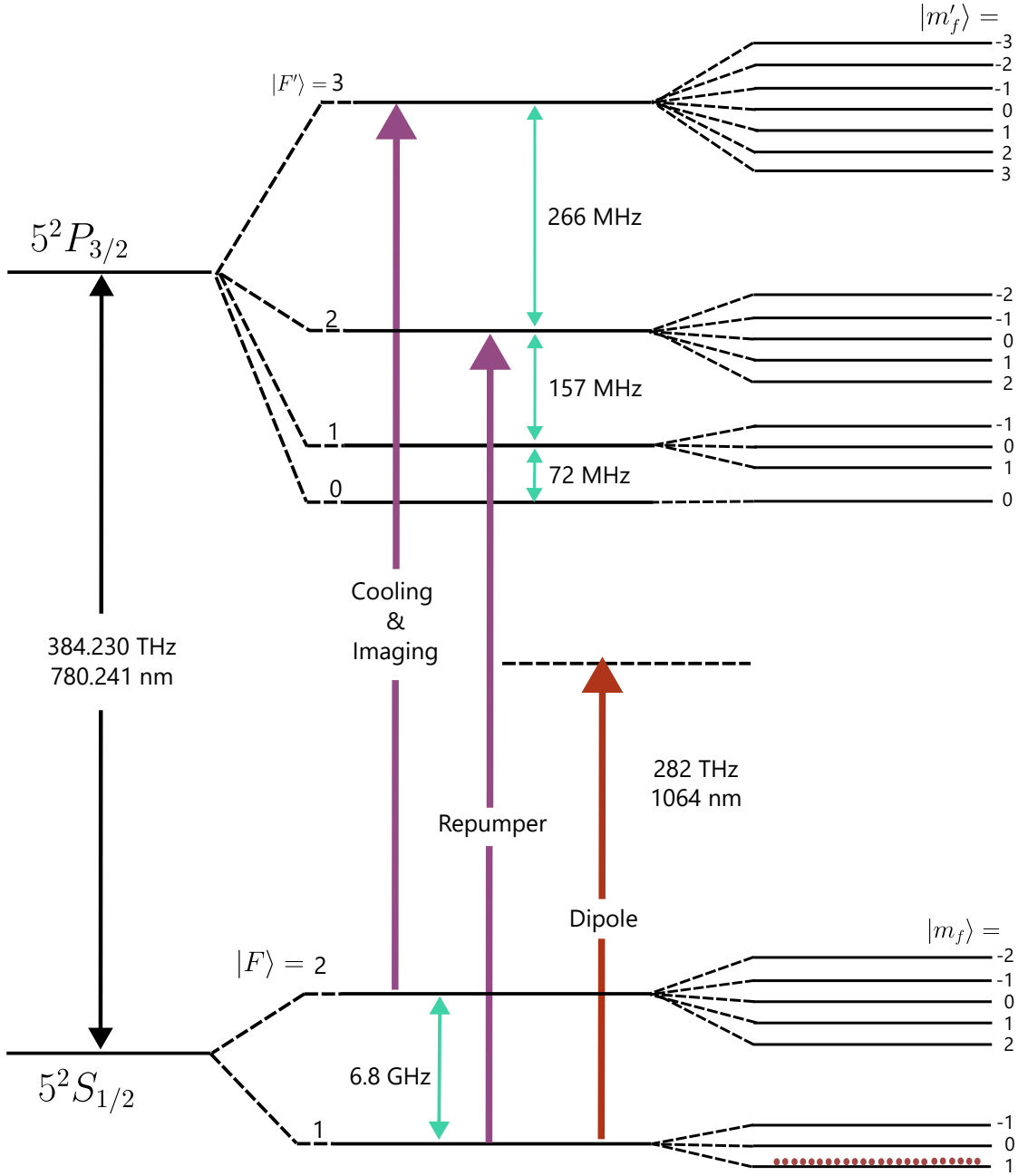


Figure 3.4: **The energy level diagram for cooling and trapping of atoms:** The ^{87}Rb D2 transition structure including the Zeeman level splitting. The atoms are cooled in a hybrid trap of magnetic and optical trap. At the completion of cooling the atoms occupy the $F = 1, m_f = -1$ ground state.

plitude, denoted by $\vec{E}_n(t)$, and phase, $\phi_n(t)$. Assuming we can differentiate between these alterations, the electric field can be expressed as:

$$\vec{E}(t) = \left\{ \vec{E}_0 + \vec{E}_n(t) \right\} e^{-i\omega t + \phi_0 + \phi_n(t)} \quad (3.4)$$

In the frequency domain, amplitude noise primarily contributes to an elevated noise floor, but it does not cause any broadening of the spectral line. In contrast, phase noise not only impacts the signal but also results in a broader linewidth, leading to a more significant spread in the frequency spectrum. The power spectral density of the electric field can now be written as:

$$PSD(\nu + \Delta\nu) = \frac{|\vec{E}_0|^2}{T} \cdot \frac{\theta_0^2 R_{\text{spontaneous}}/2}{(2\pi\Delta\nu)^2 + (\theta_0^2 R_{\text{spontaneous}}/2)^2} \quad (3.5)$$

Here, θ_0^2 represents the average phase contribution from a single spontaneous emission event, $R_{\text{spontaneous}}$ denotes the event rate, and T is the integration time of the analyzer. This forms a Lorentzian distribution, where the full width at half maximum (FWHM) corresponds to the linewidth of our laser, calculated as:

$$\Delta\nu_{FWHM} = \frac{\Delta\omega}{2\pi} = \frac{\theta_0^2 R_{\text{spontaneous}}}{2\pi} \quad (3.6)$$

We can rewrite the Equation 3.6 as derived by Schawlow and Townes in 1958 :

$$\Delta\nu_{FWHM} = \frac{\theta_0^2 R_{\text{spontaneous}}}{2\pi} = \frac{\pi h \nu_{FWHM} \Delta\nu_c^2}{P_L} \quad (3.7)$$

where $\Delta\nu_c$ is the cavity linewidth and P_L is the output power of the laser.

In semiconductor lasers, the linewidth is further broadened due to an additional coupling between amplitude and phase. As a result, the linewidth of a semiconductor laser diode is described by a modified Schawlow-Townes formula, which typically falls within the range of 100's of MHz. The modified formula is:

$$\Delta\nu_{FWHM} \geq \frac{\pi h \nu_{FWHM} \Delta\nu_c^2}{P_L} \cdot (1 + \alpha^2) \quad (3.8)$$

where, the factor $(1 + \alpha^2)$ is due to the variation in the complex refractive index caused

by a change in carrier density within a semiconductor diode.

The considerable width of semiconductor laser diodes' spectra poses an issue, as successful atom cooling demands that the optical linewidth remains narrower than the atomic ^{87}Rb D2 linewidth of $\Gamma/2\pi = 6\text{MHz}$. Thus one can reduce the linewidth by forming an external cavity using a diffraction grating. The basic block diagram of external cavity diode laser is given in Figure 3.5 The line width of the laser diodes

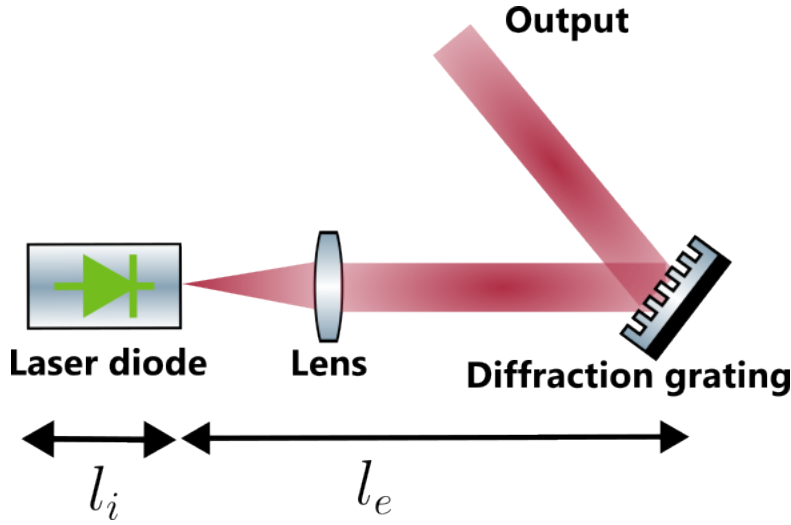


Figure 3.5: Schematic layout of an external cavity diode laser

depends on the linewidth of the cavity which scales linearly with the inverse of the mean lifetime of a photon in the cavity τ_c . The relation for a lifetime of a photon inside a combination of internal and external resonator is given as :

$$\tau_c = -\frac{2(n_i l_i + n_e l_e)}{c \ln(R_{1i}(1 - R_{2i})^2 R_{2e})} \quad (3.9)$$

where, $n_{i,e}$ is the refractive index of the cavity material, $l_{i,e}$ length of internal and external cavity and $R_{1i,2i,2e}$ are the reflectivity of different faces in the ECDL. With a rough estimate using typical values for a laser diode, such as $l_i = 250 \mu\text{m}$, $n_i = 3$, $R_{1i} = 0.95$, and $R_{2i} = 0.3$, and considering an external resonator employed in our experiment with $R_{2e} = 0.18$, $n_e = 1$, and $l_e = 40 \text{ mm}$, the average photon lifetime within the cavity increases by approximately 22-fold. Consequently, according to equation (4.19), the linewidth improves by a factor of about 500, thereby reducing it to below 200 KHz.

The lasers utilized in our experiments are diode lasers configured in Littrow setup (manufactured by TOPTICA Photonics AG, Model: TA-pro and DL-100). This setup involves the formation of an external cavity between the rear face of the laser diode and a diffraction grating with a density of 1800 lines/mm. The first-order diffracted beam from the grating is redirected back into the laser diode, while the zeroth-order beam constitutes the laser output. This optical feedback from the first-order diffracted beam effectively extends the resonator between the rear face of the laser diode and the diffraction grating. The length of this external cavity dictates the mode frequencies of the laser.

Adjusting the angle of the grating, facilitated by a piezoelectric transducer (PZT) mounted behind the grating, enables the modulation of the laser diode's frequency range. The angle of the grating is contingent upon the expansion and contraction of the PZT, thereby altering the cavity length and the grating's angle. Apart from the laser diode and grating, the Littrow configuration comprises various mechanical components, including a mounting base for the heat sink, a Peltier cooler, a base plate, a laser diode holder with a collimator, a grating mount with a piezo actuator, and a mirror for directing the output laser.

Ensuring a stable output frequency of the laser necessitates external mechanical vibration isolation, temperature control (Toptica DTC 110), and current regulation (Toptica DCC 110). Without these measures, the laser's output frequency may drift over time [102].

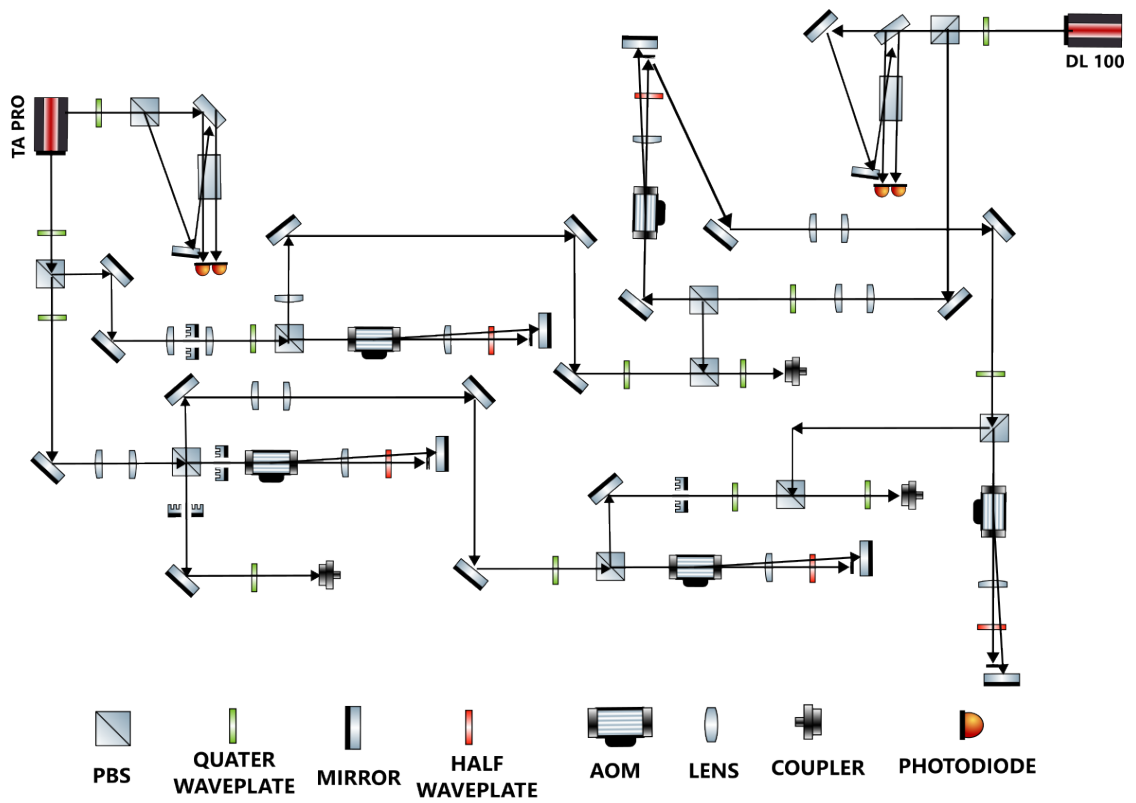
3.3.2 Cooling and re-pumping laser

The laser cooling mechanism plays a crucial role in generating and manipulating light for cooling the atomic sample, encompassing the provision of both the MOT light and the incorporation of a repump beam. For the ^{87}Rb hyperfine transition $F = 2 \rightarrow F' = 3$ of the D2 line at the wavelength $\lambda = 780 \text{ nm}$, utilized for cooling, due to its closed and cyclic nature. Despite the $F = 2 \rightarrow F' = 3$ transitions being a closed transition in nature, the nearby $F = 2 \rightarrow F' = 2$ line, with a frequency offset of $\Delta\omega = 2\pi \times 266 \text{ MHz}$, leads to considerable atom loss to the $F = 1$ ground state through off-resonant transitions. Consequently, a beam resonant with the $F = 1 \rightarrow F' = 2$ transition

becomes necessary to repump the lost atoms back.

The optics corresponding to the 3D MOT, imaging and generation of Bragg beam as shown in figure 3.6 are all generated on the main table from a single external cavity diode laser (ECDL) from TA-pro as discussed in section 3.3.1 producing approximately 150 mW of linearly polarized light. The output of the ECDL initially passes through an double stage optical isolators producing 60 dB isolation which limits the back transmitted light from a tapered amplifier (TA) further down the optics line. The high degree of isolation for ECDLs is required as any reverse transmitted light from the TA will destroy the ECDL from running single mode. On the output of the isolators the light is split via a half-waveplate ($1/2$) and polarizing beam splitter (PBS) along two paths. The light travels along four paths which are used for the zeeman cooling beam, cooling beam, the imaging, Bragg beam and frequency locking for the ECDL [6].

For switching and frequency control lines light is passed through an acoustic-optic modulator (AOM) such that the first order diffraction mode (+1) is dominant; all light then passes through a quarter-wave plate ($1/4$) and a lens; following the lens an iris blocks the zeroth order diffraction before the light is retro reflected along the same path; after the second pass through the $\frac{\lambda}{4}$ the light has the opposite linear polarization so it will pass the PBS; with proper alignment the first order diffraction on the second AOM pass will be along the same vector as the input beam; the frequency shifted light is then coupled to the apparatus table through a polarization maintaining optical fiber. Placing the lens such that both the AOM and retroreflector are at the focal length will ensure proper overlap and mode matching on the incoming and reflected beam. In order to reduce unwanted birefringent effects in the fiber such as polarization rotation or mixing, the incident beams are aligned to the fast and slow polarization axes of the fiber using a $\frac{\lambda}{2}$. Proper axis alignment will result in an extinction ratio of 30-35 dB while the fiber is mechanically or thermally stressed. The light on the output of the double pass AOM will have been frequency shifted by twice the AOM driving frequency. All AOMs in the cooling system are driven through a voltage controlled oscillator (VCO) in series with a transistor-transistor logic switch (TTL) and radio frequency amplifier. The voltage control and switch signal for the VCO and TTL is provided from the control computer.



(a)

Figure 3.6: **Optical Layout of the Laser System:** A schematic diagram depicting the optical layout of the cooling and repumping laser system. Further details can be found in Sunil Kumar's thesis [6].

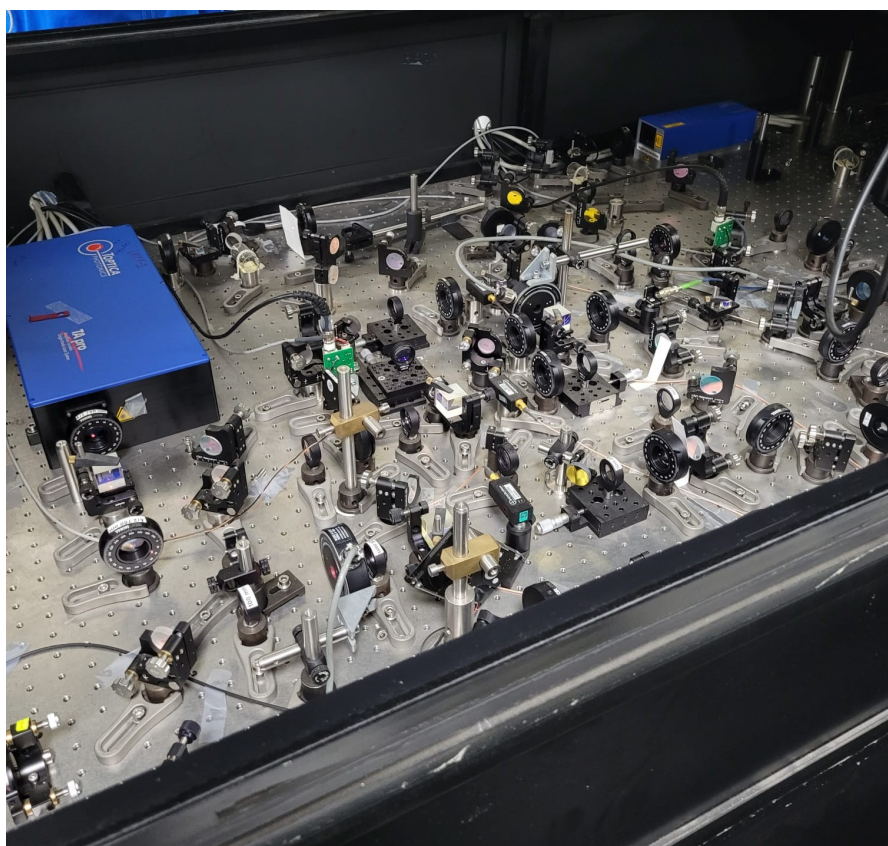


Figure 3.7: **Optical Layout of the Laser System:**The experimental setup of the optical layout

3.3.3 Laser for Bragg lattice

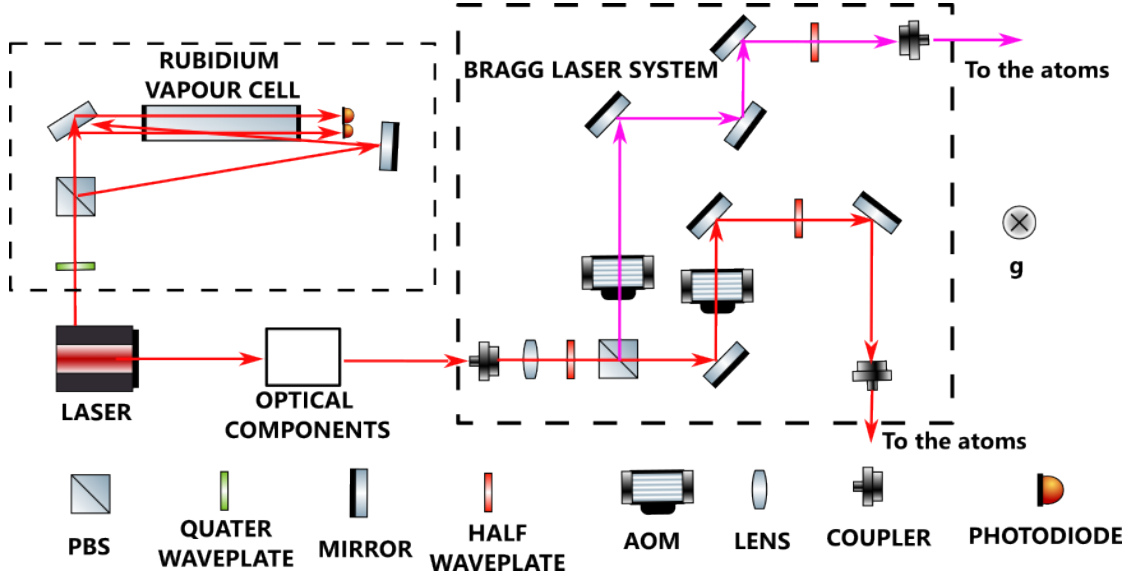


Figure 3.8: **Laser Beam Preparation for Bragg Lattice:** A schematic diagram illustrating two independent laser beams separated by $\Delta\omega \sim 15\text{ kHz}$ to generate the Bragg beams. The left dashed block represents the spectroscopy of ^{87}Rb , locked to the $5^2\text{S}_{1/2}, F=2 \rightarrow 5^2\text{P}_{3/2}, F'=2$ D2 transition at 780 nm. The right dashed block depicts the configuration of the Bragg laser system.

The Bragg laser system manipulates the frequency of light to create the desired Bragg lattice for atomic sample interaction. Figure 3.8 illustrates the optical layout of the Bragg beams. These beams are seeded by the primary cooling laser, which is red-detuned by 6.6 GHz from the atomic transition to minimize spontaneous emission. To address noise and space constraints, the main laser source is positioned on a separate table. The laser output is fiber-coupled to another optical table, where the experimental procedures are conducted.

The light is collimated using an achromatic collimator and then split equally into two different paths using a combination of a $\lambda/4$ wave plate and a polarizing beam splitter (PBS). These beams are subsequently directed into two separate acousto-optic modulators (AOMs), which are driven by an arbitrary function generator phase locked to each other at 80 MHz and 80.015 MHz, respectively. Two separate waveplates $\lambda/2$ are used in individual paths to avoid any polarization noise into the fibers. Fig. 3.9

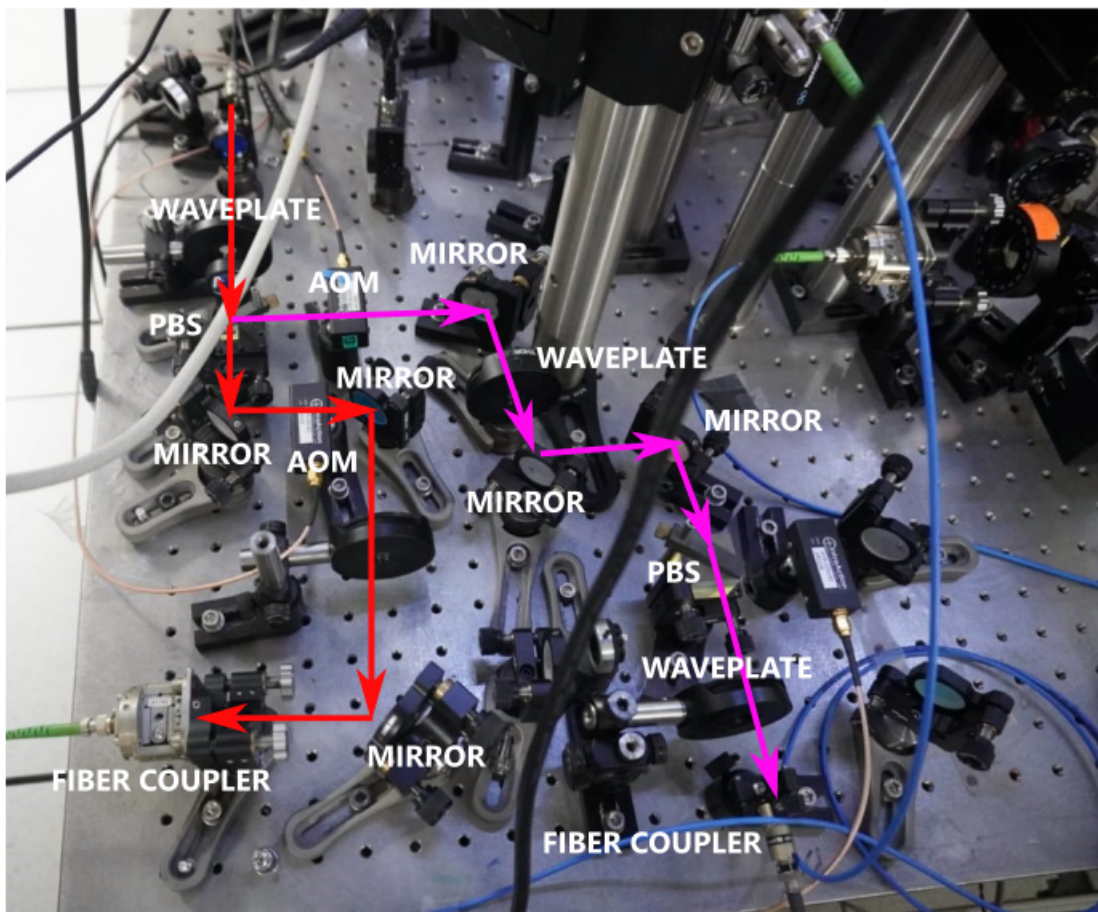


Figure 3.9: **Laser Beam Preparation for Bragg Lattice:** The experimental setup is depicted in the photograph.

shows the experimental picture of the Bragg layout.

3.3.4 Optical dipole trap

An Optical Dipole Trap (ODT) utilizes the interaction between neutral atoms and the electric field $\mathbf{E}(\mathbf{r})$ generated by a focused laser beam to confine atoms in a specific region of space. The oscillating electromagnetic field induces a dipole moment in the atoms, leading to a potential well that attracts the atoms toward the region of highest intensity, typically the center of the laser beam. In this scenario, the oscillating electromagnetic field emanates from a laser beam. The electric field induces opposing forces on its constituent parts: the positively charged nucleus moves in the direction of the field, while the negatively charged electron cloud moves in the opposite direction.

When the external electric field \mathbf{E} isn't excessively strong, the electric forces pulling the electron cloud and the nucleus apart don't surpass the Coulomb force. Instead, they reach a stable equilibrium. Consequently, the neutral atom becomes polarized, resulting in an induced dipole moment \mathbf{p} , which can be approximated by equation $\mathbf{p} = \alpha\mathbf{E}$ where α is the atomic polarisability.

In this classical approach, which is also called Lorentz model, considering a oscillatory field i.e. $\mathbf{E}(\mathbf{r}, t) = \mathbf{E}_0(\mathbf{r})e^{-i\omega t} + \text{c.c}$ and with the complex dipole moment \mathbf{p} and the complex polarisability $\mathbf{p}(\mathbf{r}, t) = \mathbf{p}_0(\mathbf{r})e^{-i\omega t} + \text{c.c}$, which is a function of the driving frequency ω [103] The potential felt by the atom due to the induced dipole interaction mentioned earlier can be determined by integrating $dU = -\mathbf{p} \cdot d\mathbf{E}$ to obtain:

$$U_{dipole} = -\frac{1}{2}\langle \mathbf{p} \cdot \mathbf{E} \rangle = -\frac{1}{2\epsilon_0 c} \text{Re}(\alpha) I(\mathbf{r}) \quad (3.10)$$

The angle brackets signify the time average where the factor $\frac{1}{2}$ arises from the integration and is absent for a permanent dipole and where $\mathbf{I}(\mathbf{r}) = 2\epsilon_0 c |\mathbf{E}_0(\mathbf{r})|^2$ is the electric field intensity. Since the potential is conservative, the force is given by $\mathbf{F}_{dipole}(\mathbf{r}) = -\nabla U_{dipole}(\mathbf{r})$.

With the above expression, the general expressions for the dipole potential simplify to

$$U_{dip}(\mathbf{r}) = \frac{3\pi c^2}{2\omega^3} \left(\frac{\mu_0}{4\pi} \right) I(\mathbf{r}) \quad (3.11)$$

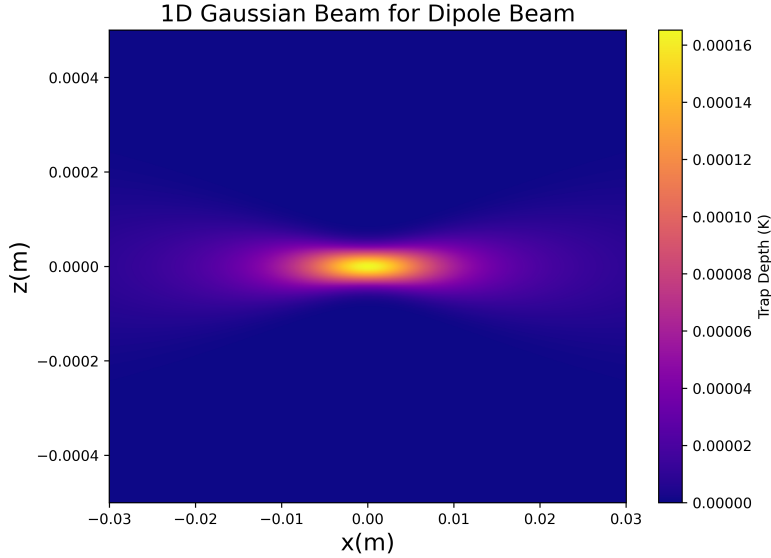


Figure 3.10: **Static Trap Depth for Dipole Beam:** The calculated trap depth for a single-beam dipole trap with a wavelength of 1064 nm. The dipole beam is traveling along the x direction. This trap utilizes a Gaussian beam with a power of $P = 5$ W and a beam waist of $w_0 = 50 \mu\text{m}$.

For a Gaussian beam of power P , its intensity distribution is characterized by the following expression:

$$I(r, z) = \frac{2P}{\pi w(z)^2} \exp\left(-\frac{2r^2}{w(z)^2}\right) \quad (3.12)$$

where $w(z)$ is the radius of the beam at position z . Since the Gaussian profile extends to infinity, this radius is defined as the distance from the beam axis where the intensity drops to $1/e^2$ (approximately 13.5%) of the maximum. Figure 3.10 shows the calculated trap depth for a single beam dipole trap using a Gaussian beam.

Figure 3.11 presents the schematic layout for extracting two laser beams to meet the specified criteria. The 20 W laser beam is split into two parts using a combination of a half-wave plate and a polarizing beam splitter (PBS) cube. This method is favored over a single beam splitter, as the latter only produces two beams with equal power, whereas the combination of a half-wave plate and PBS cube allows for adjustable power distribution between the two paths.

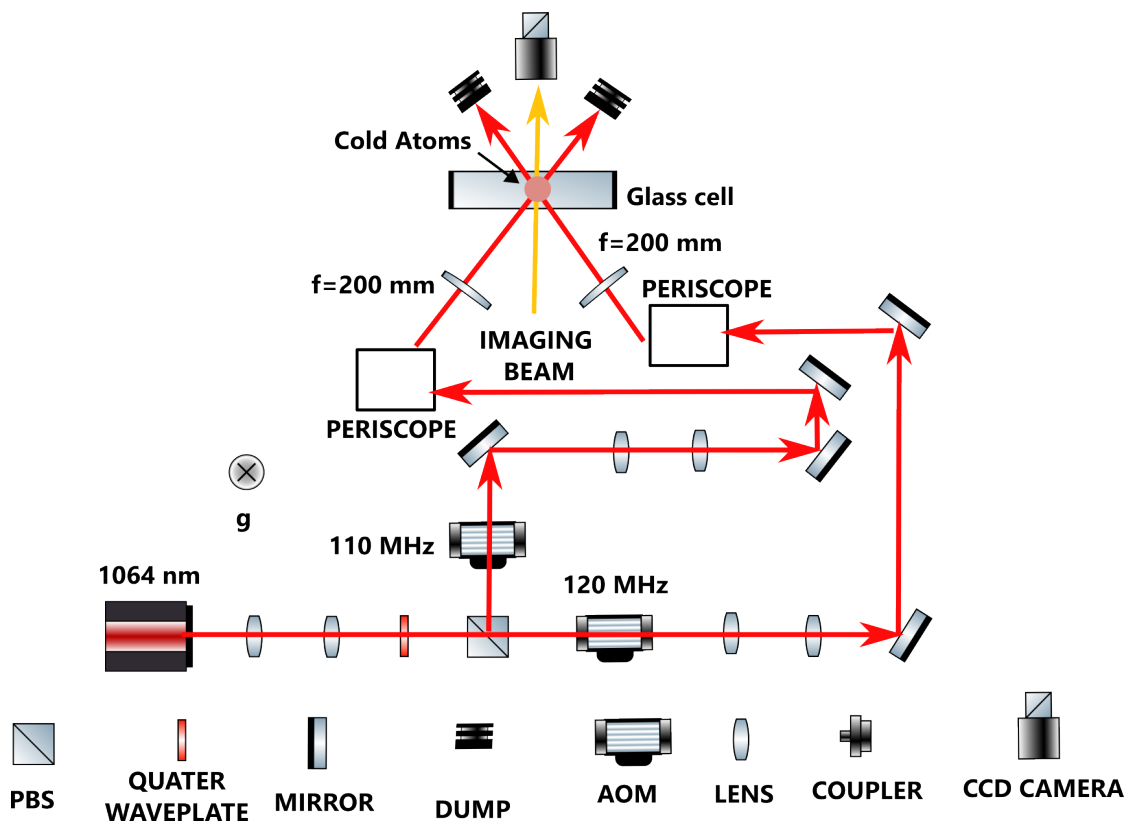


Figure 3.11: **Laser Beam Preparation for Optical dipole trap:** A schematic diagram illustrating the generation of dipole beams for evaporative cooling.

Each laser beam exiting the PBS cube is directed through an acousto-optic modulator (AOM), operating at center frequencies of 110 MHz and 120 MHz, respectively. The +1st and -1st order diffracted beams from each AOM are utilized for further experimentation. Consequently, the two laser beams differ in frequency by 230 MHz, preventing interference during the experiment. The power of each beam can be individually controlled by adjusting the RF power supplied to the AOMs, which also allows for fast beam switching.

Due to the smaller active aperture of the AOMs compared to the natural beam diameter, a telescope is employed to reduce the beam size and achieve high diffraction efficiency. The AOMs used in the experiment are not designed for high power operation and have a smaller active aperture, resulting in a maximum diffraction efficiency of 70%. A larger beam diameter is desired before passing through the final lens to achieve a tight focus. Therefore, after the AOMs, another telescope is used in each beam path to increase the beam diameter again. Following these final telescopes, two beams with approximately 5 W power each are obtained. The final beam waist used in our experiment is approximately of $100\ \mu\text{m}$ which correspond to a trap depth of approximately $50\ \mu\text{K}$. The temperature of atoms obtained after evaporative cooling is approx 200 nK. The detailed description of the optical setup can also be found in Sumit Sarkar thesis [102]. We utilize a hybrid trap, combining a quadrupolar magnetic field with a crossed optical dipole trap, for evaporative cooling. While the optical dipole trap is spin-independent, the magnetic field generates a trapping potential exclusively for the $m_F = -1$ hyperfine level.

3.4 Summary

To summarize, this chapter provides a concise overview of the experimental setup. It includes both schematic diagrams and actual photographs of the equipment where applicable. A brief description of the newly designed oven, which incorporates modifications to the previous setup, is presented. Additionally, the chapter introduces the Bragg laser system, which is employed in later experiments to demonstrate the atom interferometer.

Chapter 4

Bragg Diffraction and Atom Interferometry

4.1 Bragg diffraction of Atoms in momentum space

The periodic spacing of the crystals coincided with the X-ray wavelengths, resulting in constructive interference of the scattered radiation at specific incidence angles θ_b , as described by Bragg's law:

$$n\lambda = 2d_{\text{crystal}} \sin(\theta_b) \quad (4.1)$$

Here, n is the order of diffraction, λ represents the wavelength of the X-rays, and d_{crystal} is the crystal's periodic spacing.

Manipulating atoms similarly to light with optical components is termed atom optics. An atom-optical element, or light crystal, can be formed by the interference of two laser beams at wavelength λ_L at the atom's location. This interference generates a one-dimensional intensity pattern expressed as:

$$I(x) = 2c\epsilon_0 E_0^2 \cos^2(kx) \quad (4.2)$$

where c is the speed of light, ϵ_0 is the permittivity of free space, and E_0 is the electric field amplitude. Here, the crystal spacing d_{crystal} is replaced by the optical lattice spacing $d_{\text{light}} = \lambda_L/2$. For atoms with mass m and velocity v , the thermal de Broglie wavelength

λ_{dB} is given by $\lambda_{\text{dB}} = \frac{2\pi\hbar}{mv}$. The new resonance condition then becomes:

$$n\lambda_{\text{dB}} = \lambda_L \sin(\theta_b) \quad (4.3)$$

This condition can be met by accelerating atoms towards a standing wave. In most cold atom experiments, atoms are typically stationary when exposed to an optical lattice. A moving optical lattice can be created by interfering two laser beams with a frequency difference δ , producing a time-dependent intensity pattern:

$$I(x) = 2c\epsilon_0 E_0^2 \cos^2(kx - \Delta\omega t/2) \quad (4.4)$$

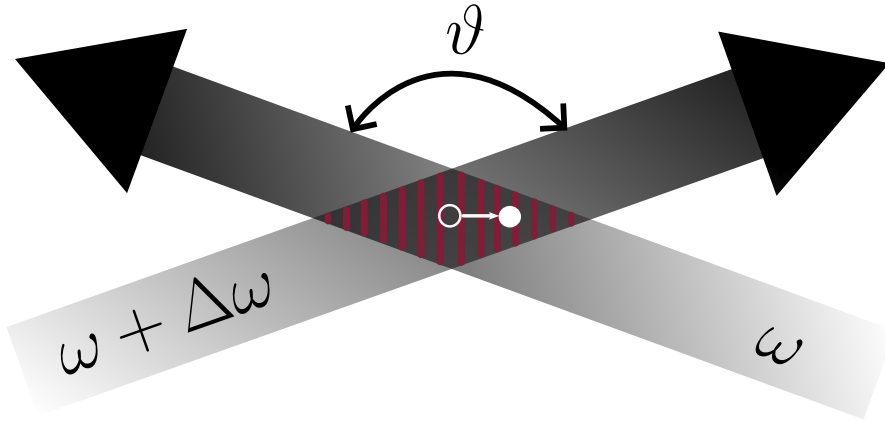


Figure 4.1: Bragg diffraction of atoms. Atoms engage with photons emitted by two laser beams, which have frequencies of ω and $\omega + \Delta\omega$ and intersect at an angle ϑ . These atoms can experience coherent diffraction, transitioning from an initial momentum state $|p_0\rangle = |0\hbar k\rangle$ to a final momentum state $|p_r\rangle = |2\hbar k \sin(\vartheta/2)\rangle$, provided that the energy difference between the laser beams meets the condition $\hbar\Delta\omega = \frac{p_r^2}{2m}$. This happens when atoms are exposed to two counter-propagating laser beams, they can undergo a process where they first absorb a photon from one beam, gaining its momentum, and then undergo stimulated emission into the opposing beam, emitting a photon and experiencing a recoil in the opposite direction.

In a simplified model, an atom absorbs a photon from one laser beam and is coherently stimulated back to the ground state by a photon from another beam. This two-photon Raman process imparts a momentum $p_r = 2\hbar k \sin(\vartheta/2)$ to the scattered atom relative to the unscattered atoms in the Bose-Einstein condensate (BEC). The laser beams have a wave vector $k = 2\pi/\lambda_L$ and are aligned at an angle ϑ , with $k_\omega \approx k_{\omega+\Delta\omega} \equiv$

k since $\Delta\omega \ll \omega$.

To conserve energy during Bragg diffraction, the laser beams must have a specific frequency difference δ , given by the effective energy difference between the two coupled ground states:

$$\Delta E = \frac{p_r^2}{2m} = \frac{(2\hbar k \sin(\vartheta/2))^2}{2m} = \hbar((\omega + \Delta\omega) - \omega) = \hbar \Delta\omega \quad (4.5)$$

For atoms with initial momentum p_0 , the condition modifies to:

$$\Delta E = \frac{(p_r + p_0)^2 - p_0^2}{2m} = \frac{(2\hbar k \sin(\vartheta/2) + mv_0)^2 - m^2v_0^2}{2m} = \hbar\Delta\omega \quad (4.6)$$

Thus, the frequency difference δ for the Bragg laser beams is:

$$\Delta\omega = 4\omega_r \sin^2(\vartheta/2) + 2kv \cdot \sin(\vartheta/2) \quad (4.7)$$

where the recoil frequency $\omega_r = \hbar k^2/m$. In our setup, with an incidence angle $\vartheta = 180^\circ$, the laser beams are anti-parallel. For first-order Bragg diffraction with stationary ($p_0 = 0$) ^{87}Rb atoms, the required frequency difference is $\Delta\omega = 4\hbar k^2/m = 4\omega_r = 2\pi \cdot 15.08 \text{ kHz}$. Figure 4.2 illustrates the Bragg diffraction and the first-order Rabi oscillations of the condensate. The Rabi frequency is determined to be $2\pi \times 5 \text{ kHz}$.

4.1.1 Higher order Bragg diffractions

In the preceding discussion, we explored the concept of first-order Bragg diffraction, which can be generalized to encompass higher-order scenarios. The equation 4.6 can be adapted as follows:

$$\Delta E = \frac{(np_r + p_0)^2 - p_0^2}{2m} = \frac{(2n\hbar k \sin(\vartheta/2) + mv_0)^2 - m^2v_0^2}{2m} = \hbar n \Delta\omega_n \quad (4.8)$$

Here, n represents the order of diffraction, thus the frequency difference between the laser beams for the n -th order Bragg diffraction is given by:

$$\Delta\omega_n = 4n\omega_r \sin^2(\vartheta/2) + 2kv \cdot \sin(\vartheta/2) \quad (4.9)$$

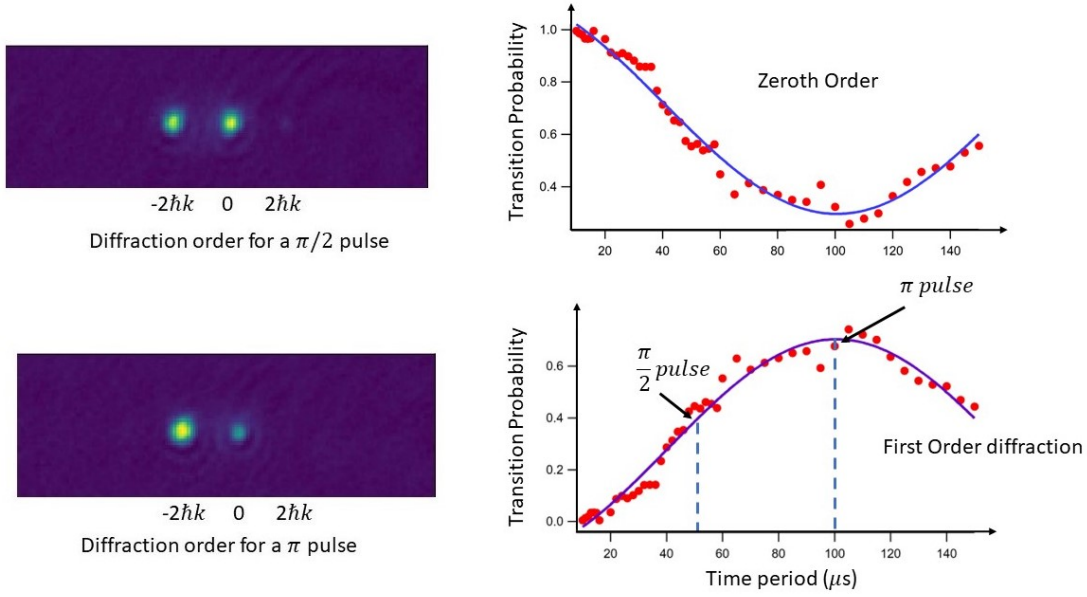


Figure 4.2: Image of Bragg diffraction and Rabi oscillation for $\pi/2$ and π pulse

For a sixth-order Bragg pulse applied to zeroth order ^{87}Rb atoms ($p_0 = 0$), an optical lattice with a frequency difference of $\Delta\omega_6 = 24 \cdot \omega_r \approx 2\pi \cdot 90 \text{ kHz}$ would be required.

The effective Rabi frequency can be obtained from:

$$\Omega_{\text{eff}}^{(n)} = \frac{\Omega^{2n}}{2^{n-1} \Delta_1 \Delta_2 \dots \Delta_{n-1}} \quad (4.10)$$

In this context, Ω_0 signifies the single-photon Rabi frequency, and Δ_i represent the detunings from various virtual levels, as depicted in Fig. 4.3.

Rabi oscillations between the coupled momentum states $|0\hbar k\rangle$ and $|2\hbar k\rangle$ were measured using the described experimental setup. Figure 4.2 presents the diffraction efficiency as the ratio of the number of diffracted atoms to the total atom number, plotted as a function of the pulse duration τ for square-shaped pulses. The experimental data were modeled using the equation:

$$\frac{N_{2\hbar k}}{N_{\text{tot}}} \sim A \cdot (1 - e^{-\tau/t_0} \cos(\Omega_{\text{eff}} \cdot \tau)),$$

where damping, characterized by the decay constant t_0 , is incorporated to account for the momentum selectivity of the Bragg pulses. The pulse duration τ was scanned

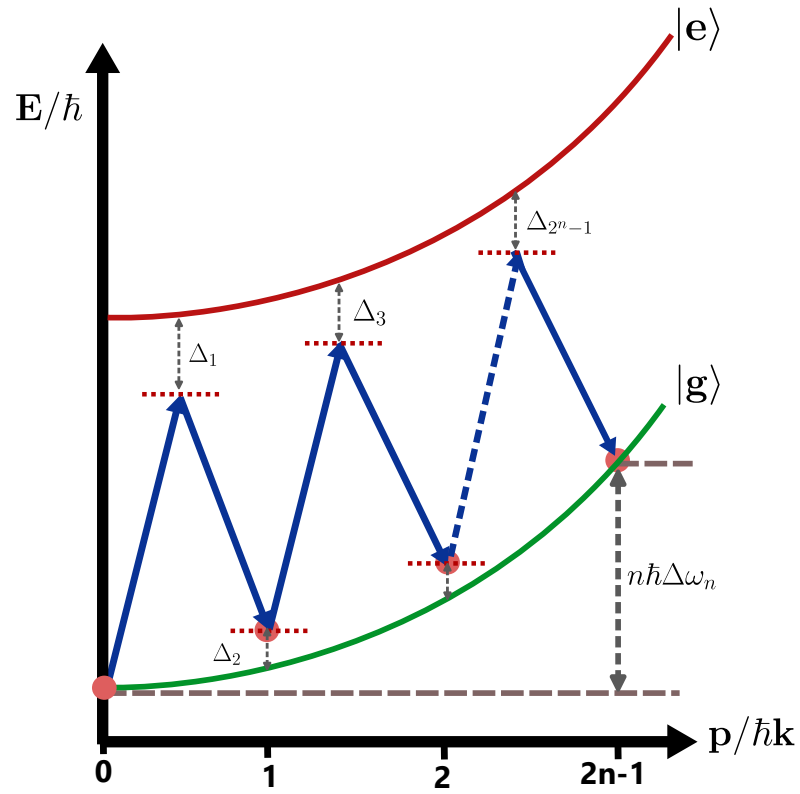


Figure 4.3: **Schematic representation of n -th order Bragg diffraction.** For coherent coupling between the momentum states $|0\hbar k\rangle$ and $|2n\hbar k\rangle$, energy conservation necessitates that $\hbar n\Delta\omega_n = \frac{(2n\hbar k)^2}{2m}$. The energy levels are indicated by their transverse momentum states, expressed in units of $\hbar k$. The corresponding detunings for the ground and excited states are represented by Δ_i .

from 0 to 150 μs for an initial expansion time of $T_0 = 2$ ms. Following the application of the Bragg pulse, the time-of-flight duration was set to $T_{\text{tof}} = T_0 + T_{\text{sep}} = 10$ ms to allow the spatial separation of the atomic ensembles prior to detection.

By fitting the above equation to the experimental data, the π -pulse duration was determined to be $\tau_\pi = 100$ μs with a diffraction efficiency of approximately 0.90. Using this result, the effective Rabi frequencies and the corresponding beam intensities at the atomic position were calculated as:

$$\tau_\pi = \frac{\pi}{\Omega_{\text{eff}}} = \frac{\pi \hbar \Delta \omega^3}{3\pi c^2 \Gamma I},$$

where $\Delta \omega$ represents the detuning, I is the laser beam intensity, and Γ is the linewidth of the atomic transition. This analysis yielded an effective Rabi frequency of $\Omega_{\text{eff}}^{10\text{ms}} = 2\pi \cdot 5$ kHz.

We have also now shown the diffraction for the 7th order (i.e., $14\hbar k$) in Fig. 4.4. Additionally, the figure illustrates the Rabi oscillation corresponding to the 6th order.

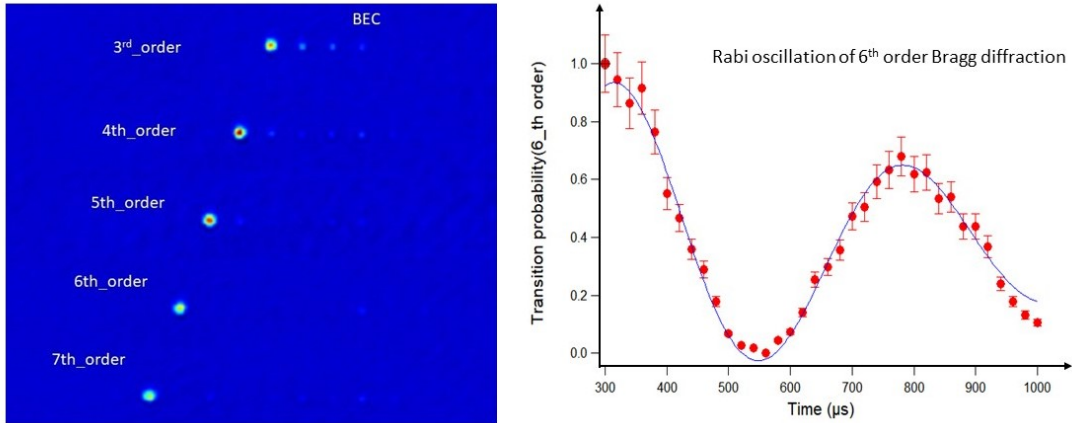


Figure 4.4: **Higher Order Bragg Diffraction.** (a) Image showing higher order Bragg diffraction of the condensate. (b) Rabi oscillation of 6th order Bragg diffraction.

4.2 Bragg spectroscopy of Atoms in momentum space

Till now we considered the Bragg diffraction of single atoms. In an ideal condition when we consider the atoms can be transferred to the higher momentum state with 100% if the

resonance condition is fulfilled. Even a sub-recoil Bose-Einstein Condensate (BEC) exhibits a finite expansion rate, which is linked to an effective momentum spread Δp_{rms} . Consequently, when a Bragg lattice with fixed $\Delta\omega$ is applied, some atoms within the distribution remain off-resonance and thus oscillate with a diminished amplitude between the coupled states.

In the case of Bragg diffraction with $n = 1$ and $\vartheta = 180^\circ$, Eq. 4.8 can be used to establish a resonance condition for atoms with an initial momentum p_0 :

$$p_0(\Delta\omega) = \frac{m\hbar\Delta\omega}{p_r} - \frac{p_r}{2} = m \left[\frac{\Delta\omega - 4(\hbar k^2/2m)}{2k} \right] \quad (4.11)$$

In a simplified scenario, atoms that satisfy Eq. 4.11 are diffracted and become spatially separated from the portion of the cloud that remains un-diffracted, provided the initial momentum spread of the cloud is less than the transferred momentum ($\Delta p_{rms} < p_r$). Under these circumstances, we can vary δ , measure the diffraction efficiency for specific momentum classes, and analyze the resulting distribution in momentum space. This technique is known as Bragg spectroscopy (BS).

The Bragg spectroscopy of the Bose-Einstein condensate, illustrated in Figure 4.4, has been analyzed. Atoms are diffracted through their interaction with Bragg beams, where the mutual detuning $\Delta\omega$ between the beams determines which momentum component is extracted from the degenerate gas condensate. In this experiment, we applied a pulse duration of $\tau = 100 \mu s$ and varied the frequency detuning from $\Delta\omega = 8$ to 21 kHz, which aligns with the first-order Bragg diffraction for stationary Rubidium-87 atoms at $\Delta\omega \sim 15$ kHz. The resulting image was captured after a time of flight of $200 \mu s$.

4.2.1 Momentum width of the BEC

The wave function in momentum space for a given interval can be defined as:

$$\Delta k_n : \left(n - \frac{1}{2} \right) |2\hbar k| < k_x \leq \left(n + \frac{1}{2} \right) |2\hbar k|.$$

Focusing solely on first-order Bragg diffraction within the non-interacting regime, the atomic state $\psi(k_x, t)$ can be represented in two momentum zones, Δk_0 and Δk_1 , as:

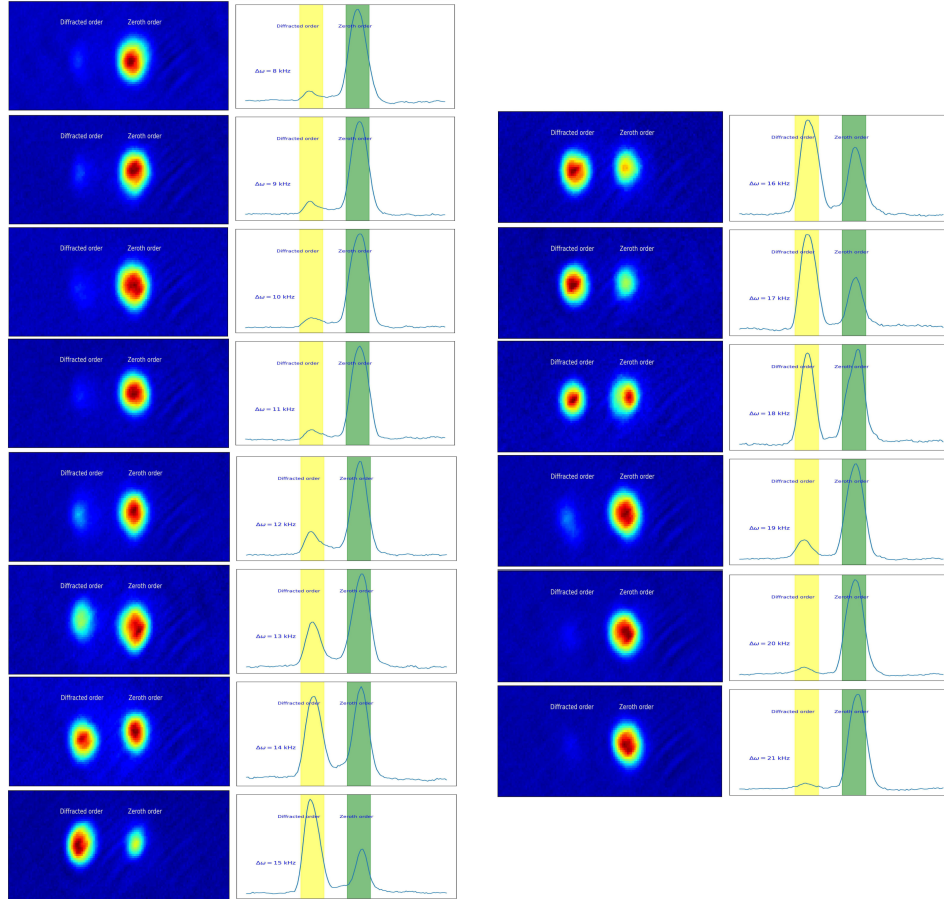


Figure 4.5: **Bragg spectroscopy of Bose-Einstein condensates in momentum space.** In each sequence from top to bottom, the duration of the box-shaped Bragg pulses is fixed at $\tau = 100 \mu s$, while the detuning $\Delta\omega$ is varied from 8 kHz to 21 kHz. The momentum distribution is observed after time of flight of $200 \mu s$. Atoms that are diffracted are highlighted with a yellow box, and the corresponding zeroth order is marked in green box.

$$\psi(k_x, t) = \phi_{k_x} \cdot \begin{pmatrix} c_0(k_x, t) \\ c_{2\hbar k}(k_x, t) \end{pmatrix},$$

where ϕ_{k_x} represents the wave function in momentum space, while $c_0(k_x, t)$ and $c_{2\hbar k}(k_x, t)$ denote the time-dependent coefficients corresponding to the amplitudes of the two diffraction orders. The variable k_x represents the atomic momentum along the direction of the beam splitter.

The time evolution of the coefficients $c_i(k_x, t)$ is governed by the Gross-Pitaevskii equation in momentum space. Under the assumption that the Bragg lattice acts as a plane-wave classical field, the non-interacting dynamics are described by:

$$i \frac{\partial}{\partial t} \begin{pmatrix} c_0(k_x, t) \\ c_{2\hbar k}(k_x, t) \end{pmatrix} = \begin{pmatrix} \frac{\hbar k_x^2}{2m} & \frac{\Omega_{\text{eff}}}{2} \\ \frac{\Omega_{\text{eff}}}{2} & \frac{\hbar}{2m}(k_x + 2k)^2 - \Delta\omega \end{pmatrix} \cdot \begin{pmatrix} c_0(k_x, t) \\ c_{2\hbar k}(k_x, t) \end{pmatrix},$$

where Ω_{eff} is the effective Rabi frequency, k denotes the wave vector of the beam splitters, and $\Delta\omega$ represents the detuning.

The momentum-space atomic distribution is approximated as a Gaussian wave packet, with its modulus squared given by:

$$|\phi(k_x)|^2 = \frac{1}{\sqrt{2\pi}\sigma_{k_x}} \exp\left(-\frac{k_x^2}{2\sigma_{k_x}^2}\right).$$

In simulations, the atoms are modeled as a Gaussian wave packet with a momentum width of $\sigma_{k_x} = 0.11\hbar k$. This approximation is based on Bragg spectroscopy of freely expanding atoms released from a shallow trap characterized by $\omega_x = 2\pi \cdot 200$ Hz after an expansion time of $T_0 = 10$ ms.

The effective detuning arises solely from the Doppler width of the atomic cloud. The Rabi amplitude in the momentum zone Δk_1 , as a function of time, is determined by:

$$|c_{2\hbar k}(k_x, t)|^2 = \frac{\Omega_{\text{eff}}^2}{\Omega_{\text{eff}}^2 + \left(\frac{2\hbar k k_x}{m}\right)^2} \sin^2\left(\sqrt{\Omega_{\text{eff}}^2 + \left(\frac{2\hbar k k_x}{m}\right)^2} \cdot \frac{\tau}{2}\right),$$

where Ω_{eff} is substituted based on prior measurements. The expectation value of the wave function $\psi_{2\hbar k}$ after the beam splitter operation can then be expressed as:

$$|\psi_{2\hbar k}(k_x, t)|^2 = |\phi(k_x)|^2 \cdot |c_{2\hbar k}(k_x, t)|^2,$$

For atoms that are off-resonance ($\epsilon_{\text{eff}} \neq 0$), oscillations occur at higher frequencies but with reduced amplitudes. A narrower initial momentum width of the atomic distribution enhances the uniformity of the Rabi frequency across the ensemble, thereby improving the beam splitter's efficiency. Alternatively, increasing the Rabi frequency results in power broadening of the Rabi amplitude, enabling the use of shorter pulse durations.

The full width at half maximum (FWHM) of the distribution, which defines the range of k_x around the Bragg resonance point where the probability of momentum transfer exceeds 1/2, can be expressed as:

$$\sigma_{c_{2\hbar k}}(k) = \frac{m\Omega_{\text{eff}}}{2\hbar k},$$

indicating a linear dependence on the effective Rabi frequency Ω_{eff} . The Rabi cycling behavior of the entire wave packet is influenced by the ratio between the power-broadened width $\sigma_{c_{2\hbar k}}(k)$ and the initial state's momentum width σ_{k_x} , where efficient cycling occurs when $\frac{\sigma_{c_{2\hbar k}}(k)}{\sigma_{k_x}} \geq 1$ [104].

In the case of a Gaussian wave packet with an rms momentum width of $\sigma_{k_x} = 0.11\hbar k$, the result aligns with the experimentally observed diffraction efficiency of 90%, as illustrated in Figure 4.5.

4.3 Atom Interferometry

Introducing individual pulses separated by an interferogram time T , comprising of $\pi/2$, π , and $\pi/2$ pulses, forms an atom interferometer known as the Mach-Zehnder type interferometer. During the first pulse, the photon recoil transferred causes the ground state $|g\rangle$ to spatially excite to a higher momentum state, akin to the Bragg case, or an excited state $|e\rangle$ in the Raman case, over time. Subsequently, the second pulse inverts states and momentum, while the third pulse serves to close the interferometer.

Let us now consider this sequence to derive the phase evolution used in our experiment. This phase evolution determines the population ratio in the output of the interfer-

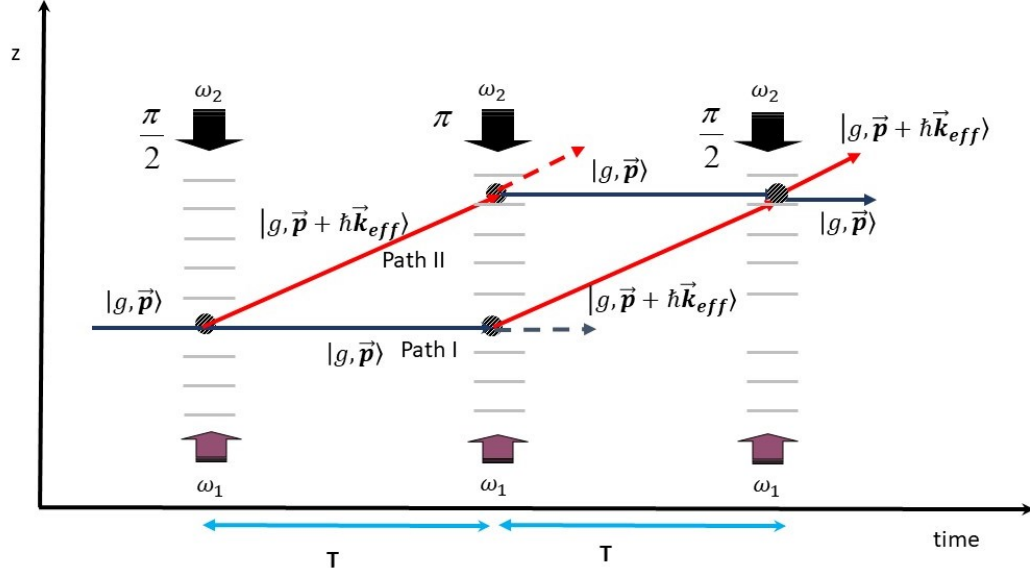


Figure 4.6: **Atom interferometer diagram depicting the atom's position.** The vertical axis is the position of the atom in the free fall trajectory of the atoms and the horizontal axis represent the time taken in the interferometric sequence.

ometer. The phase evolution can be decomposed into two components: the interaction between atoms and the Raman or Bragg laser field, and their free evolution during the intervals devoid of light pulses. Here we used Bragg pulses in the interferometer.

$$\Phi = \Delta\phi_{\text{int}} + \Delta\phi_{\text{evol}} \quad (4.12)$$

Let us discuss both the evolution separately.

4.3.1 Bragg pulse interaction in an atom interferometer

As illustrated in Figure 4.6, we will break down the specific terms that contribute to the phase shift during the transition of atoms between states. Referring to Table 2.1, we can disregard the terms that cancel out within our pulse sequence. Consequently, the primary term influencing the phase change will be ϕ_{eff} . Thus we can introduce the phase term introduced onto the wave function during the i -th pulse as:

$$\phi_i = \phi_{\text{eff}}(z(t_i), t_i) = \omega_{\text{eff}} t_i - k_{\text{eff}} z(t_i) + \phi_{\text{eff},0}(t_i) \quad (4.13)$$

where $i = A, B, C$. Assuming that the hyperfine transition energy is adjusted (using laser detuning to counteract the Doppler shift) such that $\delta_{eff} = 0$ and the light shift compensation is $\delta_{AC} = 0$, with all atoms initially in the state $|g, \vec{p}\rangle$. By applying equations 2.47 and 2.48, we can calculate the coefficients for the atomic states before, during, and after the three pulses.

$$c_{|g, \vec{p}\rangle}(t = t_0) = 1 \quad (4.14)$$

$$c_{|e, \vec{p} + \hbar \vec{k}_{eff}\rangle}(t = t_0) = 0 \quad (4.15)$$

$$c_{|g, \vec{p}\rangle}(t_A < t < t_B) = \frac{1}{\sqrt{2}} e^{-i\pi/2} \quad (4.16)$$

$$c_{|e, \vec{p} + \hbar \vec{k}_{eff}\rangle}(t_A < t < t_B) = \frac{1}{\sqrt{2}} i e^{-i(\pi/2 + \phi_A)} \quad (4.17)$$

$$c_{|g, \vec{p}\rangle}(t_B < t < t_C) = \frac{1}{\sqrt{2}} e^{-i(3\pi/2 + \phi_A - \phi'_B)} \quad (4.18)$$

$$c_{|e, \vec{p} + \hbar \vec{k}_{eff}\rangle}(t_B < t < t_C) = \frac{1}{\sqrt{2}} i e^{-i(3\pi/2 + \phi_B)} \quad (4.19)$$

$$c_{|g, \vec{p}\rangle}(t_C < t) = \frac{1}{2} e^{-i(2\pi + \phi_B - \phi'_C)} + \frac{1}{2} i e^{-i(2\pi + \phi_A - \phi'_B)} \quad (4.20)$$

$$c_{|e, \vec{p} + \hbar \vec{k}_{eff}\rangle}(t_C < t) = \frac{1}{2} e^{-i(2\pi + \phi_B)} + \frac{1}{2} i e^{-i(2\pi + \phi_A - \phi'_B + \phi_C)} \quad (4.21)$$

where ' denotes the contribution from 2nd path. Thus the probabilities after the final pulse in both the momentum states is written as:

$$P_g(t) = |c_{|g, \vec{p}\rangle}|^2 = \frac{1}{2} C (1 + \cos \Delta\phi_g) \quad (4.22)$$

$$P_e(t) = |c_{|e, \vec{p} + \hbar \vec{k}_{eff}\rangle}|^2 = \frac{1}{2} C (1 - \cos \Delta\phi_e) \quad (4.23)$$

where C is the contrast of the measurement and ,

$$\Delta\phi_g = (\phi_A - \phi_B) - (\phi'_B - \phi'_C) \quad (4.24)$$

$$\Delta\phi_e = (\phi_A - \phi_B + \phi_C) - \phi'_B \quad (4.25)$$

Gravity interaction

Assuming perfect control over the laser field phase offset and frequency, these equations can be simplified. For uniform gravitational acceleration, where $z(t_i) = v_0 t_i - \frac{1}{2} g t_i^2$, the laser field phase offset experienced by the atoms during the three pulses can be calculated as:

$$\phi_A = 0 \quad (4.26)$$

$$\phi_B = k_{eff} g \frac{T^2}{2} \quad (4.27)$$

$$\phi_C = k_{eff} g \frac{(2T)^2}{2}, \quad (4.28)$$

or, if there is an intentional phase offset $\Delta\phi_{offset}$ between pulses B and C,

$$\phi_C = k_{eff} g \frac{(2T)^2}{2} + \Delta\phi_{offset} \quad (4.29)$$

therefore,

$$\Delta\phi_{int} = \Delta\phi_g = \Delta\phi_e = \phi_A - 2\phi_B + \phi_C = k_{eff} g T^2 + \Delta\phi_{offset}, \quad (4.30)$$

or, considering the finite duration τ of the Bragg pulses and with T representing the time interval between pulses,

$$\phi_A - 2\phi_B + \phi_C = k_{eff} g T(T + 2\tau) + \Delta\phi_{offset}. \quad (4.31)$$

This results in a fundamental relation for determining the local gravitational acceleration g by measuring the population ratio at the output of an atom interferometer.

4.3.2 Free evolution between the pulses

Let us now derive the phase difference contributed from the free evolution between two pulses in an atom interferometer. This is formulated how the wavefunction evolves from $\Psi(z_A, t_A)$ to $\Psi(z_B, t_B)$ along a path between spacetime points A and B , defined by the positions z_A, z_B and times t_A, t_B with $t_A < t_B$ as mentioned in [77].

Thus, we used the solution of classical path where we considered the Lagrangian for a particle in a gravitational field. The equation states as:

$$S_{cl}(z_B t_B, z_A t_A) = \int_{t_A}^{t_B} [L(z, \dot{z})] dt \quad (4.32)$$

$$= \frac{m}{2} \frac{(z_B - z_A)^2}{t_B - t_A} - \frac{mg}{2} (z_B + z_A)(t_B - t_A) - \frac{mg^2}{24} (t_B - t_A)^3. \quad (4.33)$$

where,

$$\dot{z}(t) = \dot{z}_A - g(t_B - t_A) \quad (4.34)$$

$$z(t) = z_A + \dot{z}_A(t_B - t_A) - \frac{1}{2}g(t_B - t_A)^2 \quad (4.35)$$

which is solved by the principle of least action.

It has been demonstrated [77] that the phase evolution between spacetime points A and B can be expressed as

$$\Delta\phi_{A \rightarrow B} = \frac{S_{cl}(z_B t_B, z_A t_A)}{\hbar}. \quad (4.36)$$

This relationship is used to describe the phase shift due to free evolution along the two paths of our interferometer. We represent $z_B, z_{B'}$, and z_C using equations 4.34 and 4.35. By choosing our time and reference frames such that $t_A = 0$, $z_A = 0$, and $\dot{z}_A = 0$, and setting $(t_{B,B'} - t_A) = (t_C - t_{B,B'}) = T$, these expressions simplify to:

$$z_B = -\frac{1}{2}gT^2 \quad (4.37)$$

$$z_{B'} = -\frac{1}{2}gT^2 + \frac{\hbar k_{eff}}{m}T \quad (4.38)$$

$$z_C = -2gT^2 + \frac{\hbar k_{eff}}{m}T \quad (4.39)$$

We can now determine the phase difference caused by the free evolution of the wavepackets by splitting both interferometer paths into their two respective halves (AB, BC) and ($AB', B'C$) and inserting (4.33) and (4.36) into

$$\Delta\phi_{evol} = (\Delta\phi_{A \rightarrow B} + \Delta\phi_{B \rightarrow C}) - (\Delta\phi_{A \rightarrow B'} + \Delta\phi_{B' \rightarrow C}) \quad (4.40)$$

$$= \frac{m}{\hbar T} [z_B^2 - z_{B'}^2 - z_B z_A - z_C z_B + z_{B'} z_A + z_C z_{B'} - z_B g T^2 + z_{B'} g T^2] \quad (4.41)$$

$$= 0. \quad (4.42)$$

Thus, the free evolution in a uniform gravitational potential does not affect the interference observed at the output of the interferometer and

$$\Phi = \Delta\phi_{int}. \quad (4.43)$$

4.4 Mach-Zehnder Interferometer

In theory, the initial momentum state $|0\hbar k\rangle$ can be coupled to any momentum state $|2n\hbar k\rangle$ (where n is an integer) through n th-order Bragg diffraction. In our study, we specifically couple the momentum states $|0\hbar k\rangle$ and $|4\hbar k\rangle$ (with $k = \frac{2\pi}{\lambda}$ and $\lambda = 780$ nm, the wavelength of the laser). The momentum-space wave function of a condensate, initially in the state $|0\hbar k\rangle$, when irradiated with Bragg diffraction beams, oscillates between these two coupled momentum states similar to a two-level system. The effective oscillation frequency is given by $\Omega_{\text{eff}} = \frac{\Omega_e \Omega_g}{2\Delta}$, where Ω_e and Ω_g are the resonant Rabi frequencies of the Bragg beams, and Δ represents the detuning of the beams from the optical transition. By tuning the intensity, detuning, and duration of the Bragg pulse, we can transfer a specified fraction of atoms to the $|4\hbar k\rangle$ momentum state.

The closed two-level system influenced by the Bragg beams can be conveniently modeled as a fictitious spin- $\frac{1}{2}$ system, where $|g\rangle$ represents $|0\hbar k\rangle$ and $|e\rangle$ stands for $|4\hbar k\rangle$. A $\frac{\pi}{2}$ or π pulse transfers half or all of the atoms from $|g\rangle$ to $|e\rangle$. Specifically,

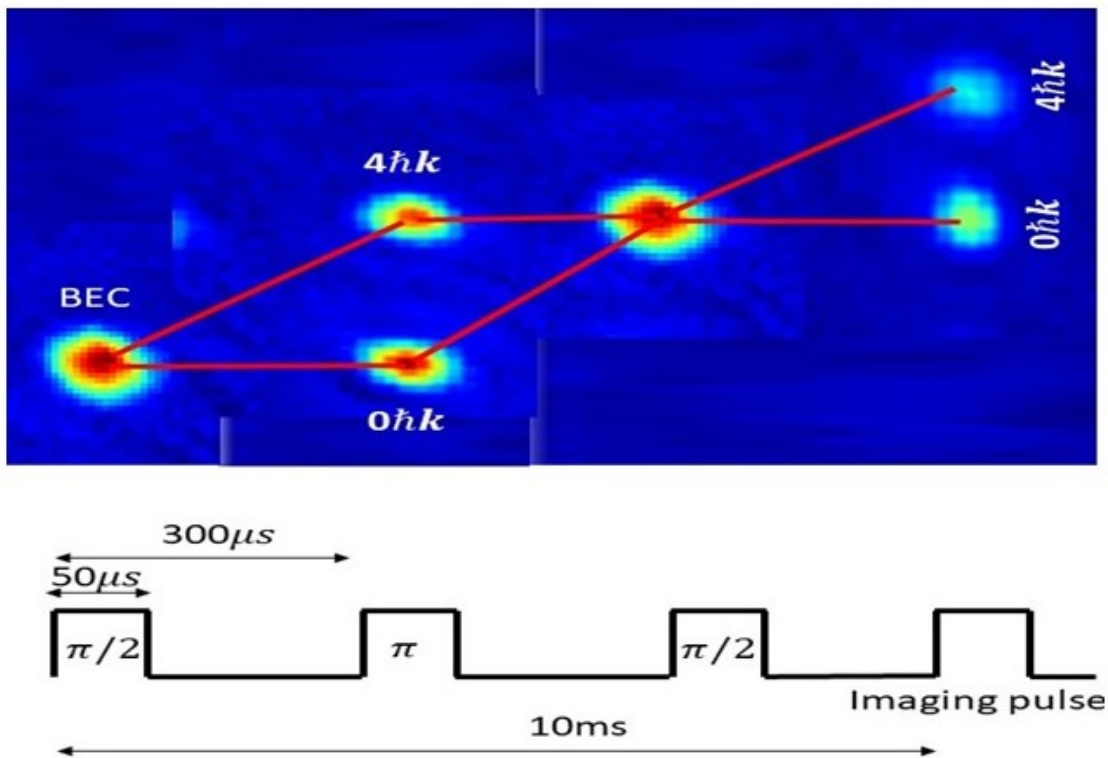


Figure 4.7: **Schematic of the Mach-Zehnder Bragg Interferometer Experiment.** The following pulse sequence illustrates the consecutive Bragg pulses. In this sequence, $\pi/2 = 50 \mu\text{s}$, $\pi = 100 \mu\text{s}$, and the interferogram time is $300 \mu\text{s}$.

under a $\frac{\pi}{2}$ pulse, the state vector transforms according to $|g\rangle \rightarrow (|g\rangle - e^{-i\phi}|e\rangle)/\sqrt{2}$ and $|e\rangle \rightarrow (e^{+i\phi}|g\rangle + |e\rangle)/\sqrt{2}$. Here, ϕ is the phase of the moving standing wave at the center of the initial atomic wavepacket $|g\rangle$ during the Bragg pulse. Changes in ϕ are measured relative to the phase of the resonant, moving standing wave. With successive applications of this transformation, a π pulse results in $|g\rangle \rightarrow 2e^{-i\phi}|e\rangle$ and $|e\rangle \rightarrow e^{+i\phi}|g\rangle$. Thus, a $\frac{\pi}{2}$ and π pulse can be used as an ideal beam splitter and mirror for the condensate.

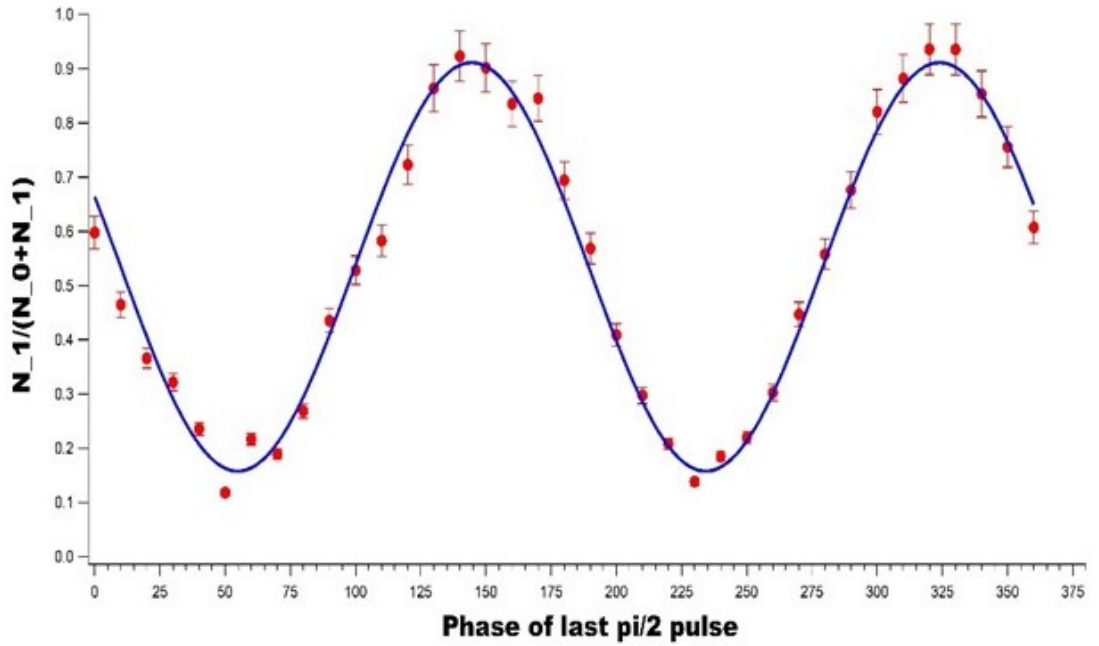


Figure 4.8: **Population oscillation of the condensate.** Oscillations in the population of diffracted order of the condensate in the $|4\hbar k\rangle$ momentum state as a function of the phase shift ϕ of the last Bragg pulse. The interferogram time between the centers of successive Bragg pulses is $\Delta T = 300 \mu\text{s}$.

We generate a Bose-Einstein condensate (BEC) of rubidium atoms, typically around 150 nK, utilizing a hybrid optical dipole trap setup. Approximately every 16 minutes, we produce a BEC comprising roughly 10^5 atoms predominantly in the $5S_{1/2} F = 1, m_F = -1$ state. Following the condensate's creation, we release it by abruptly switching off the trap mechanism, allowing for a 2 ms delay to mitigate the mean-field-driven explosive expansion. Subsequently, we implement a Bragg interferometer pulse sequence. After a 10 ms period of free evolution to enable adequate spatial separation

between the $|g\rangle$ and $|e\rangle$ components, we capture an absorption image of the resulting condensate. This imaging process yields highly precise and clear signals, as the interferometer's operation is reflected in the probability distribution of observing atoms in two distinct spatial regions. Figures 4.7 and 4.8 depict the Mach-Zehnder interferometer and the population oscillation resulting from the first-order Bragg diffraction of the condensate, respectively. The population oscillation can be fitted by 2.53 i.e.

$$P_e(t) = \sin^2 \left[\frac{\Omega_{\text{eff}} \cdot \tau}{2} \right] = \frac{1}{2} [1 - \cos(\Omega_{\text{eff}} \cdot \tau)]. \quad (4.44)$$

4.5 Summary

This chapter provides a detailed explanation of Bragg diffraction and Bragg spectroscopy in Bose-Einstein Condensates (BEC). It explores how BECs interact with standing light waves, leading to Bragg diffraction, which is crucial for understanding atomic momentum transfer and manipulating BECs in experimental setups. The chapter also delves into Bragg spectroscopy, a technique used to probe the excitation spectrum of BECs and extract key information about their properties. Additionally, it introduces an atom interferometer designed for BECs, focusing on the measurement of time-of-flight for a 10 ms duration, which is essential for precision measurements in quantum experiments.

Chapter 5

Atomic Gravimeter

This chapter has been reported in :

Comparative Analysis of Phase Noise for Different Configurations of Bragg Lattice for an Atomic Gravimeter with Bose-Einstein Condensate; **Pranab Dutta**, S. Sagar Maurya, Korak Biswas, Kushal Patel, Umakant D. Rapol, *AIP Advances*, **14**, 015352 (2024) [105]

We perform a comparative study of the phase noise induced in the lasers used for Bragg diffraction in a Bose-Einstein condensate based quantum gravimeter where the Bragg beams are generated using two different configurations. In one of the configurations, the Bragg beams that form the moving optical lattice are generated using two different acousto-optic modulators. In the second configuration, the Bragg beams are generated using a single acousto-optic modulator carrying two phase locked frequencies. The second configuration shows a suppression of phase noise by a factor of 4.7 times in the frequency band upto 10 kHz, the primary source of noise, which is the background acoustic noise picked up by optical components and the optical table. We report a short-term sensitivity of $1360 \mu\text{Gal}/\sqrt{\text{Hz}}$ ($1\text{Gal} = 10^{-2} \text{m/s}$) and upon integration over 200 seconds, achieve a resolution of $99.7 \mu\text{Gal}$ for an interferometric duration of 10 ms [105].

5.1 Introduction

Atom Interferometers (AI) have shown to be a promising tool in precision measurement over an Optical Interferometer(OI). Theoretically, the atom interferometer's sensitivity is about ten orders of magnitude larger than the optical interferometer [106] due to the rest-mass of the interfering atoms compared to photons. In the last three decades, the source of atoms for an AI moved on from a beam of hot atoms to a cloud of cold atoms [107–109]for increased sensitivity. At present, AI using cold atoms has been successfully demonstrated for utilization in gravimetry [110–112], magnetometry [113,114], rotation sensing [18,115], inertial navigation [116,117], measurement of fundamental constants [118,119] and tests of general relativity [120,121]. Over the last two decades, significant advancements have been made in the practical application of these AI based quantum sensors [7,122,123]

AI, based on cold atoms is limited by the coherence length of atoms leading to degradation of fringe contrast in the interference signal [124] which finally decreases the sensitivity of the system. AI based on Bose-Einstein Condensate (BEC) have been shown to lead to higher contrast owing to the larger brightness and coherence length of BECs. The BEC's high number density is a concern for precision measurement as it introduces interaction-induced dephasing due to mean-field energy [125]. This can be avoided by providing sufficient time of flight before the interferometric pulse sequence is initiated, whereby the mean field interaction becomes negligible [126]. For the measurement of absolute gravity, BEC based atom interferometers have been shown to be as accurate as conventional cold atom based interferometers. Atom chip based BEC AI even can potentially reduce the electronic and optical complexity [19] and have shown accuracies below sub- μGal ($1\text{Gal} = 10^{-2}\text{m/s}^2$) [19]. There have been continuous efforts worldwide to reduce its size, weight and power for transportability on ground as well as for deployment in space.

The majority of AI systems based on Bose-Einstein condensates (BECs) necessitate intricate optical configurations for system realization. These configurations introduce phase noise, which can be mitigated through the implementation of passive and active isolation systems [19], or via the utilization of optical phase-locking loop techniques

(OPLL) [127]. Here, we report the implementation of two configurations for generating Bragg beams on a BEC based AI to measure the gravity using ^{87}Rb [19, 128, 129] and made a comparative analysis of the phase noise reduction. Conventionally two separate AOMs are used to realize the Bragg beams required for AI [127]. In this work we achieved a significant reduction of phase noise using a single AOM [49] which reduces the optical complexity in comparison to the conventional method. By utilizing this approach, the Bragg beams and its associated pulses, carrying both frequencies, shared the same optical path, including mirrors, and optics. As a result, it mitigated the phase noise by significantly reducing the common mode. This reduction in common-mode phase noise proved to be highly effective, enabling us to extend the interferometric time to more than 10 ms, a task that was challenging with the two distinct AOM configurations in our setup. Furthermore, we characterized this reduction of noise by carrying out detailed study of the phase noise in both the configurations [127].

5.2 Quantum Gravimeter

5.2.1 Measurement Principle

The operation of an atom interferometer relies on spatial manipulation of the atomic wavepacket to achieve the interferometric fringe signal. This manipulation is usually achieved using laser light arranged in different configurations. Some of the commonly used techniques are Bragg diffraction, Bloch oscillations and Raman diffraction [130, 131]. In an atom interferometer the atomic wavepacket is to be split and recombined using optical 'beam splitters' and 'optical mirrors' that change the momentum of the atomic wavepacket. In our gravimeter, we utilize the technique of Bragg diffraction, which is extensively described in references [21, 132]. This technique involves coupling two momentum states, namely p_0 and $p_0 + 2n\hbar k$ (where p_0 is the initial momentum of BEC, k is the wave number of light and n is the order of Bragg transition) through a two-photon stimulated process [133]. We perform the AI in Mach-Zehnder ($\pi/2 - \pi - \pi/2$) configuration [21] where $\pi/2$ pulse acts as beam splitter and π pulse is used as mirrors [48]. A brief experimental procedure is shown in Figure 5.1 based on references [128, 129, 134]. In order to enable atomic gravimetry, one can introduce

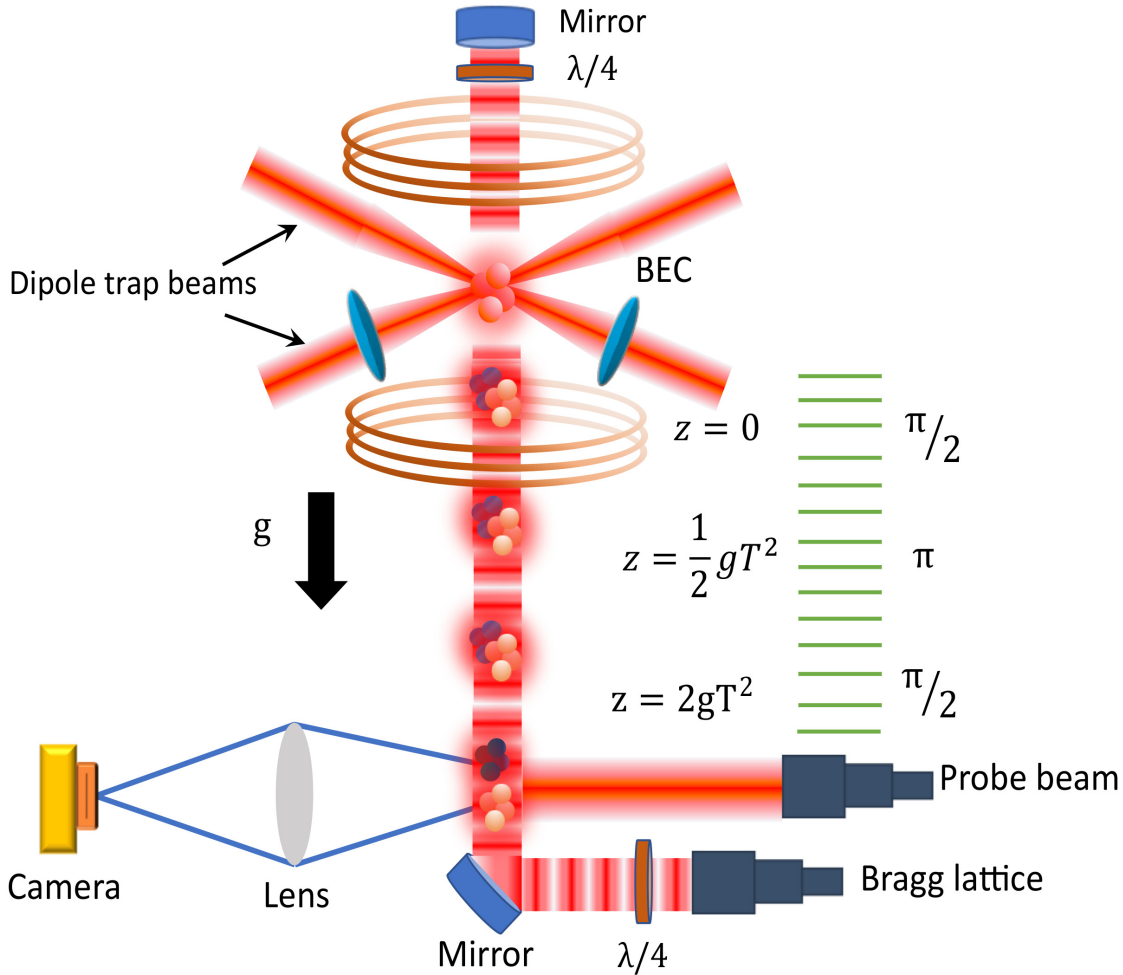


Figure 5.1: Schematic diagram of BEC based atom interferometer for gravimetry and its space time trajectories. The diagram represents the formation of BEC at the center of the magneto-optical trap which is realized in a hybrid trap using a dipole trap and the magnetic field. The BEC is allowed to free fall in the absence of the trap potential and allowed to evolve under the interferometric pulses. The green dashed lines represent the three consecutive interferometric pulses for the realization of Mach-Zehnder interferometer with BEC. Figure adapted from our previous work [7]. Reproduced with permission from J Indian Inst Sci 103, 609–632 (2023), Springer Nature.

two counter-propagating or co-propagating beams that create a moving optical lattice i.e. Bragg beams which can be realised with beams of variable frequency components f and $f + \delta f$. In the absence of any external force on atoms, the relative acceleration between the moving optical lattice and atoms remains uniform, the paths followed by the atoms during the interferometer will be identical, resulting in a zero phase contribution. Consequently, in the presence gravitational force on atoms, the overall phase shift will be proportional to the uniform acceleration generated by the interaction between light and atoms, as described in reference as [129]:

$$\Phi = n(\phi_1 - 2\phi_2 + \phi_3) = 2n\mathbf{k} \cdot \mathbf{g}T^2 \quad (5.1)$$

Here, the optical phases ϕ_1, ϕ_2 and ϕ_3 represents the interactions of atoms with Bragg pulses, n corresponds to the Bragg order, and T signifies the interferometric time of the atom interferometer (AI). Scanning the phase of final $\pi/2$ pulse, we observe oscillation in the population of both momentum order, and the resulting signal exhibits to:

$$P = N(1 + C \cos(\Phi))/2 \quad (5.2)$$

where N is the population of atoms and C is the contrast of signal. The fundamental concept of measuring gravity is to balance the phase difference imparted to the atoms by gravitational acceleration and the Bragg AI pulses. As freely falling atoms experience a time-dependent Doppler shift with respect to the Bragg transition, the optical lattice is accelerated by adjusting the frequency difference in the lattice beam. The overall phase shift can be obtained by scanning the lattice acceleration around the local gravity which becomes as $\Phi = n(2\mathbf{k} \cdot \mathbf{g}T^2 - 2\pi\alpha T^2)$ where α is the sweep rate (also considered as frequency chirp) of lattice. To determine the value of g , the value of α (say, α_0) will balance the gravity and overall phase shift Φ will be zero, thus providing $\alpha_0 = \frac{1}{\pi}(\mathbf{k} \cdot \mathbf{g})$. To determine the value of α_0 , one has to observe the interferometric signal for at least three different interferogram time(T), and all those interferometric signal have a common minima at α_0 .

5.2.2 Noise Model of an Interferometer due to its optical path

A typical or conventional atom interferometer using Bragg-based principles is constructed with a heterodyne optical setup [135]. This configuration involves splitting a single beam into two separate paths and directing them through two acousto-optic modulators (AOMs) with frequencies f_1 and f_2 respectively. The resulting heterodyne interferometric signal is detected and can be described by the equation:

$$S(t) = A [1 + C \cos(2\pi f_c t + \phi_n(t) + \phi_0)] \quad (5.3)$$

where A represents the amplitude of the DC component, C is the visibility or contrast, $f_c = f_1 - f_2$ denotes the heterodyne frequency, and ϕ_0 represents the average phase. The term $\phi_n(t)$ represents the phase noise induced by acoustic, optical, and electronic components. To extract the phase noise, one utilizes the orthogonal demodulation technique. This technique involves mixing $S(t)$ with a low-noise reference frequency using a lock-in amplifier. The lock-in amplifier mixes $S(t)$ with $\sin(2\pi f_c t)$ and $\cos(2\pi f_c t)$, followed by a low-pass filter to eliminate undesirable higher frequencies. Consequently, Equation 5.3 can be modified as proposed in [136] to include the respective noise model:

$$S(t) = A[1 + n_m(t)][1 + C \cos(2\pi f_c t + n_p(t) + \phi_0)] + n_a(t) \quad (5.4)$$

where $\phi_n(t)$ is now represented as $n_p(t)$ to account for phase noise originating from the laser source, AOM driver, and seismic vibrations. Additionally, $n_a(t)$ accounts for additive noise, including amplified spontaneous emission noise, quantization noise, and circuit noise. Finally, $n_m(t)$ represents multiplicative noise, which includes the amplitude noise of the optical pulse caused by the AOM driver and the relative intensity noise (RIN) of the laser. Our particular focus was on the noise induced by the AOM and optical elements resulting from acoustic vibrations.

5.2.3 Sensitivity Function

The sensitivity function gives the information regarding the atom interferometer phase shift Φ due to infinitesimal laser phase shift $\delta\phi$ in the Bragg pulses and thus the population measured at the interferometric outputs. The sensitivity function $g_\phi(t)$ is defined

as [137]:

$$g_\phi(t) = \lim_{\delta\phi \rightarrow 0} \frac{\delta\Phi(\delta\phi, t)}{\delta\phi} = \frac{2}{\sin \Phi} \lim_{\delta\phi \rightarrow 0} \frac{\delta P(\Phi, \delta\phi, t)}{\delta\phi} \quad (5.5)$$

The above relation can be replicated for an interferometer both for beam splitters and mirrors as follows:

$$g_\phi(t) = \sin \left(\int_{t_0}^t \Omega_R(t') dt' \right) \quad (5.6)$$

where $\Omega_R(t)$ is the Rabi frequency during the light-atom interaction in the interferomet-

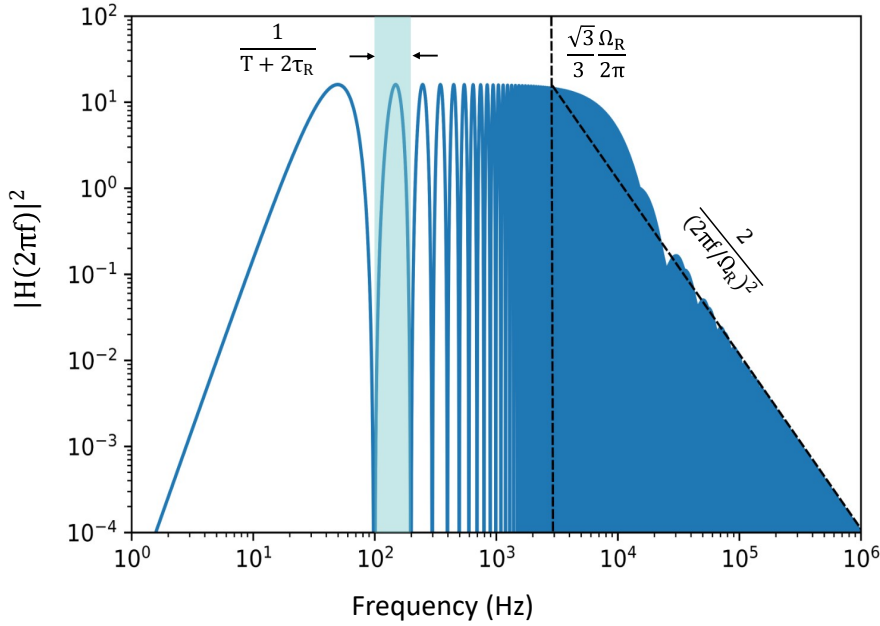


Figure 5.2: Transfer function $|H(2\pi f)|^2$ for a Mach-Zehnder sequence $\pi/2 - \pi - \pi/2$ with a Rabi frequency of $2\pi \times 5$ kHz for an interferometric time of 10 ms. $\frac{n}{T+2\tau_R}$ represents the frequencies where the sensitivity diminishes, where n is an integer and $\frac{\sqrt{3}\Omega_R}{6\pi}$ corresponds to the cutoff frequency for a finite duration of Bragg pulses.

ric sequence. The complete value of $g_\phi(t)$ depends on the scheme one uses to perform the interferometer. For a Mach-Zehnder interferometer with three consecutive pulses of $\pi/2$ and π , we consider the time origin at the middle of the second Bragg pulse. Thus the sensitivity function can thus be read as for one half of the sequence where τ_R is the

duration of the bragg pulse seperated by interferometric time T:

$$g_{\phi}(t) = \begin{cases} \sin(\Omega_R t), & 0 < t < \tau_R \\ 1, & \tau_R < t < T + \tau_R \\ -\sin(\Omega_R(T - t)), & T + \tau_R < t < T + 2\tau_R \end{cases} \quad (5.7)$$

Thus, the sensitivity function is used to determine the interferometric phase shift Φ for an arbitrary Bragg phase noise $\phi(t)$ as:

$$\Phi = \int_{-\infty}^{+\infty} g_{\phi}(t) d\phi(t) = \int_{-\infty}^{+\infty} g_{\phi}(t) \frac{d\phi(t)}{dt} dt \quad (5.8)$$

We establish the interferometer's transfer function in the Fourier domain $H(\omega) = H(2\pi f) = \omega G(\omega)$ where $G(\omega) = \int_{-\infty}^{+\infty} e^{-i\omega t} g_{\phi}(t) dt$ is the fourier transform of the sensitivity function defined as:

$$G(\omega) = \frac{4i\Omega_R}{\omega^2 - \Omega_R^2} \sin\left\{\frac{\omega(T + 2\tau_R)}{2}\right\} \times \left[\cos\left\{\frac{\omega(T + 2\tau_R)}{2}\right\} + \frac{\Omega_R}{\omega} \sin\left(\frac{\omega T}{2}\right) \right] \quad (5.9)$$

To assess how the laser phase noise affects the interferometer sensitivity, we thus defined the rms standard deviation of the phase noise in the interferometer as:

$$(\sigma_{\Phi})^2 = \int_0^{+\infty} |H(\omega)|^2 S_{\Phi}(\omega) d\omega \quad (5.10)$$

where, $S_{\phi}(\omega)$ represents the power spectral density of phase of the Bragg phase.

Hence, the transfer function was plotted in Figure 5.2 to analyze its behavior in relation to frequency. The transfer function exhibits oscillatory patterns, providing insights into the diminishing amplitude of repetitive regions at frequencies given by $f = n/(T + 2\tau_R)$, where n is an integer. This behavior indicates that the interferometer functions acts as a low-pass filter, with a cutoff frequency defined as $f = \sqrt{3}\Omega_R/6\pi$. As the frequency increases, the transfer function exhibits a trend proportional to $2/(2\pi f/\Omega_R)^2$, leading to a decrease in interferometric sensitivity.

5.3 Experimental Details

We create a BEC of ^{87}Rb consisting of 5×10^4 atoms every 15 seconds in a dipole trap. The temperature of the residual thermal component of the BEC is measured to be less than 200 nK. The experimental setup is almost the same as in this reference [138]. After turning off the dipole trap, we provide 2 ms time of flight to reduce BEC's mean-field effect on AI. The laser used for realizing the optical lattice is locked to the $5^2\text{S}_{1/2}, F = 2 \rightarrow 5^2\text{P}_{3/2}, F' = 2$, D2 transition at 780 nm. Since the BEC is prepared in the $5^2\text{S}_{1/2}, F = 1, m_F = -1$ state, the laser is 6.8 GHz red-detuned from the atoms' accessible transition to suppress spontaneous emission. Now, for operation as a gravimeter, we have introduced two different methods where a vertical, linearly polarized light beam travelling through two different Acousto-Optic Modulator (AOM) (ATM-801A2) or a single Acousto-Optic Modulator (AOM), which is driven by Arbitrary Function Generators (AFG) (AFG3032C) phase-locked by Rubidium frequency standard (FS725) as shown in the Figure 5.3 (a) and 5.3 (b). By employing the AFG to drive the AOM, we gain precise control over various parameters such as frequency, sweep rate in frequency, and the phase of the lattice beam. To drive the Bragg transition in ^{87}Rb , the frequency difference in lattice beam should be $\delta f = 4n\omega_R$, where n is the order of Bragg transition and ω_R is recoil frequency, and frequency difference is about 15 kHz in our experimental setup for first-order Bragg transition. But when the atoms are freely falling under gravity, the Bragg transition condition gets modified because atoms feel a time-dependent Doppler shift $\delta_d(t) = 2\pi\alpha_0 t$, where $\alpha_0 = (\frac{1}{\pi})(\mathbf{k} \cdot \mathbf{g})$ is a frequency chirp. The resonance condition for the Bragg transition is then transformed in laboratory frame as $\delta f = 4n\omega_R + 2(\mathbf{k} \cdot \mathbf{g})t$ [129]. To compensate for this Doppler shift, we apply a 25.078 MHz/s sweep rate (determined by the approximate theoretical value of g in Pune) in one of the lattice beams to keep the atoms on resonance for the Bragg transition. For generating the AI pulses ($\pi/2 - \pi - \pi/2$) in the Mach-Zehnder configuration, we have used square pulses with a pulse duration of 50 μs for $\pi/2$ pulses and 100 μs for π pulse to drive the first-order Bragg transition, and a time sequence has shown in Figure 5.1 with a $1/e^2$ beam diameter of about 2.5 mm. The typical power in each beam near the interrogation site is about 1 mW. The effective Rabi frequency

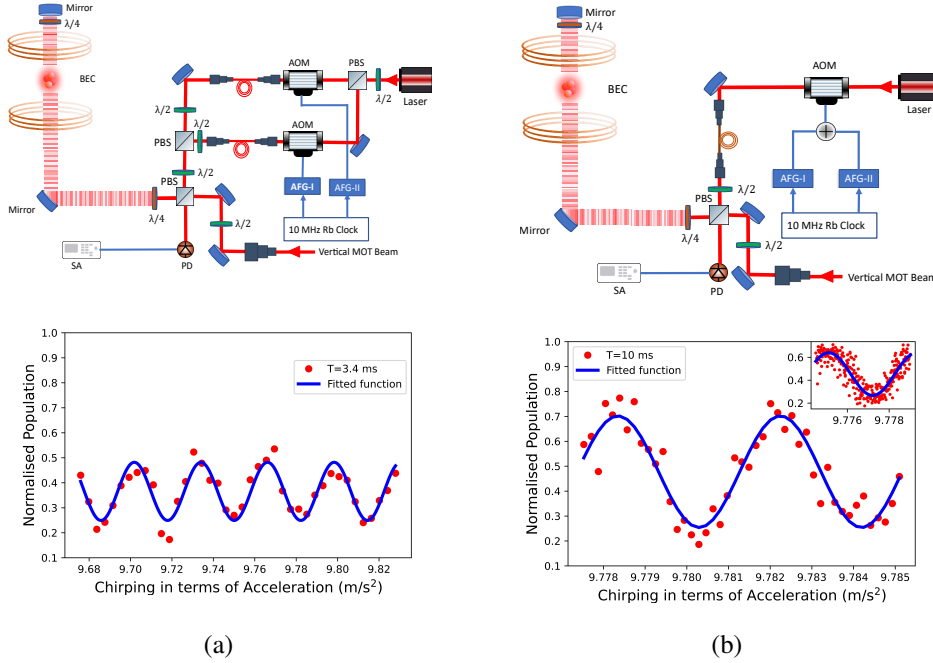


Figure 5.3: Schematic diagram of

generation of Bragg beams and interferometric signal for two different configurations. **(a)** Top figure depicts the block diagram of generation of Bragg pulses using two different AOMs driven by AFGs which are phase locked using Rubidium atomic clock. The laser is locked to the Rubidium transition line which is not shown in the diagram. PD: photodiode, SA: spectrum analyser, AFG: arbitrary function generator. Bottom figure shows the population oscillation of first order momentum state versus sweep rate in terms of acceleration for interferometer time $T = 3.4$ ms. **(b)** Top figure depicts the block diagram of generation of Bragg pulses using single AOM driven by AFG which are phase locked. Bottom figure which is adapted from our previous work [7] shows the population oscillation of first order momentum state versus sweep rate in terms of acceleration for interferometer time $T = 10$ ms for single AOM configuration. Reproduced with permission from J Indian Inst Sci 103, 609–632 (2023), Springer Nature. Inset: Precise scanning of sweep rate along with the interferometric signal.

corresponding to this beam intensity is calculated as $\Omega_{\text{eff}} = \frac{\Omega_1 \Omega_2}{2\Delta} \simeq 2\pi \times 5$ kHz where Ω_1 and Ω_2 represent the resonant Rabi frequencies of two Bragg beams, and Δ denotes the detuning of the beams from the optical transition.

Figure 5.3 represents the interference fringes obtained from two different configurations. Figure 5.3 (a) interference signal is the first configuration involved the utilization of two co-propagating laser beams diffracted by AOMs operating at 80 MHz and 80.015 MHz to generate an optical lattice as illustrated in reference [127] without any active feedback locking technique. The interference pattern exhibited an interferometric oscillation with low contrast, resulting in a transfer efficiency of approximately $\sim 25\%$ for an interferometric time of $T = 3.4$ ms. This reduction in contrast or visibility was attributed to phase noise induced by acoustic and sub-acoustic vibrations coupled to the atomic system.

In the second configuration, a single AOM was employed, and dual frequencies of 80 MHz and 80.015 MHz were introduced from two phase-locked AFGs, as illustrated in Figure 5.3 (b). Notably, this configuration demonstrated an improvement in contrast or visibility compared to the previous method. Thus the graph depicts the population oscillation of $p = 2\hbar k$ as a function of sweep rate in terms of acceleration, exhibiting a transfer efficiency of approximately $\sim 50\%$ for an interferometric time of $T = 10$ ms. The inset figure provides a detailed scan in relation to the sweep rate.

5.4 Results and discussion

5.4.1 Phase Noise for different configuration

With a interferogram time of approximately $2T = 20$ ms our interferometer is sensitive to fast noise contribution Φ_{noise} down to 50 Hz. It is important to note that due to geometric limitations in our system, we were unable to extend the interferometric experiments beyond a 40 ms time of flight. The principal source of noise in the measurement is the phase noise of the laser which interacts with the atoms. This laser phase originates from laser source and from the vibrations that shift the phase fronts of the two co-propagating laser beams. Since in our case we use Bragg beams which is originated from a single laser source due to which the contribution due to it is less compared to

acoustic vibrations.

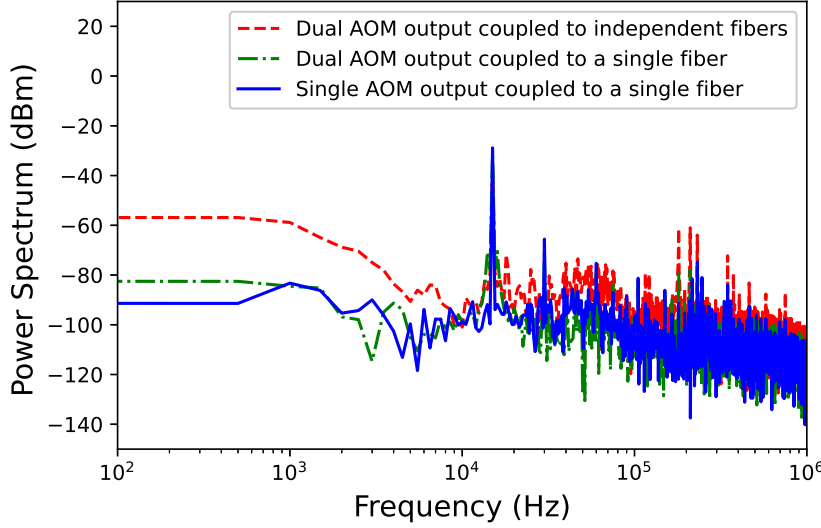


Figure 5.4: The power spectrum of the Bragg beams is examined for various configurations. In this analysis, the dashed red line represents the configuration involving two co-propagating laser beams diffracted from separate AOMs as shown in Figure 5.3 (a), the dot-dashed green line represents the configuration of Bragg beams diffracted from separate AOMs and coupled into a single fiber to reduce the differential phase noise and the solid blue line corresponds to the configuration utilizing a single AOM as shown in the Figure 5.3(b), with a frequency resolution of 500 Hz.

To evaluate the contribution of different configuration we set the frequency difference between the lattice beam at 15 kHz, the first order Bragg resonance for ^{87}Rb . The beat signal is logged at a sampling rate of 2.5 Giga samples per second for 2 ms with a record length of 5 million points. A fourier transform of the logged data is converted into the power spectrum shown in Figure 5.4. The dashed red line shows the power spectrum of configuration, as depicted in Figure 5.3 (a), which exhibits power above -80 dBm for frequencies below 10 kHz well above the single AOM configuration as shown in Figure 5.3 (b) which is depicted in solid blue line. The power spectrum analysis was conducted with a frequency resolution of 500 Hz. We also compared the beat signal generated by two AOMs and coupled to a single fiber to reduce the differential phase noise which is represented as the dot-dashed green line.

Thus, the initial experimental setup, depicted in Figure 5.3 (a), resulted in lower

interferometric signal due to the presence of phase noise induced by vibrations, which resulted in a constraint on the interferometric time due to loss of contrast. And, remarkably, Figure 5.3 (b) demonstrates a notable enhancement in both contrast and interferometric signal when we transitioned to the configuration utilizing a single AOM.

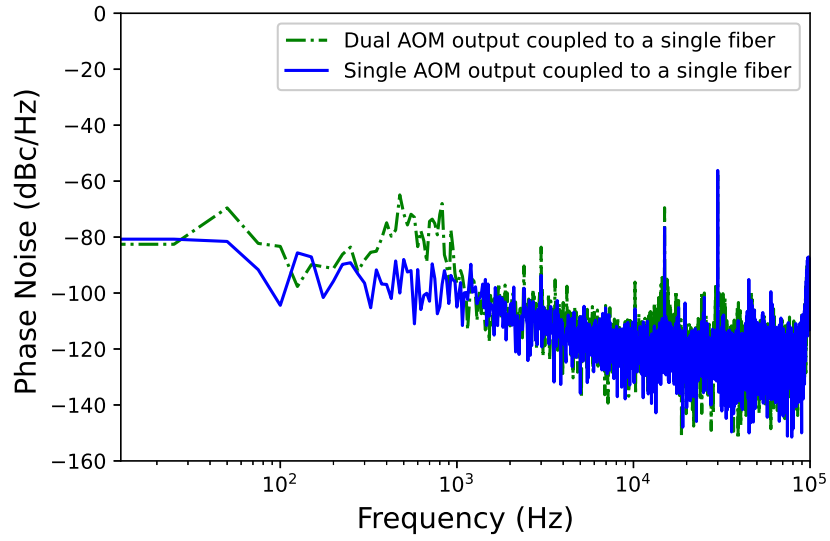


Figure 5.5: Phase Noise spectrum of the Bragg beams for single AOM configuration and dual AOM configuration coupled to a single fiber with 25 Hz resolution bandwidth.

We had also presented the phase noise spectrum for single AOM configuration and double AOM output coupled to a single fiber with a resolution bandwidth of 25 Hz. Notably, the single AOM configuration, represented by the blue line in Figure 5.5, achieves a significant suppression of residual phase noise by two orders of magnitude around 800 Hz. The calculated integrated phase noise in the Bragg pulse within the frequency range upto 10 kHz from Equation 5.10 for single AOM configuration, measures 10 mrad/shot, while for the dual AOM configuration coupled to a single fiber amounts to 47 mrad/shot.

5.4.2 Stability of the gravity measurement

To justify the resolution of the determined gravity value we performed the integration of the stability of the experiment. The AI interferometer is operated for about 2 hours with a pulse separation time of $T = 10$ ms for cycle time of $T_{\text{cycle}} = 17.98$ s. Figure 5.6

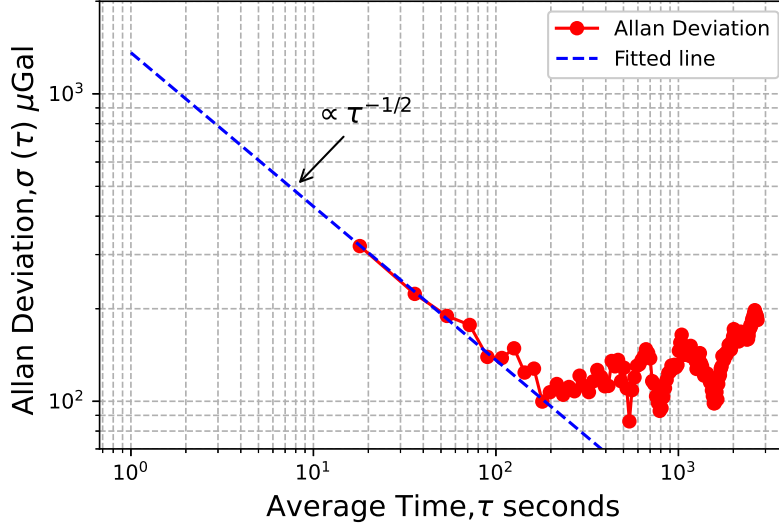


Figure 5.6: Allan deviation of the gravity measurements for interferometric time $T = 10$ ms. The dashed line corresponds to a short-term sensitivity of $1360 \mu\text{Gal}/\sqrt{\text{Hz}}$ for 1 second.

depicts the time series data in the form of Allan deviation of the population of atom in first order. The phase noise for the atomic interferometer with the better configuration is calculated using an Allan deviation. This which is derived as the square root of the Allan variance,

$$\sigma_y^2(\tau) = \frac{1}{2(M-1)} \sum_{i=1}^{M-1} (y_{i+1} - y_i)^2 \quad (5.11)$$

for a collections of M mean data points y_i , acquired at average interval τ . For this analysis, the data points corresponds to the measured acceleration due to gravity and the averaging time is expressed in units of runs that corresponds to the 17.9 s duty cycle of the experiment. Thus Allan deviation is a standard tool for assessing the temporal characteristics of noise in precision measurements. Hence, the Allan deviation serves as a common tool for evaluating the temporal properties of noise in precise measurements.

The measured short-term sensitivity of ultracold atom interferometer is estimated to be $1360 \mu\text{Gal}/\sqrt{\text{Hz}}$ which is extrapolated to 1 second according to the white noise behaviour as it scales as $\tau^{-1/2}$ where τ is the average time of operation. Thus we report

a resolution of $99.7 \mu\text{Gal}$ for an integration time of 200 seconds.

For the given interferometric time of $T=10$ ms, we have estimated the intrinsic sensitivity limit of the interferometer as [139]:

$$(\Delta g/g)_{\text{limit}} = \sigma_{\text{qpn}} \cdot \sigma_g = \frac{1}{C\sqrt{N}gk_{\text{eff}}T^2} \quad (5.12)$$

where $(\Delta g/g)_{\text{limit}}$ is the sensitivity of the system, σ_{qpn} is the quantum projection noise, σ_g is the scaling factor of the interferometer to changes in g and $k_{\text{eff}} = 2k$. The calculated intrinsic sensitivity limit for $T = 10$ ms is obtained to be around 56.7×10^{-8} for 50% contrast with 5×10^4 atoms.

5.5 Conclusion

In this study, we conducted a comparative analysis of two different techniques employed in atom interferometry (AI) for measuring local gravitational acceleration. Our approach involved utilizing a Mach-Zehnder matter wave interferometer, where Bragg diffraction of ^{87}Rb atoms in the Bose-Einstein condensate (BEC) state was employed. By implementing the one AOM configuration instead of the conventional method, we successfully reduced the phase noise in our system. As a result, we were able to extract the fringe visibility or contrast for the atom interferometer. The sensitivity of our system was determined to be $99.7 \mu\text{Gal}$, at an integration time of 200 seconds interval, with an interferometric time of 10 ms. Furthermore, we demonstrated that the conventional method, which involves splitting the beam and passing it through two AOMs coupled into a single fiber for noise cancellation, exhibited higher integrated phase noise compared to the single AOM configuration. In summary, our findings highlight the efficacy of employing a one AOM configuration to reduce phase noise, improve fringe visibility, and enhance the overall performance of the atom interferometer system for measuring local gravitational acceleration.

Chapter 6

Atom based rotation sensor

Some of the results of this chapter has been published in:

A Decade of Advancement of Quantum Sensing and Metrology in India Using Cold Atoms and Ions. J Indian Inst Sci; **Pranab Dutta**, S. Sagar Maurya, Kushal Patel, Korak Biswas, Umakant D. Rapol, et al. *J Indian Inst Sci*, **103**, 609–632 (2023) [56]

6.1 Sagnac Theory

In 1913, Georges Sagnac conducted an experimental demonstration illustrating that when light originating from a coherent source underwent division and recombination within a defined spatial enclosure, the resulting interference pattern experienced a phase alteration upon rotation of the entire apparatus [140]. This observed phase variation was directly related to the angular velocity, represented as $\vec{\Omega}$, giving rise to what is now widely recognized as the Sagnac effect. Within a Mach-Zehnder interferometer (MZI), such phase modulation accumulates along the two distinct interferometric paths. Furthermore, for an MZI encompassing a non-zero spatial area represented by \vec{A} , the discrepancy in phase is likewise contingent upon this enclosed region. Consequently, the larger the spatial expanse of the interferometer, the greater the sensitivity of the phase to rotational motion. This discrepancy in phase between the two paths is termed the Sagnac phase shift, its magnitude dictated by the rate of rotation according to the

ensuing expression:

$$\Delta\Phi_{\Omega} = \frac{1}{\hbar c^2} \oint_{\Gamma_0} (\vec{\Omega} \times \vec{r}) \cdot \vec{E} d\mathbf{r} = \frac{2E}{\hbar c^2} \vec{A} \cdot \vec{\Omega} \quad (6.1)$$

The symbol \vec{E} denotes the rest mass energy of the particles utilized in interferometry, while \vec{A} represents the physical area encompassed by the interferometer. Primarily, the device sensitive to this phase discrepancy functions as a gyroscope. This characterization of the Sagnac phase shift has been established in the context of matter-wave experiments, such as electron interferometry, as referenced in [141] and [142]. Similarly, the relationship between the Sagnac phase and the variables \vec{A} and $\vec{\Omega}$ holds true for optical interferometers, as noted in [143].

6.1.1 Employing a path integral approach to solve the Sagnac interferometer configuration

Utilizing the Feynman path integral method proves valuable in calculating the phase alteration during the propagation of atoms within the interferometer. Storey and Cohen-Tannoudji [144] conducted a thorough examination of interferometer setups, including ours, employing a path integral analysis. They also provide guidelines for managing interactions with light pulses. In classical mechanics, Hamilton's principle of least action dictates that a particle, subjected to an external potential $V(r)$, follows a trajectory for which the integral

$$S_{\Gamma} = \int_{t_a}^{t_b} L[\vec{r}(t), \dot{\vec{r}}(t)] dt \quad (6.2)$$

is stationary, where the Lagrangian is defined as is stationary, where the Lagrangian is defined as $L[\vec{r}, \dot{\vec{r}}] = \frac{1}{2}m\dot{\vec{r}}^2 - V(\vec{r})$, and S_{Γ} is the action along the path Γ . The phase of the wavefunction at the final point b then depends on the initial wavefunction at a and the classical action, as follows:

$$|\Psi(\vec{r}_b, t_b)\rangle \propto e^{iS_{\Gamma}/\hbar} |\Psi(\vec{r}_a, t_a)\rangle \quad (6.3)$$

The atom is treated classically with its position and velocity corresponding to the center of mass and group velocity of a spatially localized quantum mechanical wavepacket.

Perturbative approach

The alteration in phase resulting from a modification to the Lagrangian, represented by ΔL , can be computed to the initial order by integrating the perturbing potential across the classical trajectory unaffected by the disturbance, identified as Γ_0 . The comprehensive derivation of this equation is provided in the thesis [145] and [146]. Thus, the discrepancy in phase between the two arms of the interferometer is expressed as:

$$\Delta\Phi = \frac{1}{\hbar} \oint_{\Gamma_0} \Delta L dt \quad (6.4)$$

To determine the appropriate perturbation to the Lagrangian for a rotating interferometer, one can consider an inertial coordinate frame and a frame rotating with angular frequency Ω with a common origin. The Lagrangian in a rotating frame can be defined as :

$$L'(\vec{r}, v) = \frac{1}{2} m (\vec{v} + \vec{\Omega} \times \vec{r})^2 \quad (6.5)$$

$$= \frac{1}{2} m v^2 + m \vec{\Omega} \cdot (\vec{\Omega} \times \vec{r}) + O(\Omega^2) \quad (6.6)$$

In the rotating frame, Coriolis acceleration adds a perturbation $\Delta L' = \Delta L = m \vec{\Omega} \cdot (\vec{r} \times \vec{v})$ to the free particle Lagrangian. Now one can use Equation 6.4 to compute the phase shift due to this perturbation:

$$\Delta\Phi_\Omega = \frac{m}{\hbar} \oint_{\Gamma_0} \vec{\Omega} \cdot (\vec{r} \times \vec{v}) dt = \frac{1}{\hbar c^2} \oint (\vec{\Omega} \times \vec{r}) \cdot \vec{E} d\vec{r} = \frac{2E}{\hbar c^2} \vec{A} \cdot \vec{\Omega} \quad (6.7)$$

6.2 Rotation sensor using atom interferometry

Within this context, Equation 6.7 underscores the superiority of employing an atom interferometer compared to a light interferometer. Specifically, when considering an equal interferometric area, and comparing the total energy of a photon in an optical interferometer ($E_{\text{photon}} = h\nu$) to the total energy of an atom in an atom interferometer

($E_{\text{atom}} = mc^2$), the resultant ratio is as follows:

$$\frac{E_{\text{atom}}}{E_{\text{photon}}} \approx 10^{11} \quad (6.8)$$

The equation presented above suggests a substantial enhancement in sensitivity achievable through the utilization of AI. The relationship between the differential phase shift and inertial and gravitational forces depends on the specific interferometer pulse sequence being used. The timing and particular combination of pulses used determine the atomic trajectories, and also control how the laser phase is sampled by the interfering paths. We will briefly discuss about the two methods, the three pulse and four pulse method and their effects on linear accelerations and rotations from the differential phase shift. Here we work with the Bragg transition of atoms.

6.2.1 Three pulse (MZI) rotation sensor :

While the full path integral provides a way of calculating the exact phase shift for the atomic wavefunction, it is often convenient and more intuitive to break up the total phase contribution into several different components. In particular, treating the discrete atom-laser interactions independently from the free propagation of the atom simplifies the calculation. Also, phase shifts due to spatial offsets in the initial/final positions of the interfering paths can be treated independently, so that:

$$\Delta\Phi_{\text{total}} = \Delta\Phi_{\text{prop}} + \Delta\Phi_{\text{sep}} + \Delta\Phi_{\text{laser}} \quad (6.9)$$

The propagation phase $\Delta\Phi_{\text{prop}}$ represents the phase shift picked up by the atom due to its free propagation between the pulses. Fig.6.1 a) shows the MZI where the phase shift caused by the rotation due to doppler shift is

$$\Phi_{\text{laser}} = \phi_1 - 2\phi_2 + \phi_3 \quad (6.10)$$

where ϕ_i is the phase experienced by atoms during i th pulse. Thus $\phi_i = \phi_i^0 + \vec{k}_{\text{eff}} \cdot \vec{x}_i$, where ϕ_i^0 is the arbitrary laser phase and k_{eff} is the wave vector. Considering the rotation Ω which induces a slight deflection θ due to which the Doppler shift it induces

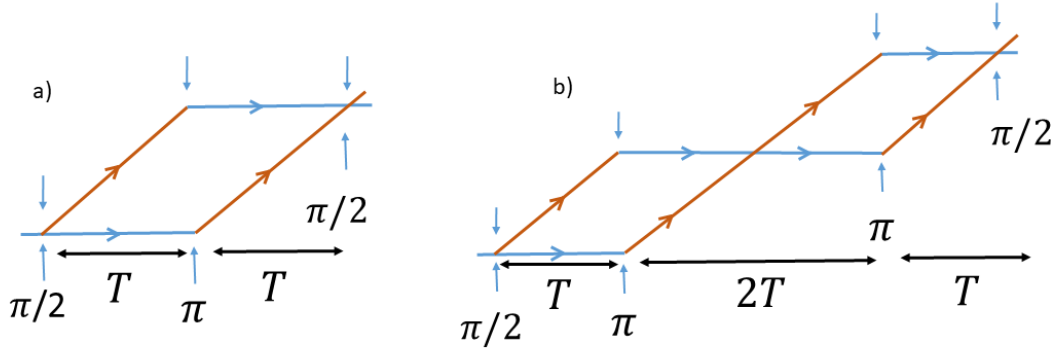


Figure 6.1: Schematic pulse diagram of BEC based Atom Interferometer and its space time trajectories. a) Three Pulse Scheme b) Four Pulse Scheme

and modifies the Equation 6.10 into

$$\Phi_{rot} = -2k_{eff} \cdot (\Omega \times v_0) T^2 \quad (6.11)$$

Here, interferometric area $A = (\hbar k_{eff})/m \cdot v_0 T^2$ which is similar to the Sagnac Phase effect in light. The generalised equation dealing with the principle of rotation involves

$$\Phi_{Total} = k_{eff} \cdot g T^2 - 2k_{eff} \cdot (\Omega \times v_0) T^2 - 2k_{eff} \cdot (\Omega \times g) T^3 + \phi_i^0 \quad (6.12)$$

where $k_{eff} \cdot g T^2$ is induced due to gravity, $-2k_{eff} \cdot (\Omega \times v_0) T^2 - 2k_{eff} \cdot (\Omega \times g) T^3$ is induced due to the rotation in any axis and $-2k_{eff} \cdot (\Omega \times g) T^3$ arises only if the gravity g is not parallel to the rotation axis.

Now moving to a three pulse method(MZI) to find the phase shift due to Rotation, usually dual interferometric loops are formed in two opposite directions. Thus one can simultaneously separate the acceleration and Rotation phase shift by having the common and differential modes. Thus the phase shift for rotation is $\Phi_{Total} = \Phi_{rot} = -4k_{eff} \cdot (\Omega \times v_0) T^2$ in differential mode.

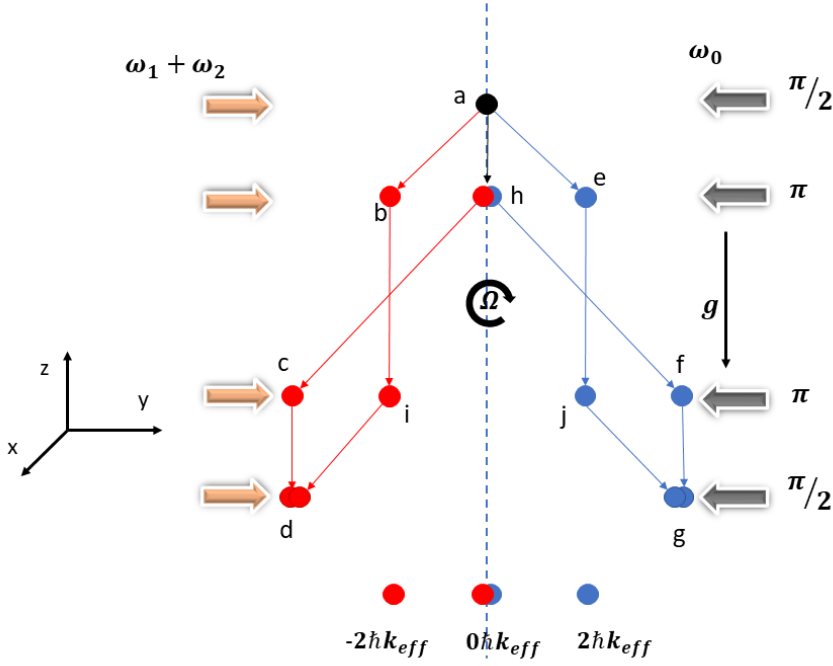


Figure 6.2: Schematic pulse diagram of simultaneous BEC-based Atom Interferometer and its space-time trajectories for Four Pulse Scheme. The orange and grey color arrows indicate the Bragg pulses for splitting, redirecting, and merging. The orange beam is coupled with two different frequencies of ω_1 and ω_2 whereas the grey beam consists of one frequency ω_0 . The atoms start from a position (a) where a $\pi/2$ pulse is applied. The atoms split into two momentum states simultaneously and symmetrically with a recoil momentum of $\pm 2\hbar k$. Subsequently, we apply $\pi - \pi - \pi/2$ pulses with a time interval of $T - 2T - T$ after the first π pulse. The red arrow and circles denote the trajectories of the negative momentum interferometer, whereas the blue arrows and circles denote the trajectories of the positive momentum interferometer. Since the interferometer time is less enough than after the last $\pi/2$ pulse, the zeroth momentum state is not separated enough, so we see them overlapping with each other. Here g is the direction of gravity.

6.2.2 Four Pulse Ramsey-Bordé Atom Interferometry rotation sensor

Fig.6.1 b) shows the Ramsey-Bordé Atom Interferometry (RBI) where the phase shift caused by the rotation due to doppler shift is

$$\Phi_{rot} = \phi_1 - 2\phi_2 + 2\phi_3 - \phi_4 \quad (6.13)$$

Here we apply four pulse $\frac{\pi}{2} - \pi - \pi - \frac{\pi}{2}$ interferometer sequence where time between first,second,third and fourth is separated as T-2T-T. The differential phase shift in RBI is :

$$\Phi_{total} = 4(k \times g) \cdot \Omega T^3 + \phi_i^0 \quad (6.14)$$

In case of four pulse interferometry the constant acceleration term cancels out since $k_{eff} \cdot (\Omega \times v_0)$ reverses sign. In the Eq. 6.14, rotation term is related to acceleration due to gravity rather than the initial velocity of atoms. Also, the above four pulse configuration is insensitive to any dc acceleration along the direction of Bragg pulses.

6.3 Differential atom interferometer

As mentioned in the article about multidimensional atom optics and interferometry [147] where they discussed the measurement of three components of acceleration and Rotation simultaneously. Here we implemented simultaneous diffraction of atoms in two momentum states along one axis using double Bragg diffraction (DBD). Fig. 6.2 shows the four pulse method interferometer with Bose-Einstein condensate.

Experimental method

The experimental schematic for the dual atom interferometer is described in Fig.6.2. The initial experimental setup is explained in Section 4.2.2. Here, three counter-propagating laser beams constitute the optical lattice, and these beams are obtained from the first-order diffraction of two separate Acousto-Optic Modulators (AOM), which are driven by phase-locked AFGs. This is implemented by passing one laser beam in an AOM fed with two frequencies produced by two different AFGs and the other beam through another AOM fed with a single frequency. The peak intensity of each beam is about

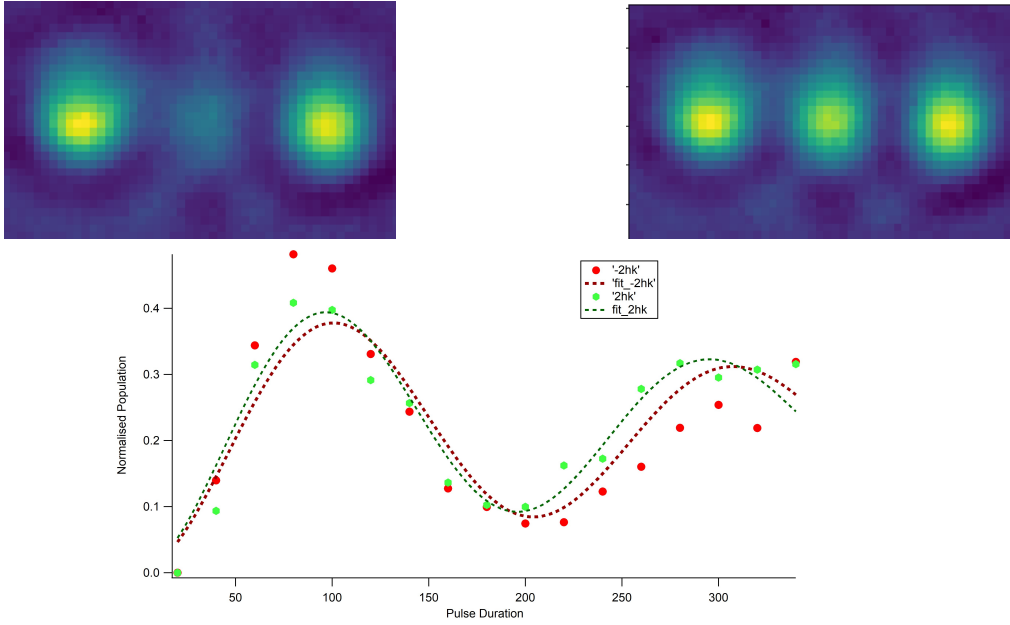


Figure 6.3: a) BEC after π pulse, b) BEC after $\pi/2$ pulse, c) Rabi oscillation for two different momentum states

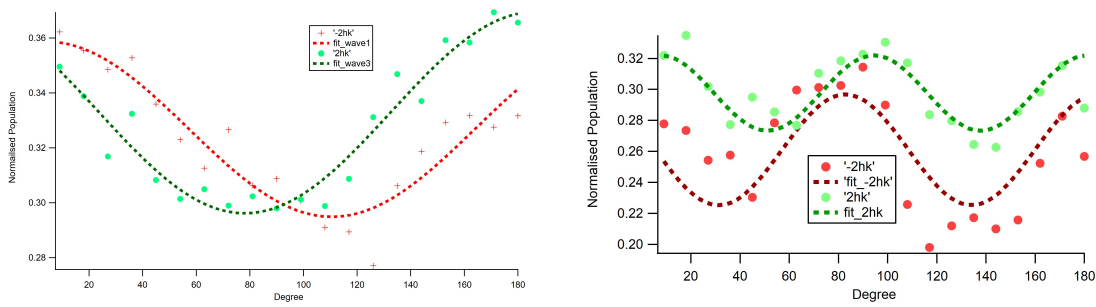


Figure 6.4: Normalised population oscillation of $\pm 2\hbar k$ for four pulse method. a) $T=450\mu s$, b) $T=1\text{ ms}$

0.3 W/cm^2 with a gaussian shape, $1/e^2$ radius of $700 \mu\text{m}$. For generating the AI pulses ($\pi - \pi/2 - \pi/2 - \pi$), we have used square pulses with an on-time of $50 \mu\text{s}$ for $\pi/2$ pulses and $100 \mu\text{s}$ for π pulse to drive the first-order Bragg transition. Fig.6.3 shows the momentum states after $\pi, \pi/2$ pulses and their corresponding Rabi oscillations.

Results

To realize the RBI, we apply four pulses of ($\pi - \pi/2 - \pi/2 - \pi$) to the BEC as discussed in Fig.6.2. We consider the case where we scan the relative phase of the last $\pi/2$ Bragg pulses from 0 to π . Fig.6.4 shows the population oscillation of the $p = \pm 2\hbar k$ as a function of phase when the interferogram time (T) is equal to $450 \mu\text{s}$ and 1 ms respectively. A clear interferometric oscillation can be seen in Fig.6.4 with a contrast of 10%.

Chapter 7

Conclusion and Outlook

7.1 Summary

The primary objective of this thesis was to establish an experimental platform for conducting precision measurements on ultracold rubidium atoms. The thesis is structured into four main parts. The initial phase focused on developing Bragg diffraction of atoms. In this stage, we successfully achieved Bragg diffraction by creating a moving optical lattice with two frequencies separated by 15 kHz. Subsequently, we demonstrated a Mach-Zehnder interferometer using the Bragg beams within the same context.

In the second stage, we demonstrated a quantum gravimeter using the existing setup. We encountered phase noise issues that limited the interferometer's performance over extended interferogram times. To address this, we conducted a comparative analysis of two techniques in atom interferometry (AI) for measuring local gravitational acceleration. By implementing a single AOM configuration instead of the conventional method, we successfully reduced phase noise in our system. This improvement led to better fringe visibility and contrast in the atom interferometer. Our system's sensitivity was measured at $99.7 \mu\text{Gal}$ with an integration time of 200 seconds and an interferometric time of 10 ms. Overall, our results demonstrate the effectiveness of using a single AOM configuration to reduce phase noise, enhance fringe visibility, and improve the performance of the atom interferometer for local gravitational acceleration measurements.

Next, we implemented double Bragg diffraction in the Bose-Einstein Condensate (BEC) to develop a rotation sensor based on an atomic Sagnac interferometer. While we

successfully demonstrated a dual interferometer, we were unable to fully characterize the system as a rotation sensor. Challenges included intensity stabilization, phase noise, interferogram time, and detuning of the Bragg beams.

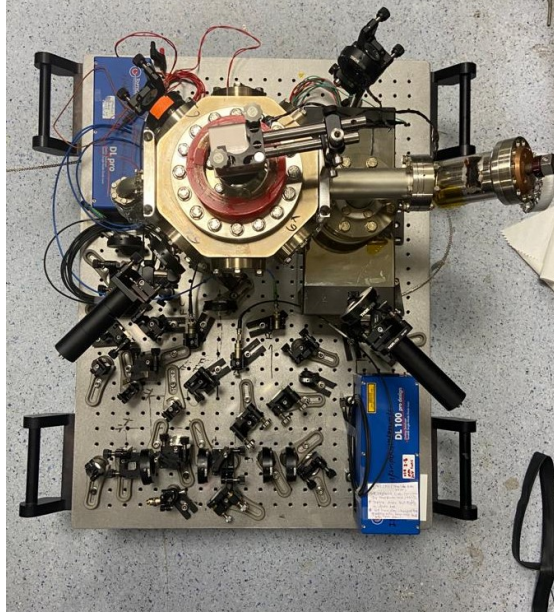


Figure 7.1: **Compact setup of a Rubidium MOT.**

7.2 Future outlook

The above study establishes a foundation for developing quantum sensors based on atom interferometry. Here are several key points where this approach can be implemented to advance quantum sensor technology.

- The development of the quantum gravimeter was conducted in a lab-based setup, which limited the free fall time of the atoms. The glass cell used in our experiments allowed only a 60 ms time of flight before the atoms struck the bottom of the cell. To enhance the sensitivity of the gravimeter, a new experimental setup is required. Figure 7.1 illustrates such a compact setup, mounted on a 3×2 feet optical table, which is also easily transportable. The next generation of atomic gravimeters will be developed using this setup.
- In our implementation, we used a TTL pulse, specifically a square pulse, for the

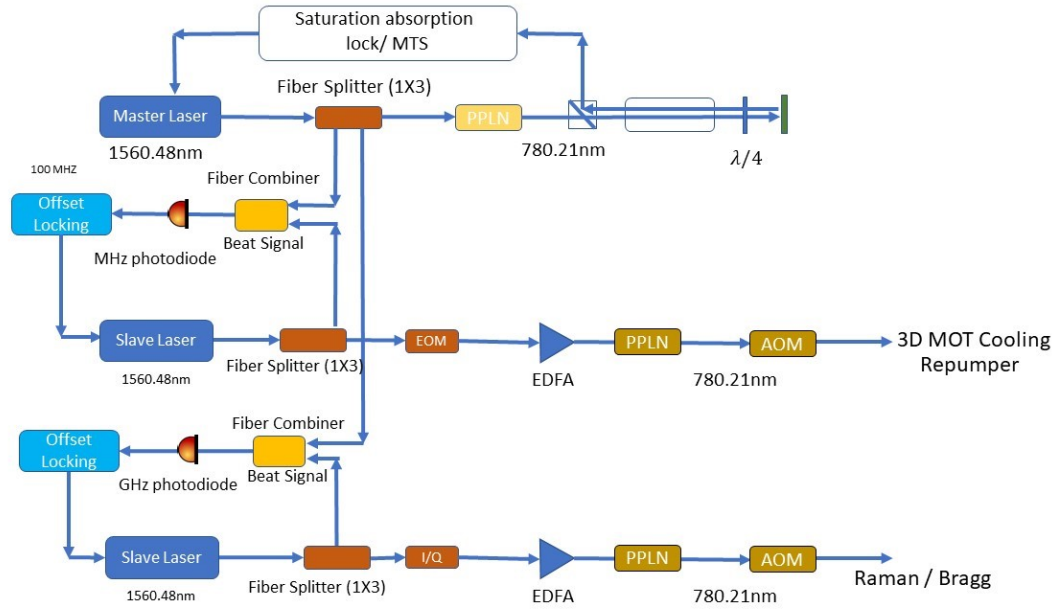


Figure 7.2: **Laser system for compact quantum gravimeter using telecom laser.**

splitting, reflecting, and merging processes. To enhance the sensitivity of the sensor, one could develop an interferometer utilizing a Gaussian pulse or an optimized pulse. This approach would allow for the use of higher diffracted orders instead of just the first order, thereby improving the sensor's sensitivity.

- One can improve the sensitivity by actively and passively isolating the entire setup from seismic noise through the introduction of an isolation platform.
- Instead of using a 780 nm laser, one can integrate a fiber telecom laser at 1560 nm, which can be frequency doubled to generate the MOT and conduct further experiments in the setup. This approach reduces the complexity of optics and incorporates fiber optics into the system. Figure 7.2 presents the block diagram detailing the components of the laser system.

Bibliography

- [1] M. Sahelgozin, “Design and construction of a transportable quantum gravimeter and realization of an atom-chip magnetic trap,” 2019.
- [2] R. Gautier, M. Guessoum, L. A. Sidorenkov, Q. Bouton, A. Landragin, and R. Geiger, “Accurate measurement of the sagnac effect for matter waves,” *Science Advances*, vol. 8, no. 23, p. eabn8009, 2022.
- [3] S. S. Szigeti, O. Hosten, and S. A. Haine, “Improving cold-atom sensors with quantum entanglement: Prospects and challenges,” *Applied Physics Letters*, vol. 118, no. 14, p. 140501, 2021.
- [4] J. Zhong, B. Tang, X. Chen, and L. Zhou, “Quantum gravimetry going toward real applications,” *The Innovation*, vol. 3, no. 3, 2022.
- [5] S. Templier, *Three-axis hybridized quantum accelerometer for inertial navigation*. PhD thesis, Université de Bordeaux, 2021.
- [6] S. KUMAR, *Towards Distributed Quantum Information Processing Using Coupling Of Neutral Atoms to Plasmonic Nanostructures*. PhD thesis, Dept. of Physics, 2017.
- [7] P. Dutta, S. S. Maurya, K. Patel, K. Biswas, J. Mangaonkar, S. Sarkar, and U. D. Rapol, “A decade of advancement of quantum sensing and metrology in india using cold atoms and ions,” *Journal of the Indian Institute of Science*, vol. 103, no. 2, pp. 609–632, 2023.

- [8] K. Bongs, M. Holynski, J. Vovrosh, P. Bouyer, G. Condon, E. Rasel, C. Schubert, W. P. Schleich, and A. Roura, “Taking atom interferometric quantum sensors from the laboratory to real-world applications,” *Nature Reviews Physics*, vol. 1, no. 12, pp. 731–739, 2019.
- [9] N. Aslam, H. Zhou, E. K. Urbach, M. J. Turner, R. L. Walsworth, M. D. Lukin, and H. Park, “Quantum sensors for biomedical applications,” *Nature Reviews Physics*, vol. 5, no. 3, pp. 157–169, 2023.
- [10] C. Janvier, V. Ménoret, B. Desruelle, S. Merlet, A. Landragin, and F. Pereira dos Santos, “Compact differential gravimeter at the quantum projection-noise limit,” *Phys. Rev. A*, vol. 105, p. 022801, Feb 2022.
- [11] B. Stray, A. Lamb, A. Kaushik, J. Vovrosh, A. Rodgers, J. Winch, F. Hayati, D. Boddice, A. Stabrawa, A. Niggebaum, *et al.*, “Quantum sensing for gravity cartography,” *Nature*, vol. 602, no. 7898, pp. 590–594, 2022.
- [12] W. D. Phillips, “Nobel lecture: Laser cooling and trapping of neutral atoms,” *Rev. Mod. Phys.*, vol. 70, pp. 721–741, Jul 1998.
- [13] M. Kasevich and S. Chu, “Atomic interferometry using stimulated raman transitions,” *Phys. Rev. Lett.*, vol. 67, pp. 181–184, Jul 1991.
- [14] K. B. Davis, M. O. Mewes, M. R. Andrews, N. J. van Druten, D. S. Durfee, D. M. Kurn, and W. Ketterle, “Bose-einstein condensation in a gas of sodium atoms,” *Phys. Rev. Lett.*, vol. 75, pp. 3969–3973, Nov 1995.
- [15] D. S. Jin, J. R. Ensher, M. R. Matthews, C. E. Wieman, and E. A. Cornell, “Collective excitations of a bose-einstein condensate in a dilute gas,” *Phys. Rev. Lett.*, vol. 77, pp. 420–423, Jul 1996.
- [16] V. Ménoret, P. Vermeulen, N. Le Moigne, S. Bonvalot, P. Bouyer, A. Landragin, and B. Desruelle, “Gravity measurements below 10^{-9} g with a transportable absolute quantum gravimeter,” *Scientific Reports*, vol. 8, p. 12300, Aug 2018.

- [17] T. Bothwell, C. J. Kennedy, A. Aepli, D. Kedar, J. M. Robinson, E. Oelker, A. Staron, and J. Ye, “Resolving the gravitational redshift across a millimetre-scale atomic sample,” *Nature*, vol. 602, pp. 420–424, Feb 2022.
- [18] I. Dutta, D. Savoie, B. Fang, B. Venon, C. L. Garrido Alzar, R. Geiger, and A. Landragin, “Continuous cold-atom inertial sensor with 1 nrad/sec rotation stability,” *Phys. Rev. Lett.*, vol. 116, p. 183003, May 2016.
- [19] K. S. Hardman, P. J. Everitt, G. D. McDonald, P. Manju, P. B. Wigley, M. A. Sooriyabandara, C. C. N. Kuhn, J. E. Debs, J. D. Close, and N. P. Robins, “Simultaneous precision gravimetry and magnetic gradiometry with a bose-einstein condensate: A high precision, quantum sensor,” *Phys. Rev. Lett.*, vol. 117, p. 138501, Sep 2016.
- [20] S. H. You, M. H. Cai, S. S. Zhang, Z. S. Xu, and H. P. Liu, “Microwave-field sensing via electromagnetically induced absorption of rb irradiated by three-color infrared lasers,” *Opt. Express*, vol. 30, pp. 16619–16629, May 2022.
- [21] Y. Torii, Y. Suzuki, M. Kozuma, T. Sugiura, T. Kuga, L. Deng, and E. W. Hagley, “Mach-zehnder bragg interferometer for a bose-einstein condensate,” *Phys. Rev. A*, vol. 61, p. 041602, Feb 2000.
- [22] J. Wang, “Precision measurement with atom interferometry,” *Chinese Physics B*, vol. 24, no. 5, p. 053702, 2015.
- [23] S. Yanagimachi, K. Mizobuchi, and A. Morinaga, “Ramsey-bordé atom interferometer having two arms with different zeeman sublevels,” *Phys. Rev. A*, vol. 64, p. 041601, Sep 2001.
- [24] A. Béguin, T. Rodzinka, L. Calmels, B. Allard, and A. Gauguier, “Atom interferometry with coherent enhancement of bragg pulse sequences,” *Phys. Rev. Lett.*, vol. 131, p. 143401, Oct 2023.
- [25] K. E. McAlpine, D. Gochner, and S. Gupta, “Excited-band bloch oscillations for precision atom interferometry,” *Phys. Rev. A*, vol. 101, p. 023614, Feb 2020.

- [26] R. H. Parker, C. Yu, W. Zhong, B. Estey, and H. Müller, “Measurement of the fine-structure constant as a test of the standard model,” *Science*, vol. 360, no. 6385, pp. 191–195, 2018.
- [27] A. Wicht, J. M. Hensley, E. Sarajlic, and S. Chu, “A preliminary measurement of the fine structure constant based on atom interferometry,” *Physica Scripta*, vol. 2002, p. 82, jan 2002.
- [28] D. S. Weiss, B. C. Young, and S. Chu, “Precision measurement of the photon recoil of an atom using atomic interferometry,” *Phys. Rev. Lett.*, vol. 70, pp. 2706–2709, May 1993.
- [29] G. T. Foster, J. B. Fixler, J. M. McGuirk, and M. A. Kasevich, “Method of phase extraction between coupled atom interferometers using ellipse-specific fitting,” *Opt. Lett.*, vol. 27, pp. 951–953, Jun 2002.
- [30] E. Tiesinga, P. J. Mohr, D. B. Newell, and B. N. Taylor, “Codata recommended values of the fundamental physical constants: 2018,” *Rev. Mod. Phys.*, vol. 93, p. 025010, Jun 2021.
- [31] L. I. Schiff, “On experimental tests of the general theory of relativity,” *Am. J. Phys*, vol. 28, no. 4, pp. 340–343, 1960.
- [32] C. M. Will, “The confrontation between general relativity and experiment,” *Living reviews in relativity*, vol. 17, no. 1, pp. 1–117, 2014.
- [33] G. Tino, L. Cacciapuoti, S. Capozziello, G. Lambiase, and F. Sorrentino, “Precision gravity tests and the einstein equivalence principle,” *Progress in Particle and Nuclear Physics*, vol. 112, p. 103772, 2020.
- [34] E. G. Adelberger, J. Gundlach, B. Heckel, S. Hoedl, and S. Schlamminger, “Torsion balance experiments: A low-energy frontier of particle physics,” *Progress in Particle and Nuclear Physics*, vol. 62, no. 1, pp. 102–134, 2009.
- [35] P. Touboul, G. Métris, M. Rodrigues, Y. André, Q. Baghi, J. Berge, D. Boulanger, S. Bremer, R. Chhun, B. Christophe, *et al.*, “Space test of the equivalence prin-

- ciple: first results of the microscope mission,” *Classical and Quantum Gravity*, vol. 36, no. 22, p. 225006, 2019.
- [36] S. Fray, C. A. Diez, T. W. Hänsch, and M. Weitz, “Atomic interferometer with amplitude gratings of light and its applications to atom based tests of the equivalence principle,” *Phys. Rev. Lett.*, vol. 93, p. 240404, Dec 2004.
- [37] P. Asenbaum, C. Overstreet, M. Kim, J. Curti, and M. A. Kasevich, “Atom-interferometric test of the equivalence principle at the 10^{-12} level,” *Phys. Rev. Lett.*, vol. 125, p. 191101, Nov 2020.
- [38] M. G. Tarallo, T. Mazzoni, N. Poli, D. V. Sutyryn, X. Zhang, and G. M. Tino, “Test of einstein equivalence principle for 0-spin and half-integer-spin atoms: Search for spin-gravity coupling effects,” *Phys. Rev. Lett.*, vol. 113, p. 023005, Jul 2014.
- [39] H. Albers, A. Herbst, L. L. Richardson, H. Heine, D. Nath, J. Hartwig, C. Schubert, C. Vogt, M. Woltmann, C. Lämmerzahl, *et al.*, “Quantum test of the universality of free fall using rubidium and potassium,” *The European Physical Journal D*, vol. 74, pp. 1–9, 2020.
- [40] S. Dimopoulos, P. W. Graham, J. M. Hogan, M. A. Kasevich, and S. Rajendran, “Atomic gravitational wave interferometric sensor,” *Phys. Rev. D*, vol. 78, p. 122002, Dec 2008.
- [41] J. M. Hogan and M. A. Kasevich, “Atom-interferometric gravitational-wave detection using heterodyne laser links,” *Phys. Rev. A*, vol. 94, p. 033632, Sep 2016.
- [42] P. Amaro-Seoane, S. Aoudia, S. Babak, P. Binétruy, E. Berti, A. Bohé, C. Caprini, M. Colpi, N. J. Cornish, K. Danzmann, J.-F. Dufaux, J. Gair, O. Jennrich, P. Jetzer, A. Klein, R. N. Lang, A. Lobo, T. Littenberg, S. T. McWilliams, G. Nelemans, A. Petiteau, E. K. Porter, B. F. Schutz, A. Sesana, R. Stebbins, T. Sumner, M. Vallisneri, S. Vitale, M. Volonteri, and H. Ward, “Low-frequency gravitational-wave science with elisa/ngo,” *Classical and Quantum Gravity*, vol. 29, p. 124016, jun 2012.

- [43] B. P. Abbott, R. Abbott, and e. a. Abbott, “Observation of gravitational waves from a binary black hole merger,” *Phys. Rev. Lett.*, vol. 116, p. 061102, Feb 2016.
- [44] B. Canuel, A. Bertoldi, L. Amand, E. Pozzo di Borgo, T. Chantrait, C. Danquigny, M. Dovale Álvarez, B. Fang, A. Freise, R. Geiger, J. Gillot, S. Henry, J. Hinderer, D. Holleville, J. Junca, G. Lefèvre, M. Merzougui, N. Mielec, T. Monfret, S. Pelisson, M. Prevedelli, S. Reynaud, I. Riou, Y. Rogister, S. Rosat, E. Cormier, A. Landragin, W. Chaibi, S. Gaffet, and P. Bouyer, “Exploring gravity with the miga large scale atom interferometer,” *Scientific Reports*, vol. 8, p. 14064, Sep 2018.
- [45] W. Chaibi, R. Geiger, B. Canuel, A. Bertoldi, A. Landragin, and P. Bouyer, “Low frequency gravitational wave detection with ground-based atom interferometer arrays,” *Phys. Rev. D*, vol. 93, p. 021101, Jan 2016.
- [46] M. Kasevich and S. Chu, “Measurement of the gravitational acceleration of an atom with a light-pulse atom interferometer,” *Applied Physics B*, vol. 54, pp. 321–332, 1992.
- [47] D. M. Giltner, R. W. McGowan, and S. A. Lee, “Theoretical and experimental study of the bragg scattering of atoms from a standing light wave,” *Phys. Rev. A*, vol. 52, pp. 3966–3972, Nov 1995.
- [48] H. Müller, S.-w. Chiow, Q. Long, S. Herrmann, and S. Chu, “Atom interferometry with up to 24-photon-momentum-transfer beam splitters,” *Phys. Rev. Lett.*, vol. 100, p. 180405, May 2008.
- [49] L. Hu, N. Poli, L. Salvi, and G. M. Tino, “Atom interferometry with the sr optical clock transition,” *Phys. Rev. Lett.*, vol. 119, p. 263601, Dec 2017.
- [50] A. Peters, K. Y. Chung, and S. Chu, “Measurement of gravitational acceleration by dropping atoms,” *Nature*, vol. 400, pp. 849–852, Aug 1999.

- [51] M. Ben Dahan, E. Peik, J. Reichel, Y. Castin, and C. Salomon, “Bloch oscillations of atoms in an optical potential,” *Phys. Rev. Lett.*, vol. 76, pp. 4508–4511, Jun 1996.
- [52] G. Ferrari, N. Poli, F. Sorrentino, and G. M. Tino, “Long-lived bloch oscillations with bosonic sr atoms and application to gravity measurement at the micrometer scale,” *Phys. Rev. Lett.*, vol. 97, p. 060402, Aug 2006.
- [53] P. A. Altin, M. T. Johnsson, V. Negnevitsky, G. R. Dennis, R. P. Anderson, J. E. Debs, S. S. Szigeti, K. S. Hardman, S. Bennetts, G. D. McDonald, L. D. Turner, J. D. Close, and N. P. Robins, “Precision atomic gravimeter based on bragg diffraction,” *New Journal of Physics*, vol. 15, p. 023009, feb 2013.
- [54] G. Sagnac, “L’éther lumineux démontré par l’effet du vent relatif d’éther dans un interféromètre en rotation uniforme,” *CR Acad. Sci.*, vol. 157, pp. 708–710, 1913.
- [55] A. Lenef, T. D. Hammond, E. T. Smith, M. S. Chapman, R. A. Rubenstein, and D. E. Pritchard, “Rotation sensing with an atom interferometer,” *Phys. Rev. Lett.*, vol. 78, pp. 760–763, Feb 1997.
- [56] P. Dutta, S. S. Maurya, K. Patel, K. Biswas, J. Mangaonkar, S. Sarkar, and U. D. Rapol, “A decade of advancement of quantum sensing and metrology in india using cold atoms and ions,” *Journal of the Indian Institute of Science*, vol. 103, pp. 609–632, Apr 2023.
- [57] J. Esteve, C. Gross, A. Weller, S. Giovanazzi, and M. Oberthaler, “Squeezing and entanglement in a bose–einstein condensate,” *Nature*, vol. 455, no. 7217, pp. 1216–1219, 2008.
- [58] M. F. Riedel, P. Böhi, Y. Li, T. W. Hänsch, A. Sinatra, and P. Treutlein, “Atom-chip-based generation of entanglement for quantum metrology,” *Nature*, vol. 464, no. 7292, pp. 1170–1173, 2010.

- [59] C. Gross, T. Zibold, E. Nicklas, J. Esteve, and M. K. Oberthaler, “Nonlinear atom interferometer surpasses classical precision limit,” *Nature*, vol. 464, no. 7292, pp. 1165–1169, 2010.
- [60] S. S. Szigeti, S. P. Nolan, J. D. Close, and S. A. Haine, “High-precision quantum-enhanced gravimetry with a bose-einstein condensate,” *Phys. Rev. Lett.*, vol. 125, p. 100402, Sep 2020.
- [61] F. Anders, A. Idel, P. Feldmann, D. Bondarenko, S. Loriani, K. Lange, J. Peise, M. Gersemann, B. Meyer-Hoppe, S. Abend, N. Gaaloul, C. Schubert, D. Schlippert, L. Santos, E. Rasel, and C. Klempt, “Momentum entanglement for atom interferometry,” *Phys. Rev. Lett.*, vol. 127, p. 140402, Sep 2021.
- [62] T. Lévêque, A. Gauguier, F. Michaud, F. Pereira Dos Santos, and A. Landragin, “Enhancing the area of a raman atom interferometer using a versatile double-diffraction technique,” *Phys. Rev. Lett.*, vol. 103, p. 080405, Aug 2009.
- [63] N. Malossi, Q. Bodart, S. Merlet, T. Lévêque, A. Landragin, and F. P. D. Santos, “Double diffraction in an atomic gravimeter,” *Phys. Rev. A*, vol. 81, p. 013617, Jan 2010.
- [64] S.-w. Chiow, T. Kovachy, H.-C. Chien, and M. A. Kasevich, “ $102\hbar k$ large area atom interferometers,” *Phys. Rev. Lett.*, vol. 107, p. 130403, Sep 2011.
- [65] P. Cladé, S. Guellati-Khélifa, F. m. c. Nez, and F. m. c. Biraben, “Large momentum beam splitter using bloch oscillations,” *Phys. Rev. Lett.*, vol. 102, p. 240402, Jun 2009.
- [66] H. Ahlers, H. Müntinga, A. Wenzlawski, M. Krutzik, G. Tackmann, S. Abend, N. Gaaloul, E. Giese, A. Roura, R. Kuhl, C. Lämmerzahl, A. Peters, P. Windpassinger, K. Sengstock, W. P. Schleich, W. Ertmer, and E. M. Rasel, “Double bragg interferometry,” *Phys. Rev. Lett.*, vol. 116, p. 173601, Apr 2016.
- [67] A. Noureldin, T. B. Karamat, and J. Georgy, *Fundamentals of inertial navigation, satellite-based positioning and their integration*. Springer Science & Business Media, 2012.

- [68] C. Musso, B. Sacleux, A. Bresson, J. Allard, K. Dahia, Y. Bidel, N. Zahzam, and C. Palmier, “Terrain-aided navigation with an atomic gravimeter,” in *2019 22th International Conference on Information Fusion (FUSION)*, pp. 1–8, 2019.
- [69] A. M. Phillips, M. J. Wright, I. Riou, S. Maddox, S. Maskell, and J. F. Ralph, “Position fixing with cold atom gravity gradiometers,” *AVS Quantum Science*, vol. 4, no. 2, 2022.
- [70] X. Wang, C. Gilliam, A. Kealy, J. Close, and B. Moran, “Probabilistic map matching for robust inertial navigation aiding,” *NAVIGATION: Journal of the Institute of Navigation*, vol. 70, no. 2, 2023.
- [71] R. Wu, Q. Wu, F. Han, T. Liu, P. Hu, and H. Li, “Gravity compensation using egm2008 for high-precision long-term inertial navigation systems,” *Sensors*, vol. 16, no. 12, 2016.
- [72] J. Shockley and J. Raquet, “Navigation of ground vehicles using magnetic field variations,” *NAVIGATION: Journal of the Institute of Navigation*, vol. 61, no. 4, pp. 237–252, 2014.
- [73] <https://aosense.com/product/gravimeter/>.
- [74] <http://www.atomionics.com/gravio.html>.
- [75] http://https://www.m2lasers.com/quantum-datasheet.html?file=M_Squared_Quantum%20Grav
- [76] S. Templier, P. Cheiney, Q. d’Armagnac de Castanet, B. Gouraud, H. Porte, F. Napolitano, P. Bouyer, B. Battelier, and B. Barrett, “Tracking the vector acceleration with a hybrid quantum accelerometer triad,” *Science Advances*, vol. 8, no. 45, p. eadd3854, 2022.
- [77] M. Schmidt, A. Senger, M. Hauth, C. Freier, V. Schkolnik, and A. Peters, “A mobile high-precision absolute gravimeter based on atom interferometry,” *Gyroscopy and Navigation*, vol. 2, no. 3, pp. 170–177, 2011.
- [78] A. Ashkin, “Acceleration and trapping of particles by radiation pressure,” *Phys. Rev. Lett.*, vol. 24, pp. 156–159, Jan 1970.

- [79] T. Hänsch and A. Schawlow, "Cooling of gases by laser radiation," *Optics Communications*, vol. 13, no. 1, pp. 68–69, 1975.
- [80] D. Wineland and H. Dehmelt, "Principles of the stored ion calorimeter," *Journal of Applied Physics*, vol. 46, no. 2, pp. 919–930, 1975.
- [81] A. Ashkin, "Trapping of atoms by resonance radiation pressure," *Phys. Rev. Lett.*, vol. 40, pp. 729–732, Mar 1978.
- [82] W. D. Phillips and H. Metcalf, "Laser deceleration of an atomic beam," *Phys. Rev. Lett.*, vol. 48, pp. 596–599, Mar 1982.
- [83] S. Chu, L. Hollberg, J. E. Bjorkholm, A. Cable, and A. Ashkin, "Three-dimensional viscous confinement and cooling of atoms by resonance radiation pressure," *Phys. Rev. Lett.*, vol. 55, pp. 48–51, Jul 1985.
- [84] S. Chu, J. E. Bjorkholm, A. Ashkin, and A. Cable, "Experimental observation of optically trapped atoms," *Phys. Rev. Lett.*, vol. 57, pp. 314–317, Jul 1986.
- [85] P. D. Lett, R. N. Watts, C. I. Westbrook, W. D. Phillips, P. L. Gould, and H. J. Metcalf, "Observation of atoms laser cooled below the doppler limit," *Phys. Rev. Lett.*, vol. 61, pp. 169–172, Jul 1988.
- [86] J. Dalibard and C. Cohen-Tannoudji, "Laser cooling below the doppler limit by polarization gradients: simple theoretical models," *J. Opt. Soc. Am. B*, vol. 6, pp. 2023–2045, Nov 1989.
- [87] P. J. Ungar, D. S. Weiss, E. Riis, and S. Chu, "Optical molasses and multilevel atoms: theory," *JOSA B*, vol. 6, no. 11, pp. 2058–2071, 1989.
- [88] D. S. Weiss, E. Riis, Y. Shevy, P. J. Ungar, and S. Chu, "Optical molasses and multilevel atoms: experiment," *JOSA B*, vol. 6, no. 11, pp. 2072–2083, 1989.
- [89] A. Aspect, E. Arimondo, R. Kaiser, N. Vansteenkiste, and C. Cohen-Tannoudji, "Laser cooling below the one-photon recoil energy by velocity-selective coherent population trapping," *Phys. Rev. Lett.*, vol. 61, pp. 826–829, Aug 1988.

- [90] M. Kasevich and S. Chu, “Laser cooling below a photon recoil with three-level atoms,” *Phys. Rev. Lett.*, vol. 69, pp. 1741–1744, Sep 1992.
- [91] J. Lawall, S. Kulin, B. Saubamea, N. Bigelow, M. Leduc, and C. Cohen-Tannoudji, “Three-dimensional laser cooling of helium beyond the single-photon recoil limit,” *Phys. Rev. Lett.*, vol. 75, pp. 4194–4197, Dec 1995.
- [92] H. J. Lee, C. S. Adams, M. Kasevich, and S. Chu, “Raman cooling of atoms in an optical dipole trap,” *Phys. Rev. Lett.*, vol. 76, pp. 2658–2661, Apr 1996.
- [93] Bose, “Plancks gesetz und lichtquantenhypothese,” *Zeitschrift für Physik*, vol. 26, no. 1, pp. 178–181, 1924.
- [94] A. Einstein, “Quantentheorie des einatomigen idealen gases. sitzungsberichte der preussischen akademie der wissenschaften, physikalisch-mathematische klasse. akademie der wissenschaften,” *The Collected Papers of Albert Einstein*, vol. 14, 1924.
- [95] F. Kubli, “Louis de broglie und die entdeckung der materiewellen,” *Archive for History of Exact Sciences*, pp. 26–68, 1970.
- [96] H. J. Metcalf and P. Van der Straten, *Laser cooling and trapping*. Springer Science & Business Media, 1999.
- [97] K. W. Martin, G. Phelps, N. D. Lemke, M. S. Bigelow, B. Stuhl, M. Wojcik, M. Holt, I. Coddington, M. W. Bishop, and J. H. Burke, “Compact optical atomic clock based on a two-photon transition in rubidium,” *Phys. Rev. Appl.*, vol. 9, p. 014019, Jan 2018.
- [98] S. Hartmann, J. Jenewein, E. Giese, S. Abend, A. Roura, E. M. Rasel, and W. P. Schleich, “Regimes of atomic diffraction: Raman versus bragg diffraction in retroreflective geometries,” *Phys. Rev. A*, vol. 101, p. 053610, May 2020.
- [99] P. Meystre, *Atom optics*, vol. 33. Springer Science & Business Media, 2001.
- [100] P. R. Berman, *Atom interferometry*. Academic press, 1997.

- [101] K. Moler, D. S. Weiss, M. Kasevich, and S. Chu, “Theoretical analysis of velocity-selective raman transitions,” *Phys. Rev. A*, vol. 45, pp. 342–348, Jan 1992.
- [102] S. SARKAR, *Ultracold atoms in 1-D optical lattices: experiments towards quantum chaos and atom interferometry*. PhD thesis, Dept. of Physics, 2019.
- [103] R. Grimm, M. Weidemüller, and Y. B. Ovchinnikov, “Optical dipole traps for neutral atoms,” in *Advances in atomic, molecular, and optical physics*, vol. 42, pp. 95–170, Elsevier, 2000.
- [104] P. B. Blakie and R. J. Ballagh, “Mean-field treatment of bragg scattering from a bose-einstein condensate,” *Journal of Physics B: Atomic, Molecular and Optical Physics*, vol. 33, no. 19, p. 3961, 2000.
- [105] P. Dutta, S. S. Maurya, K. Biswas, K. Patel, and U. D. Rapol, “Comparative analysis of phase noise for different configurations of Bragg lattice for an atomic gravimeter with Bose–Einstein condensate,” *AIP Advances*, vol. 14, p. 015352, 01 2024.
- [106] M. O. Scully and J. P. Dowling, “Quantum-noise limits to matter-wave interferometry,” *Phys. Rev. A*, vol. 48, pp. 3186–3190, Oct 1993.
- [107] O. Carnal and J. Mlynek, “Young’s double-slit experiment with atoms: A simple atom interferometer,” *Phys. Rev. Lett.*, vol. 66, pp. 2689–2692, May 1991.
- [108] T. L. Gustavson, P. Bouyer, and M. A. Kasevich, “Precision rotation measurements with an atom interferometer gyroscope,” *Phys. Rev. Lett.*, vol. 78, pp. 2046–2049, Mar 1997.
- [109] D. W. Keith, C. R. Ekstrom, Q. A. Turchette, and D. E. Pritchard, “An interferometer for atoms,” *Phys. Rev. Lett.*, vol. 66, pp. 2693–2696, May 1991.
- [110] Z.-K. Hu, B.-L. Sun, X.-C. Duan, M.-K. Zhou, L.-L. Chen, S. Zhan, Q.-Z. Zhang, and J. Luo, “Demonstration of an ultrahigh-sensitivity atom-interferometry absolute gravimeter,” *Phys. Rev. A*, vol. 88, p. 043610, Oct 2013.

- [111] A. Peters, K. Y. Chung, and S. Chu, “Measurement of gravitational acceleration by dropping atoms,” *Nature*, vol. 400, no. 6747, pp. 849–852, 1999.
- [112] J. Le Gouët, T. Mehlstäubler, J. Kim, S. Merlet, A. Clairon, A. Landragin, and F. P. Dos Santos, “Limits to the sensitivity of a low noise compact atomic gravimeter,” *Applied Physics B*, vol. 92, no. 2, pp. 133–144, 2008.
- [113] M.-K. Zhou, Z.-K. Hu, X.-C. Duan, B.-L. Sun, J.-B. Zhao, and J. Luo, “Precisely mapping the magnetic field gradient in vacuum with an atom interferometer,” *Phys. Rev. A*, vol. 82, p. 061602, Dec 2010.
- [114] A. Smith, B. E. Anderson, S. Chaudhury, and P. S. Jessen, “Three-axis measurement and cancellation of background magnetic fields to less than $50 \mu\text{g}$ in a cold atom experiment,” *Journal of Physics B: Atomic, Molecular and Optical Physics*, vol. 44, no. 20, p. 205002, 2011.
- [115] P. Berg, S. Abend, G. Tackmann, C. Schubert, E. Giese, W. P. Schleich, F. A. Narducci, W. Ertmer, and E. M. Rasel, “Composite-light-pulse technique for high-precision atom interferometry,” *Phys. Rev. Lett.*, vol. 114, p. 063002, Feb 2015.
- [116] B. Battelier, B. Barrett, L. Fouché, L. Chichet, L. Antoni-Micollier, H. Porte, F. Napolitano, J. Lautier, A. Landragin, and P. Bouyer, “Development of compact cold-atom sensors for inertial navigation,” in *Quantum Optics* (J. Stuhler and A. J. Shields, eds.), vol. 9900, pp. 21 – 37, International Society for Optics and Photonics, SPIE, 2016.
- [117] R. Geiger, V. Ménoret, G. Stern, N. Zahzam, P. Cheinet, B. Battelier, A. Villing, F. Moron, M. Lours, Y. Bidel, *et al.*, “Detecting inertial effects with airborne matter-wave interferometry,” *Nature communications*, vol. 2, no. 1, pp. 1–7, 2011.
- [118] R. Bouchendira, P. Cladé, S. Guellati-Khélifa, F. m. c. Nez, and F. m. c. Biraben, “New determination of the fine structure constant and test of the quantum electrodynamics,” *Phys. Rev. Lett.*, vol. 106, p. 080801, Feb 2011.

- [119] G. Rosi, F. Sorrentino, L. Cacciapuoti, M. Prevedelli, and G. Tino, “Precision measurement of the newtonian gravitational constant using cold atoms,” *Nature*, vol. 510, no. 7506, pp. 518–521, 2014.
- [120] S. Dimopoulos, P. W. Graham, J. M. Hogan, and M. A. Kasevich, “Testing general relativity with atom interferometry,” *Phys. Rev. Lett.*, vol. 98, p. 111102, Mar 2007.
- [121] G. Rosi, G. D’Amico, L. Cacciapuoti, F. Sorrentino, M. Prevedelli, M. Zych, Č. Brukner, and G. Tino, “Quantum test of the equivalence principle for atoms in coherent superposition of internal energy states,” *Nature communications*, vol. 8, no. 1, pp. 1–6, 2017.
- [122] K. Bongs, M. Holynski, J. Vovrosh, P. Bouyer, G. Condon, E. Rasel, C. Schubert, W. P. Schleich, and A. Roura, “Taking atom interferometric quantum sensors from the laboratory to real-world applications,” *Nature Reviews Physics*, vol. 1, no. 12, pp. 731–739, 2019.
- [123] I. Alonso, C. Alpigiani, B. Altschul, H. Araújo, G. Arduini, J. Arlt, L. Badurina, A. Balaž, S. Bandrupally, B. C. Barish, *et al.*, “Cold atoms in space: community workshop summary and proposed road-map,” *EPJ Quantum Technology*, vol. 9, no. 1, pp. 1–55, 2022.
- [124] S. S. Szigeti, J. E. Debs, J. J. Hope, N. P. Robins, and J. D. Close, “Why momentum width matters for atom interferometry with bragg pulses,” *New Journal of Physics*, vol. 14, no. 2, p. 023009, 2012.
- [125] M. Fattori, C. D’Errico, G. Roati, M. Zaccanti, M. Jona-Lasinio, M. Modugno, M. Inguscio, and G. Modugno, “Atom interferometry with a weakly interacting bose-einstein condensate,” *Phys. Rev. Lett.*, vol. 100, p. 080405, Feb 2008.
- [126] J. Stenger, S. Inouye, A. P. Chikkatur, D. M. Stamper-Kurn, D. E. Pritchard, and W. Ketterle, “Bragg spectroscopy of a bose-einstein condensate,” *Phys. Rev. Lett.*, vol. 82, pp. 4569–4573, Jun 1999.

- [127] Y. Cheng, K. Zhang, L.-L. Chen, W.-J. Xu, Q. Luo, M.-K. Zhou, and Z.-K. Hu, “Low-phase noise and high-power laser for Bragg atom interferometer,” *AIP Advances*, vol. 7, p. 095211, 09 2017.
- [128] S. Abend, M. Gebbe, M. Gersemann, H. Ahlers, H. Müntinga, E. Giese, N. Gaaloul, C. Schubert, C. Lämmerzahl, W. Ertmer, W. P. Schleich, and E. M. Rasel, “Atom-chip fountain gravimeter,” *Phys. Rev. Lett.*, vol. 117, p. 203003, Nov 2016.
- [129] J. E. Debs, P. A. Altin, T. H. Barter, D. Döring, G. R. Dennis, G. McDonald, R. P. Anderson, J. D. Close, and N. P. Robins, “Cold-atom gravimetry with a bose-einstein condensate,” *Phys. Rev. A*, vol. 84, p. 033610, Sep 2011.
- [130] S. Sarkar, R. Piccon, S. Merlet, and F. P. dos Santos, “Simple and robust architecture of a laser system for atom interferometry,” *Opt. Express*, vol. 30, pp. 3358–3366, Jan 2022.
- [131] R. Charrière, M. Cadoret, N. Zahzam, Y. Bidel, and A. Bresson, “Local gravity measurement with the combination of atom interferometry and bloch oscillations,” *Phys. Rev. A*, vol. 85, p. 013639, Jan 2012.
- [132] P. Altin, M. Johnsson, V. Negnevitsky, G. Dennis, R. P. Anderson, J. Debs, S. Szigeti, K. Hardman, S. Bennetts, G. McDonald, *et al.*, “Precision atomic gravimeter based on bragg diffraction,” *New Journal of Physics*, vol. 15, no. 2, p. 023009, 2013.
- [133] M. Kozuma, L. Deng, E. W. Hagley, J. Wen, R. Lutwak, K. Helmerson, S. L. Rolston, and W. D. Phillips, “Coherent splitting of bose-einstein condensed atoms with optically induced bragg diffraction,” *Phys. Rev. Lett.*, vol. 82, pp. 871–875, Feb 1999.
- [134] D. M. Giltner, R. W. McGowan, and S. A. Lee, “Atom interferometer based on bragg scattering from standing light waves,” *Phys. Rev. Lett.*, vol. 75, pp. 2638–2641, Oct 1995.

- [135] K. S. Hardman *et al.*, *A BEC based precision gravimeter and magnetic gradiometer: design and implementation*. PhD thesis, 2016.
- [136] F. Liu, L. Gu, S. Xie, X. He, D. Yi, M. Zhang, and Q. Tao, “Acousto-optic modulation induced noises on heterodyne-interrogated interferometric fiber-optic sensors,” *Journal of Lightwave Technology*, vol. 36, no. 16, pp. 3465–3471, 2018.
- [137] P. Cheinet, B. Canuel, F. Pereira Dos Santos, A. Gauguier, F. Yver-Leduc, and A. Landragin, “Measurement of the sensitivity function in a time-domain atomic interferometer,” *IEEE Transactions on Instrumentation and Measurement*, vol. 57, no. 6, pp. 1141–1148, 2008.
- [138] S. S. Maurya, J. B. Kannan, K. Patel, P. Dutta, K. Biswas, J. Mangaonkar, M. S. Santhanam, and U. D. Rapol, “Interplay between quantum diffusion and localization in the atom-optics kicked rotor,” *Phys. Rev. E*, vol. 106, p. 034207, Sep 2022.
- [139] S. Abend, *Atom-chip gravimeter with Bose-Einstein condensates*. PhD thesis, Hannover: Gottfried Wilhelm Leibniz Universität Hannover, 2017.
- [140] “Optical swirl effect. the circulation of luminous ether in a rotating interferograph, author=Sagnac, Georges, journal=J. Phys. Theor. Appl., volume=4, number=1, pages=177–195, year=1914,”
- [141] F. Hasselbach and M. Nicklaus, “An electron optical sagnac experiment,” *Physica B+ C*, vol. 151, no. 1-2, pp. 230–234, 1988.
- [142] F. Hasselbach and M. Nicklaus, “Sagnac experiment with electrons: Observation of the rotational phase shift of electron waves in vacuum,” *Phys. Rev. A*, vol. 48, pp. 143–151, Jul 1993.
- [143] W. W. Chow, J. Gea-Banacloche, L. M. Pedrotti, V. E. Sanders, W. Schleich, and M. O. Scully, “The ring laser gyro,” *Rev. Mod. Phys.*, vol. 57, pp. 61–104, Jan 1985.

-
- [144] P. Storey and C. Cohen-Tannoudji, “The feynman path integral approach to atomic interferometry. a tutorial,” *Journal de Physique II*, vol. 4, no. 11, pp. 1999–2027, 1994.
- [145] T. L. Gustavson, *Precision rotation sensing using atom interferometry*. PhD thesis, stanford university, 2000.
- [146] K. Takase, *Precision rotation rate measurements with a mobile atom interferometer*. PhD thesis, Stanford University, 2008.
- [147] B. Barrett, P. Cheiney, B. Battelier, F. Napolitano, and P. Bouyer, “Multidimensional atom optics and interferometry,” *Phys. Rev. Lett.*, vol. 122, p. 043604, Feb 2019.